A study on numerical analysis based on boundary element method for wave propagation properties of phononic periodic structures

Haifeng GAO

A study on numerical analysis based on boundary element method for wave propagation properties of phononic periodic structures

by

Haifeng GAO

A dissertation submitted in partial fulfillment
of the requirements for the degree of
Doctor of Engineering
(Department of Mechanical Science and Engineering)
in Nagoya University
2013

ACKNOWLEDGEMENTS

I would like to thank my advisor Prof. Toshiro Matsumoto for his support and encouragement during the four-year study in Japan and for assisting me in completing my research work about BEM. I also want to express my appreciation for his careful reading and checking of my papers.

I would also like to thank our Lecturer Toru Takahashi for his helpful advice and discussion on my study. He always makes excellent comments and suggestions when I ask him for help.

I want to thank Assistant Prof. Hiroshi Isakari for his reviewing of my manuscripts and sharing with his experience.

I am deeply grateful to Prof. Inoue, Prof. Azegami and Lecturer Takagi for their careful reading and helpful comments for the improvement of my doctoral thesis.

Special thanks go to Ms Kondo and Mr. Aoki for their excellent works that offer me a comfortable life.

Lastly, I want to thank my family whose support made all of this possible. Thanks to my wife Mei for putting me up through highs and lows, to my parents who give me the chance to enjoy my life and to my son who is the sunshine in my world.

TABLE OF CONTENTS

LIST OF FIGURES

Figure

LIST OF TABLES

Table

ABSTRACT

A study on numerical analysis based on boundary element method for wave propagation properties of phononic periodic structures

by

Haifeng GAO

Chair: Professor Toshiro Matsumoto

This dissertation presents a new methodology for the band calculations of phononic structures based on the boundary element method. To investigate the band structure given by the dispersion relation, Bloch eigenvalue problems need to be solved. Using the boundary element method, nonlinear eigenvalue problems are formulated for both homogenous and periodic structures originated from the nonlinear property of the fundamental solutions. To solve the nonlinear eigenvalue problems, a contour integral method so-called Sakurai-Sugiura method is employed to extract the eigenfrequencies in a certain selected complex domain of the circular frequency surrounded by a closed Jordan curve. When using the boundary integral equation, spurious eigenvalues are also obtained together with the true eigenvalues. To identify the spurious eigenvalues, additional boundary integral equation provided by Burton-Millerfs method are employed.

After solving the resonance problems in 2D and 3D acoustic cavities as preparation works, the band structures of acoustic and elastic phononic structures in 2D are computed by the proposed methodology. For importance of practical problems, the transmissions of waves in finite unidirectional phononic periodic structures are investigated through formulating a size-reduced system matrix by the boundary element method. The frequency-banded nature existing in finite unidirectional periodic phononic structures is discussed.

CHAPTER I

Introduction

1.1 Background

Composite materials with inclusions embedded in a host periodically, are called phononic/sonic crystals. Phononic crystals are the elastic analogues of photonic crystals [3, 4, 5] and exhibit frequency-banded nature for the propagation of acoustic/elastic waves. The distinctive feature of a phononic crystal is its capacity to create band gaps, based on Bragg scattering, usually at the wavelengths that are comparable to its lattice constant. Therefore, small size phononic crystals usually display band gaps in high frequency ranges. However, relatively low frequency band gaps also can be created based on local resonances [6]. The width of the band gap, in general, increases with the difference in the densities and sound velocities of the component materials, and the frequency of the gap can be tuned, by changing lattice parameter. Along with the growing interest in phononic crystals, novel applications have been found and investigated, such as acoustic superlenses [7], acoustic lasers [8], thermal barriers [9], acoustic diode [10], phononic senors [11] etc,. The existence of band gaps in phononic crystals has been observed experimentally [12, 13, 14, 15, 16, 17, 18, 19, 20, 21, 22] and theoretically [23, 24, 25, 26, 27, 28, 29, 30, 31]. A great illustration in the experiment [15] conducted by the researchers at the Material Science Institute of Madrid shows that the sculpture in Fig. 1.1 strongly attenuates sound waves at certain frequencies.

Since fabrication of these materials is currently quite challenging, computation has become the primary tool for investigating the band structure of phononic crystals. The calculation of band structure leads to a Bloch eigenvalue problem. Various numerical methods such as plane wave expansion method, multiple-scattering theory method, finite difference domain method, finite element method [24, 23, 32, 33,

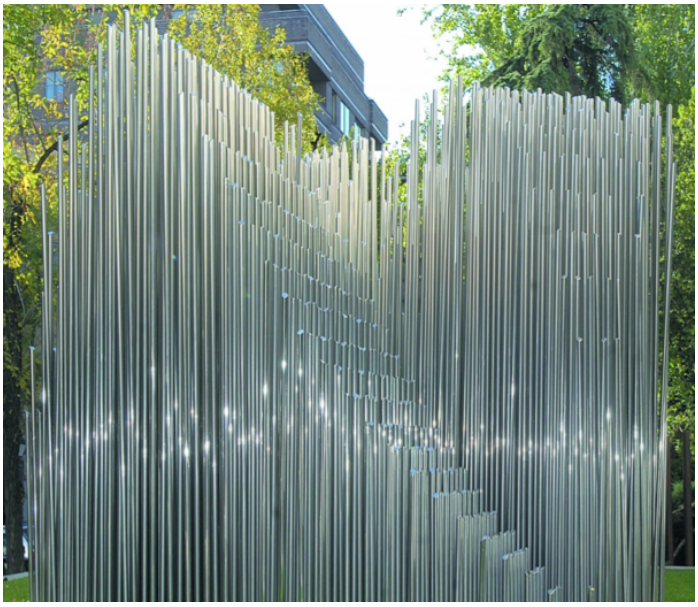

Figure 1.1: The kinematic sculpture by Eusebio Sempere consists of a periodic array of hollow stainless-steel cylinders, each 2.9 cm in diameter, arranged on a square 10×10 cm lattice [2].

34, 35, 36, 37, 38, 39] are applied to the analysis of phononic crystals including the boundary element method (BEM) [40, 41, 42]. The BEM [43], as one of the most widely used numerical methods, requires only the discretization of the surface rather than the volume. Hence, the BEM codes are easier to use with existing solid modelers and mesh generators. Furthermore, for stress concentration and crack problems, the BEM provides solutions in better accuracy, compared with the finite element method (FEM) [44]. In particular, the BEM has an advantage in dealing with infinite problems, since it has the boundary-only discretization and the fundamental solutions employed in the boundary integral equations satisfy the radiation condition automatically. However, in order to solve such infinite problems, the FEM has to adopt a perfectly matched layer [45] or special elements [46]. Though the BEM has advantages, the computing cost is considered as a drawback for large-scale problems, since the coefficient matrices formulated by the BEM are full and nonsymmetric matrices. The emergence of fast algorithms such as fast multipole method (FMM) [47, 48, 49] and adaptive across approximation (ACA) method [50, 51] can reduce the operation count from $O(N^3)$ to $O(N(\log N)^\alpha)$ where N is the degrees of the freedom. This makes the BEM become more attractive for large-scale problems. However, even the computing cost is decreased, the calculation of eigenfrequencies is very difficult because the fundamental solutions of interest are nonlinear with respect to circular

frequency or wave number. This occurs when the BEM is applied to the problems such as acoustic resonance, free vibration of elastic structures and Bloch eigenvalue calculations. In the BEM formulation, the circular frequency ω is involved in the coefficient matrix implicitly, and the eigenequation is a transcendental equation that contains the Bessel/Hankel functions.

However, the emergence of the contour integral method [52] which converts nonlinear eigenvalue problems to generalized eigenvalue problems, now enables to extract the eigenvalues of the nonlinear eigenvalue problems given by the BEM. This method is also called projection method because the eigenspace is also reduced to smaller one that can be chosen as one wishes. In contrast to the original eigenspace, the computing cost of the reduced eigenspace is negligible. Moreover, the master-worker type algorithm make it easier to use in PC clusters or multi-core computers. The colleagues of the author have performed a exploration work [53].

In this thesis, a new methodology based on the BEM and contour integral method for the calculation of eigenfrequencies of the structures related to phononic crystals is proposed, and is applied to the analyses of band structures of phononic structures.

As a starting point, the resonances of homogenous acoustic cavities are considered. For undamped free vibration, only real eigenvalues are required, however, due to the formulations provided by the BEM, spurious eigenvalues exist. These spurious eigenvalues contain both real and complex numbers. It is easy to identify the complex spurious eigenvalues from the numerical results. The identification of real spurious eigenvalues, however, requires the boundary integral equation provided by Burton-Miller's method which moves the real spurious eigenvalues off the real axis.

After the preparing work is done, the method is applied to the band calculation of phononic structures. Taking the BEM as the tool for the analysis of photonic/phononic crystals, there are two ways of applying the Bloch theorem to the numerical models: one is to use a quasi-periodic fundamental solution instead of the conventional fundamental solution [41], the other is to give the Bloch periodic boundary condition on the boundary of a unit cell. The former way results in a nonlinear eigenvalue problem and the issue of the convergence of quasi-periodic fundamental solution has to be considered. The latter way requires the extra discretization for boundary of a unit cell. In our research, the latter way of applying Bloch theorem is adopted, since it provides the whole reciprocal space.

The proposed methodology combining of the BEM and the contour integral method is examined in the practical problems for the resonances of 2D and 3D acoustic cavities. Then the author discusses applications of the proposed method to various

phononic structures in two dimensions. The effectiveness of the method to analyze phononic structures is demonstrated through numerical examples.

1.2 Organization of the thesis

The thesis is organized as follows.

- Chapter II

A new BEM-based methodology is proposed to calculate band structures of given phononic structures.

The difficulties resulting from the application of the BEM to eigenvalue problems are described. The nonlinear eigenvalue problems formulated by the BEM are presented by considering a simple case of the Helmholtz equation. Starting from the weighted residual form, the boundary integral equation that shows a nonlinear expression for the eigenvalue parameter is derived. In particular, spurious eigenvalue problems are also introduced by showing the spurious eigenequations of an annular structure which is a interior problem but has a multiply connected domain. Since phononic structures are always considered as multiply connect domains, spurious eigensolutions are also obtained in the numerical simulations. To overcome the spurious solutions, Burton-Miller's method is introduced.

Similar properties of photonic crystals for phononic structure are introduced. Bloch wave function for the mechanical waves propagating in phononic structures is described. Various structures of crystals and their first Brillouin zones are introduced, and the corresponding phononic structures that exhibit the same characteristics are given. Next, the BEM modeling for the phononic structures is presented. Without domain discretization, simple models are created.

- Chapter III

Being also considered as a new methodology for the eigenvalue problems, the proposed method is applied to the analyses of a 2D square acoustic cavity. Furthermore, the eigenfrequencies of 3D acoustic cavities are computed.

For the eigenfrequency computation for the 2D cavity, a relatively large threshold $\delta = 10^{-6}$ is chosen for the rank detection of the Hankel matrix to filter out the meaningful singular values. Also for the 3D case, by observing the behavior of the singular values against the number of collocation points used for evaluating the contour integral, a relatively large threshold value can be determined to filter out the

meaningful singular values. The threshold is not unique for different models. If a multiply connected domain is considered as an acoustic cavity, the boundary of the inclusion generates spurious eigenfrequencies of real numbers [54]. To identify these spurious solutions, the proposed methodology employs the boundary integral equation provided by Burton-Miller's method by which the components with large imaginary parts are added to the real spurious eigenvalues. By observing the imaginary parts of the numerical results, the true eigensolutions can be identified.

- Chapter IV

A new approach based on the BEM and the block SS method for the analyses of band structure of phononic structures is proposed and applied to the band calculation of acoustic phononic structure governed by the Helmholtz equation. The band gaps are observed correctly both in homogenous and composite phononic structures. By applying the Bloch periodic boundary condition on the virtual boundary of a unit cell, the analyzed problem can be considered as an interior problem with a multiply connect domain. Therefore, the real spurious eigenfrequencies are also observed as horizontal lines in the band structures. Again, Burton-Miller's method is used for eliminating the spurious solutions.

- Chapter V

An important difference between elastic waves in solids and acoustic wave in the air is that an elastic wave in a homogeneous solid has three independent polarizations: two of them are transverse and one is longitudinal. However, an acoustic wave has just one longitudinal polarization. To investigate the more complicated wave propagations, the proposed approach is applied to the band calculation for elastic phononic structures. In order to improve the efficiency of the contour integral method for computing the real eigenfrequencies, a fusiform contour integral path is employed to exclude the complex solutions. Three typical elastic phononic structures are constructed: the bi-material phononic structure which has dense/stiff scatterers imbedded in light/soft host, presenting a band gap based on Bragg scattering; the unidirectional phononic periodic plate which has the unit cell with traction-free boundaries, presenting a flat band structure; the phononic structure which has the imbedded dense/stiff scatterers coated with a light/soft material, presenting a band gap based on the local resonance. Numerical results demonstrate the effectiveness of the method for elastic materials.

- Chapter VI

For importance of practical problems, an investigation on finite/infinite unidirectional phononic plates which have 2D cells arranged along one direction periodically, is carried out.

The band structures of the infinite unidirectional phononic plates are computed by using the proposed approach. The dispersion relations for both acoustic and elastic infinite unidirectional phononic plates are obtained. In the dispersion relations, the stop bands and pass bands are identified. For the finite case, the bounded input and output domains are connected with finite layers of unidirectional phononic plates. To investigate the wave transmission in these finite structures, a size-reduced coefficient matrix is derived utilizing the transfer matrix formulated by the BEM repeatedly. The wave transmission is observed against the frequency and the number of layer. With a sufficient number of layers of cells, the finite structures also exhibits the frequency-banded nature which can be enhanced through increasing the number of cells. Furthermore, the whole finite structure including the input and output domains is treated as a free vibration problem and its eigenfrequencies are extracted by using the block SS method. This is a more direct way to identify the frequency-banded nature of the finite structures.

- Chapter VII

Conclusions of the thesis are presented.

CHAPTER II

Overview of BEM-based methodology for band calculation of phononic structures

2.1 BEM for eigenvalue problems

2.1.1 Nonlinear eigenvalue problems resulting from BEM

Different from nonlinear eigenvalue problems formulated by the BEM, a generalized eigenvalue problem is given by the FEM [44] as follows:

$$(\mathbf{K} - \omega^2 \mathbf{M})\mathbf{x} = \mathbf{0}, \tag{2.1}$$

where the circular frequency ω is involved in the eigenvalue problem explicitly. But for the BEM, since the fundamental solutions are adopted as the weighted functions, the coefficient matrix involve ω implicitly in each matrix element. Let us take a simple case of the Helmholtz equation as an example:

$$\nabla^2 p(x) + k^2 p(x) + f(x) = 0 \qquad \text{in } \Omega, \tag{2.2}$$

where x is a point in Ω, Ω is the domain of the problem, $k = \omega/C$ is the wave number, with circular frequency ω and wave speed C, and $f(x)$ is a source term.

The integral representation for $u(x)$ can be derived by starting from the following weighted residual form:

$$\int_{\Omega} \left\{ \nabla^2 p(y) + k^2 p(y) + f(y) \right\} p^*(x, y) \, \mathrm{d}\Omega_y = 0. \tag{2.3}$$

where the fundamental solutions $p^*(x, y)$ for the Helmholtz equation include the ex-

ponential function e^r or the zeroth order Hankel function of the first kind $\mathrm{H}_0^{(1)}(r)$ where $r = |x - y|$ and Ω_y denotes the integration with respect to point y. Moreover, for elastodynamic problems, the fundamental solutions contain the Bessel functions. The fundamental solutions have highly nonlinear property.

Integrating by parts the left-hand side of the above form twice gives:

$$\int_S p^*(x,y)\frac{\partial p(y)}{\partial n(y)}\,\mathrm{d}S_y - \int_S \frac{\partial p^*(x,y)}{\partial n(y)}p(y)\,\mathrm{d}S_y + \int_\Omega p^*(x,y)f(y)\,\mathrm{d}\Omega_y + \int_\Omega \left\{\nabla^2 p^*(x,y) + k^2 p^*(x,y)\right\} p(y)\,\mathrm{d}\Omega_y = 0, \tag{2.4}$$

where $S = \partial\Omega$, and $\frac{\partial(\cdot)}{\partial n}$ denotes the normal derivative at the corresponding point on the boundary S. Recall the fundamental solution $p^*(x,y)$ satisfies

$$\nabla^2 p^*(x,y) + k^2 p^*(x,y) + \delta(x-y) = 0, \tag{2.5}$$

where $\delta(x-y)$ is Dirac's delta function in three-dimensional space. Therefore, the last domain integral term of the left-hand side of Eq. (2.4) becomes as

$$\int_\Omega \{-\delta(x-y)\}\, p(y)\,\mathrm{d}\Omega_y = -p(x), \tag{2.6}$$

and hence, we have the following integral representation:

$$p(x) = \int_S p^*(x,y)\frac{\partial p(y)}{\partial n(y)}\,\mathrm{d}S_y - \int_S \frac{\partial p^*(x,y)}{\partial n(y)}p(y)\,\mathrm{d}S_y + \int_\Omega p^*(x,y)f(y)\,\mathrm{d}\Omega_y, \quad x \in \Omega. \tag{2.7}$$

Moving the point x to the boundary S and discretizing the boundary integral equation with Ne constant elements, without the source term, we have the form as follows:

$$\frac{1}{2}p^i(x) = \sum_{j=1}^{Ne}\left[\left(\int_{S_j} p^*(x,y)\,\mathrm{d}S_y\right)\frac{\partial p^j(y)}{\partial n(y)}\right] - \sum_{j=1}^{Ne}\left[\left(\int_{S_j}\frac{\partial p^*(x,y)}{\partial n(y)}\,\mathrm{d}S_y\right)p^j(y)\right]. \tag{2.8}$$

Let i vary from 1 to Ne, and then we have Ne linear equations as follows:

$$\mathbf{Bp} = \mathbf{Gq}, \tag{2.9}$$

where $\mathbf{p} = \{p^1, p^2, ..., p^{Ne}\}^T$ and $\mathbf{q} = \{\frac{\partial p^1}{\partial n}, \frac{\partial p^2}{\partial n}, ..., \frac{\partial p^{Ne}}{\partial n}\}^T$.

By substituting the homogenous boundary condition of free vibration or the periodic boundary condition to those equations and moving all the unknowns to the left hand side, we obtain a nonlinear eigenvalue problem as follows:

$$\mathbf{A}(\omega)\mathbf{x} = \mathbf{0}. \tag{2.10}$$

where $\mathbf{x}$ includes all the unknowns. In the coefficient matrix of Eq. (2.10), each element of the matrix is related to the integrals in Eq. (2.8) which has fundamental solutions as the integrands.

2.1.2 Spurious eigenvalues for multiply connect domains

The nonlinear eigenvalue problem in Eq. (2.10) has not only a highly nonlinear nature, but also yield spurious eigenvalues when the analyzed domain is infinite or multiply connected [55, 54]. Especially, for the latter case, which is frequently encountered in the investigation of phononic structures, both real and complex spurious eigenvalues exist.

Considering a 2D multiply connected annular domain depicted in Fig. 2.1, where S_{I} denotes the inner boundary, and S_{U} denotes the outer boundary, the eigenequations of this special case are given in Eqs. (2.11)-(2.19) [54].

For the boundary condition given as $u = 0$ on S_{I} and $u = 0$ on S_{U}, the true eigenequation is as follows:

$$J_n(kr_1)Y_n(kr_2) - J_n(kr_2)Y_n(kr_1) = 0 \tag{2.11}$$

and the spurious eigenequation is written as

$$J_n(kr_1) = 0, \tag{2.12}$$

where J_n denotes the Bessel function of the first kind and Y_n denotes the Bessel function of the second kind. For the boundary condition given as $u = 0$ on S_{I} and

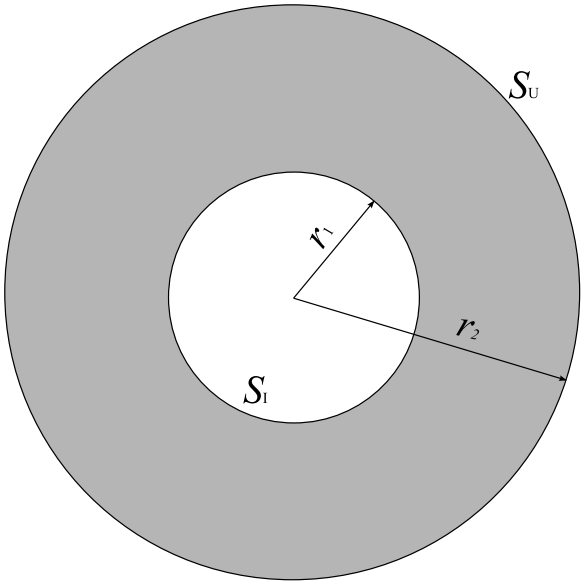

Figure 2.1: A multiply connected annular domain.

$\frac{\partial u}{\partial n} = 0$ on S_{U}, the true eigenequation is as follows:

$$J_n(kr_1)Y_n'(kr_2) - J_n'(kr_2)Y_n(kr_1) = 0 \tag{2.13}$$

and the spurious eigenequation is written as

$$J_n(kr_1) = 0, \tag{2.14}$$

where $(\cdot)'$ denotes the first derivative of $(\cdot)$. For the boundary condition given as $\frac{\partial p}{\partial n} = 0$ on S_{I} and $p = 0$ on S_{U}, the true eigenequation is as follows:

$$J_n'(kr_1)Y_n(kr_2) - J_n(kr_2)Y_n'(kr_1) = 0, \tag{2.15}$$

and the spurious eigenequation is written as

$$J_n(kr_1) = 0. \tag{2.16}$$

For the boundary condition given as $\frac{\partial p}{\partial n} = 0$ on S_{I} and $\frac{\partial p}{\partial n} = 0$ on S_{U}, we have the true eigenequation:

$$J_n'(kr_1)Y_n'(kr_2) - J_n'(kr_2)Y_n'(kr_1) = 0, \tag{2.17}$$

and the spurious eigenequation:

$$J_n(kr_1) = 0. \tag{2.18}$$

It can be seen that the domain shown in Fig. 2.1 always yields spurious eigenvalues determined by $J_n(kr_1) = 0$. Moreover, there is an extra nonzero factor of eigenequation for real kr_1 in each case:

$$Y_n(kr_1) - \mathrm{i}J_n(kr_1) = 0, \tag{2.19}$$

which is equivalent to $\mathrm{i}H_n^{(1)}$ wherein i is the imaginary unit. The zeros of $H_n^{(1)}$ are complex spurious eigenvalues. The contour integral method adopts the contour integral in the complex plane, and the zeros of $H_n^{(1)}$ are also obtained. For the undamped linear vibration of acoustic and elastic problem, there is no complex eigenvalue for interior problem, therefore, the complex spurious solutions obtained by the contour integral method can be removed from the results.

For the real spurious eigenvalues resulted by the eigenequations like $J_n(kr_1) = 0$, it is difficult to identify them from the true solutions that are also real numbers, so we employ Burton-Miller's method to eliminate them.

2.1.3 Burton-Miller's method

Let us see the integral equation shown in the previous section in Eq. (2.7). Taking the normal derivative of Eq. (2.7) at point x, the integral equation becomes as follows:

$$\begin{aligned}\frac{\partial p(x)}{\partial n(x)} = \int_S \frac{\partial p^*(x,y)}{\partial n(x)} \frac{\partial p(y)}{\partial n(y)} \,\mathrm{d}S_y - \int_S \frac{\partial^2 p^*(x,y)}{\partial n(y)\partial n(x)} p(y) \,\mathrm{d}S_y \\ + \int_\Omega \frac{\partial p^*(x,y)}{\partial n(x)} f(y) \,\mathrm{d}\Omega_y, \quad x \in \Omega.\end{aligned} \tag{2.20}$$

Without considering the source terms, the combination form as (2.7)+μ(2.20) [55]:

$$\begin{aligned}u(x) + \mu \frac{\partial p(x)}{\partial n(x)} = \int_S p^*(x,y) \frac{\partial p}{\partial n}(y) \,\mathrm{d}S_y + \mu \int_S \frac{\partial p^*(x,y)}{\partial n(x)} \frac{\partial p(y)}{\partial n(y)} \,\mathrm{d}S_y \\ - \int_S \frac{\partial p^*(x,y)}{\partial n(y)} p(y) \,\mathrm{d}S_y - \mu \int_S \frac{\partial^2 p^*(x,y)}{\partial n(y)\partial n(x)} p(y) \,\mathrm{d}S_y, \quad x \in \Omega.\end{aligned} \tag{2.21}$$

is proposed for the elimination of the real spurious eigenvalues. The coefficient μ is

not unique for different models. The choice of μ is another research topic that is beyond the scope of this thesis.

2.2 Phononic structure

2.2.1 Bloch wave

The Bloch wave or Bloch state is usually considered as a wave function of electromagnetic waves propagating in a periodic medium. Similarly, the mechanical waves that exist in a periodic acoustic medium or composite solid structure, also present the properties of the Bloch waves. The wave function can be written as

$$U_{n\mathbf{k}}(\mathbf{r}) = e^{\mathrm{i}\mathbf{k}\cdot\mathbf{r}} u_{n\mathbf{k}}(\mathbf{r}) \tag{2.22}$$

where $\mathbf{r}$ denotes the position in the periodic structure, $U_{n\mathbf{k}}$ can be defined as various physical quantities such sound pressure, displacements, etc., n denotes the number of eigenvalues for a same wave vector $\mathbf{k}$, and $u_{n\mathbf{k}}$ is a periodic function in the space of the periodic structure, written as follows:

$$u_{n\mathbf{k}}(\mathbf{r} + \mathbf{L}) = u_{n\mathbf{k}}(\mathbf{r}) \tag{2.23}$$

where $\mathbf{L}$ is the lattice vector.

2.2.2 First Brillouin zone

The first Brillouin zone is usually introduced in solid state physics and considered as a primitive cell in reciprocal space. In a single Brillouin zone, the solutions of waves can be completely characterized, furthermore, the irreducible Brillouin zone, which is the first Brillouin zone reduced by all symmetries in the point group of the lattice. The examples of the first Brillouin zones for 1D, 2D, 3D, crystal lattices are shown in Figs. 2.2-2.5. More simply, in the band calculation for the crystals, one can just let the wave vector $\mathbf{k}$ vary along the boundary of irreducible Brillouin zone.

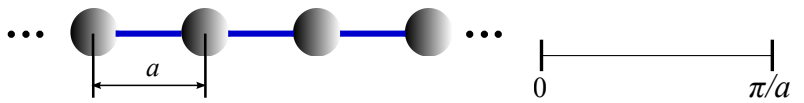

(a) 1D lattices (b) The irreducible Brillouin zone

Figure 2.2: The 1D lattice (a) and its irreducible Brillouin zone (b).

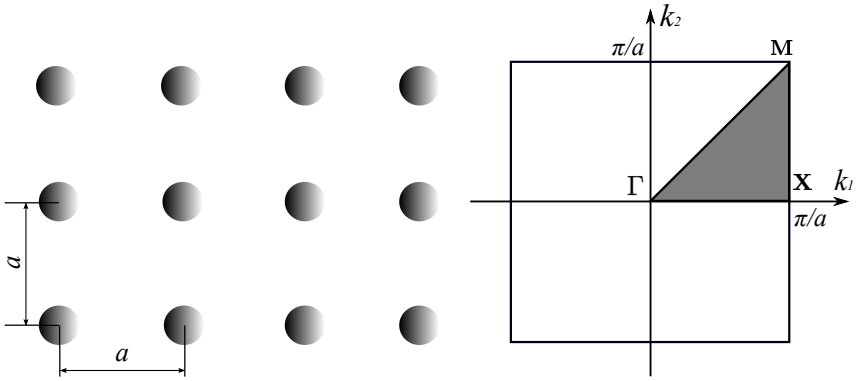

(a) 2D square lattices (b) The irreducible Brillouin zone

Figure 2.3: The 2D square lattice (a) and its irreducible Brillouin zone (shade region) (b).

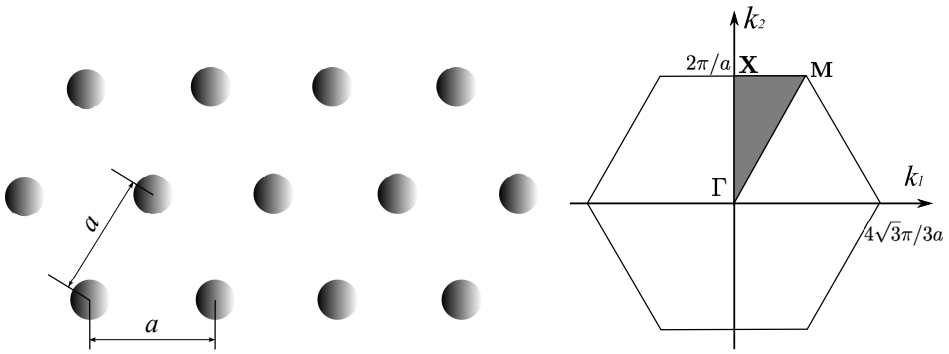

(a) 2D square phononic structure (b) The irreducible Brillouin zone

Figure 2.4: The 2D triangular lattice (a) and its irreducible Brillouin zone (shade region) (b).

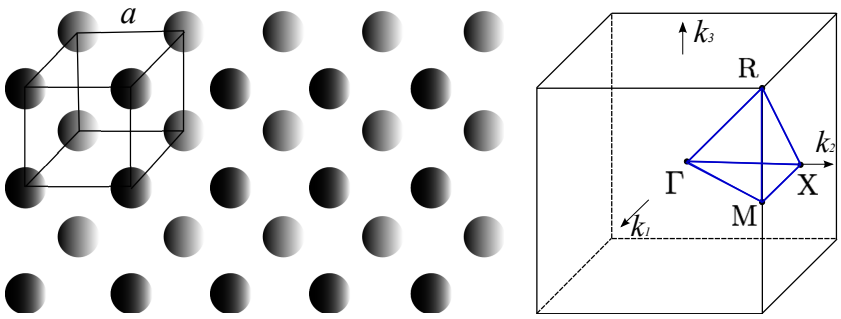

(a) 3D simple cubic lattices

(b) The irreducible Brillouin zone

Figure 2.5: The 3D simple cubic lattice (a) and its irreducible Brillouin zone (surrounded by blue lines) (b).

For the phononic structures, as macroscopical problems, have the inclusions distributed in the host periodically. These phononic structures in Fig.2.6 also have the properties of crystals.

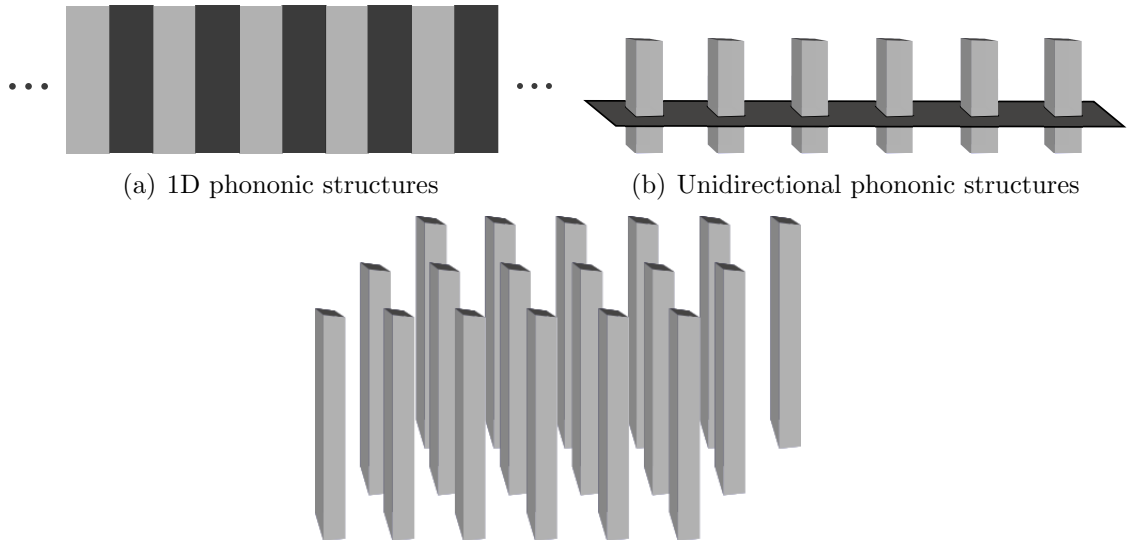

(a) 1D phononic structures

(b) Unidirectional phononic structures

(c) 2D phononic structures

Figure 2.6: The 1D phononic structure (a), the unidirectional phononic plate (b) and 2D phononic structures (c).

2.2.3 BEM modeling for unit cells of phononic structures

In the boundary integral equations, in contrast to the weak form employed in the FEM, the BEM does not have any domain integral terms unless sources over areas

are given to the domain. Due to this advantage of the BEM, the numerical model for phononic structures can be preprocessed easily. The BEM models for 2D and 3D phononic structures are shown in Fig. 2.7.

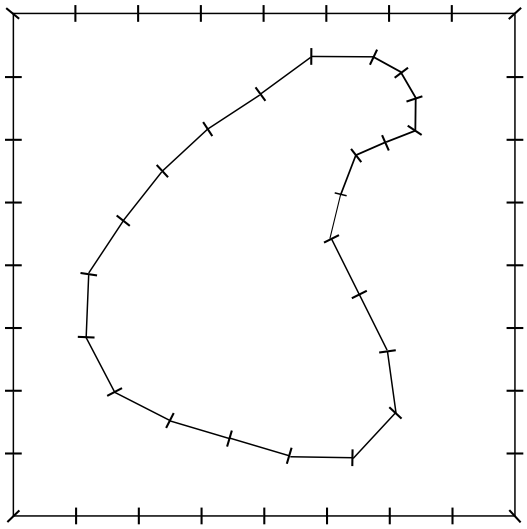

(a) The model for a cell of 2D phononic structure discretized by boundary elements

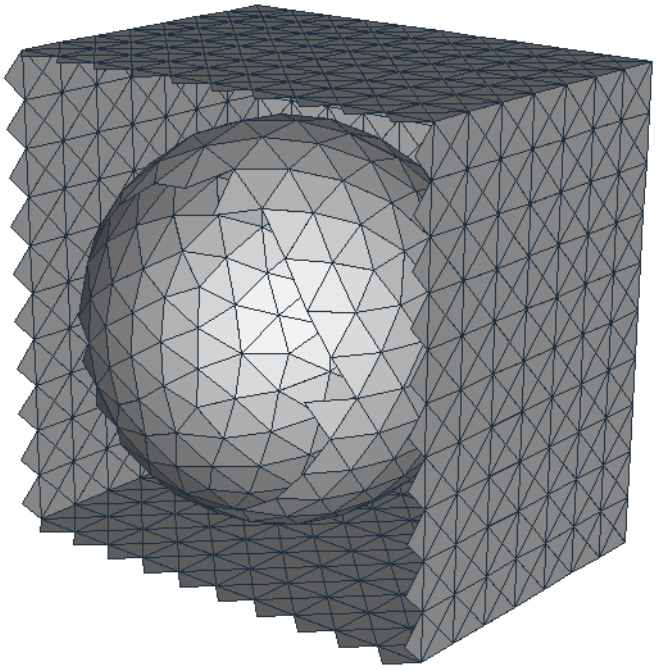

(b) The model for a cell of 3D phononic structure (cross-section view) discretized by boundary elements

Figure 2.7: The 2D phononic BEM model (a) and 3D phononic BEM model (b).

In the BEM models, only the boundaries of the unit cell and inclusion are constructed. It is very convenient to apply the Bloch periodic boundary condition to the

surface of the unit cell.

2.3 Eigensolver: the contour integral method

2.3.1 Brief introduction for the contour integral method

The contour integral method adopted in this thesis is the Sakurai-Sugiura (SS) method [52] which is named after Sakurai and Sugiura who introduce their method as an eigensolver for generalized eigenvalue problems. Based on the root finding method for an analytic function, the SS method projects the original eigenspace to a subspace associated with the eigenvalues located in a domain surrounded by a closed Jordan curve as shown in Fig. 2.8. The reduced eigenspace is determined by the Hankel matrices which formed by moments in different orders. These moments are calculated by evaluating a contour integral along the Jordan curve numerically. Later, the method is reformulated by using the resolvent theory in [56], wherein the filter function can be observed explicitly. Furthermore, the block version of the SS method is developed to overcome the problem of degenerated eigenvalues. Different from the original SS method, instead of using one initial vector, the block version employs a set of the initial vectors and the Hankel matrices are formed by moment matrices. For nonlinear eigenvalue problems, the method is proposed in [1], wherein the SS method is derived from Smith form for analytic matrix functions. A similar approach is proposed by Wolf-Jürgen Beyn who use complex integrals of the resolvent operator [57]. The block SS method not only is able to solve the degenerated eigenvalues, but also enables us to acquire more eigenvalues with lower-order moment matrices.

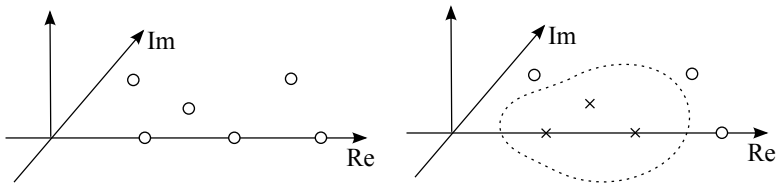

(a) The original eigenspace (The circular symbols denote the eigenvalues of the original eigenspace)

(b) The reduced eigenspace by the contour integral (the crossed symbols denote the eigenvalues in the reduced eigenspace, and the dashed line denotes the contour integration path)

Figure 2.8: The reduction of the eigenspace by the block SS method.

2.3.2 Block SS method [1]

Let us consider a nonlinear eigenvalue problem written in the form as follows

$$\mathbf{A}(z)\mathbf{x} = \mathbf{0}, \tag{2.24}$$

where the size of $\mathbf{A}(z)$ is equal to Ne. In the block version SS method, $Ne \times l$ matrix $\mathbf{U}$ and $Ne \times l$ matrix $\mathbf{V}$ ($l \ll Ne$) are used to construct the following matrix function $\mathbf{T}(z)$:

$$\mathbf{T}(z) \;=\; \mathbf{U}^H \mathbf{A}(z)^{-1} \mathbf{V}, \tag{2.25}$$

where $(\cdot)^H$ denotes the conjugate transpose, $\mathbf{U}$ and $\mathbf{V}$ are arbitrary nonzero matrices, and $\mathbf{U} = \mathbf{V}$. It is noted that, in the original version of the SS method, arbitrary nonzero vectors $\mathbf{u}$, $\mathbf{v}$ are used instead of the above matrices $\mathbf{U}$, $\mathbf{V}$.

The moment matrices are given as follows:

$$\mathbf{M}_m = \frac{1}{2\pi \mathrm{i}} \int_{\Gamma} \mathbf{T}(z) z^m \mathrm{d}z, \tag{2.26}$$

where Γ is a positively oriented closed Jordan curve in the complex plane for k, then two Hankel matrices $\mathbf{H}_{Kl}^{<}$ and $\mathbf{H}_{Kl}$ can be formed by using the moment matrices $\mathbf{M}_m$, where m varies from 0 to $2K-1$:

$$\mathbf{H}_{Kl} \;=\; \begin{pmatrix} \mathbf{M}_0 & \mathbf{M}_1 & \cdots & \mathbf{M}_{K-1} \\ \mathbf{M}_1 & \mathbf{M}_2 & \cdots & \mathbf{M}_K \\ \vdots & \vdots & \ddots & \vdots \\ \mathbf{M}_{K-1} & \mathbf{M}_K & \cdots & \mathbf{M}_{2K-2} \end{pmatrix}, \tag{2.27}$$

$$\mathbf{H}_{Kl}^{<} \;=\; \begin{pmatrix} \mathbf{M}_1 & \mathbf{M}_2 & \cdots & \mathbf{M}_K \\ \mathbf{M}_2 & \mathbf{M}_3 & \cdots & \mathbf{M}_{K+1} \\ \vdots & \vdots & \ddots & \vdots \\ \mathbf{M}_K & \mathbf{M}_{K+1} & \cdots & \mathbf{M}_{2K-1} \end{pmatrix}. \tag{2.28}$$

By solving the eigenvalues of the matrix pencil $\mathbf{H}_{Kl}^{<} - k\mathbf{H}_{Kl}$:

$$\mathbf{H}_{Kl}^{<}\mathbf{w} = k\mathbf{H}_{Kl}\mathbf{w}, \tag{2.29}$$

the eigenvalues $k_1, k_2, \cdots, k_K$ located in the closed curve Γ can be obtained.

It can be proved that $k_1, k_2, \cdots, k_K$ are the eigenvalues of the original problem Eq. (2.24) located inside Γ [1].

Let $(k_j, \mathbf{w}_j)$ be the eigenpairs of the generalized eigenvalue problem (2.29), and let

$$\mathbf{S}_m = \frac{1}{2\pi \mathrm{i}} \int_{\Gamma} z^m \mathbf{A}(\mathbf{z})^{-1} \mathbf{V} \mathrm{d}z, m = 0, 1, \cdots, K-1, \tag{2.30}$$

where $\mathbf{S}_m$ are $Ne \times l$ matrix, with which one can form the matrix $\mathbf{S} = (\mathbf{S}_0, \mathbf{S}_1, \cdots, \mathbf{S}_{M-1})$, which is a $Ne \times Kl$ matrix. Then, the eigenvectors can be solved by using the formula:

$$\mathbf{x}_j = \mathbf{S}\mathbf{w}_j, \tag{2.31}$$

where $\mathbf{x}_j$ are eigenvectors of the original nonlinear eigenvalue problem. The proofs of the theorems are given in [1].

The contour integrals in Eqs. (2.26) and (2.30) are carried out numerically using N-points trapezoidal rule. A circlular integration path is defined as $\Gamma = \gamma + \rho e^{\mathrm{i}\theta} (0 \leq \theta < 2\pi)$ and the collocation points are $p_j = \gamma + \rho e^{2\pi \mathrm{i}(j+1/2)/N} (j = 0, 1, 2, \ldots, N-1)$. $\mathbf{M}_m$ and $\mathbf{S}_m$ are calculated numerically:

$$\mathbf{M}_m \approx \hat{\mathbf{M}}_m = \frac{1}{N} \sum_{j=0}^{N-1} \left(\frac{p_j - \gamma}{\rho} \right)^{m+1} \mathbf{T}(p_j), \tag{2.32}$$

$$\mathbf{S}_m \approx \hat{\mathbf{S}}_m = \frac{1}{N} \sum_{j=0}^{N-1} \left(\frac{p_j - \gamma}{\rho} \right)^{m+1} \mathbf{A}(p_j)\mathbf{V}. \tag{2.33}$$

As the number of eigenvalues located inside Γ is not known in advance, the number of the eigenvalues has to be determined. To this end, the singular value decomposition (SVD) of the Hankel matrix is performed. After the Hankel matrices are formed, the SVD of $\mathbf{H}_{Kl}$ is carried out as follows:

$$\mathbf{H}_{Kl} = \mathbf{C}\mathbf{\Sigma}\mathbf{E}^H, \tag{2.34}$$

where $\mathbf{C}$ is a $Kl \times Kl$ complex unitary matrix ,$\mathbf{\Sigma}$ is a $Kl \times Kl$ diagonal matrix with nonnegative real numbers (singular values of $\mathbf{H}_{KL}$) on the diagonal, and $\mathbf{E}^H$ is the conjugate transpose of $\mathbf{E}$ which is a $Kl \times Kl$ complex unitary matrix. The $\mathbf{\Sigma}$ matrix

can be written as

$$\mathbf{\Sigma} = \begin{pmatrix} \sigma_1 & & & & & & \\ & \sigma_2 & & & & & \\ & & \ddots & & & & \\ & & & \sigma_{m'} & & & \\ & & & & \sigma_{m'+1} & & \\ & & & & & \ddots & \\ & & & & & & \sigma_{Kl} \end{pmatrix}, \tag{2.35}$$

where $\sigma_1, \sigma_2, \ldots, \sigma_{m'}, \sigma_{m'+1}, \ldots, \sigma_{Kl}$ are the singular values of the Hankel matrix and are defined as positive. The singular values are listed in decreasing order $\sigma_1 > \sigma_2, \ldots, > \sigma_{Kl}$. Let δ be a positive threshold value and omit the small singular values $\sigma_{m'+1} < \delta \cdot \ \sigma_1$, then a diagonal $m' \times m'$ matrix is obtained as follows:

$$\mathbf{\Sigma}_{m'} = \begin{pmatrix} \sigma_1 & & & \\ & \sigma_2 & & \\ & & \ddots & \\ & & & \sigma_{m'} \end{pmatrix}. \tag{2.36}$$

Let $\mathbf{H} = \mathbf{C}^H \mathbf{H}_{Kl}^{<} \mathbf{E}$, then Eq. (2.29) becomes the form as

$$\mathbf{H}\bar{\mathbf{w}} = k\mathbf{\Sigma}\bar{\mathbf{w}}, \tag{2.37}$$

where $\bar{\mathbf{w}} = \mathbf{E}^H \mathbf{w}$.

Let $\mathbf{H}' = \mathbf{H}(1 : m', 1 : m')$, and $\mathbf{H}_{m'} = {\mathbf{\Sigma}_{m'}}^{-\frac{1}{2}} \mathbf{H}' \mathbf{\Sigma}_{m'}^{-\frac{1}{2}}$, then the problem becomes a linear eigenvalue problem for $\mathbf{H}_{m'}$

$$\mathbf{H}_{m'}\mathbf{y} = \lambda\mathbf{y}. \tag{2.38}$$

If it is necessary to know the number of eigenvalues located in the selected range in advance, the stochastic estimation [58] of the number for eigenvalues is proposed as follows:

$$m' = \frac{1}{2\pi \mathrm{i}} \oint_{\Gamma} \mathrm{tr} \left(\mathbf{A}(z)^{-1} \frac{\mathrm{d}\mathbf{A}(z)}{\mathrm{d}z} \right) \mathrm{d}z, \tag{2.39}$$

where m' is the number of eigenvalues located in Γ, and $\mathrm{tr}\,(\mathbf{A}(z))$ is the matrix trace

of $\mathbf{A}(z)$.

A numerical approximation of m' can also be carried out by using trapezoidal rule:

$$m' \approx \hat{m'} = \frac{1}{l} \sum_{j=0}^{N-1} w_j \sum_{i=1}^{l} (\mathbf{v}_i^T \mathbf{A}(p_j)^{-1} \mathbf{A}'(p_j) \mathbf{v}_i), \tag{2.40}$$

where $w_j = \frac{\rho}{N} \mathrm{e}^{\frac{2\pi \mathrm{i}}{N}(j+1/2)}$ are the wights.

In Eqs. (2.32) and (2.33), the integration path is shifted and scaled as well as the eigenvalues in order to retain numerical accuracy. Let $\lambda_1, \lambda_2, \ldots, \lambda_{m'}$ be the eigenvalues of (2.38), then the eigenvalues can be recovered by

$$k_j = \rho \lambda_j + \gamma. \tag{2.41}$$

where ρ and γ are the radius and center of the circular integration path respectively.

In SVD (2.34), let $\mathbf{E} = \{\mathbf{e}_1, \mathbf{e}_2, \ldots, \mathbf{e}_{Kl}\}$, $\mathbf{e}_j^H$ be the row vectors of $\mathbf{E}^H$, let $\mathbf{E}_{m'} = \{\mathbf{e}_1, \mathbf{e}_2, \ldots, \mathbf{e}_{m'}\}$, then we have

$$\mathbf{w}_j = \mathbf{E}_{m'} \mathbf{\Sigma}_{m'}^{-\frac{1}{2}} \mathbf{y}_j, \tag{2.42}$$

substituting Eq. (2.42) into Eq. (2.31), we can recover the eigenvectors by

$$\mathbf{x}_j = \mathbf{S} \mathbf{E}_{m'} \mathbf{\Sigma}_{m'}^{-\frac{1}{2}} \mathbf{y}_j. \tag{2.43}$$

Error analysis of contour integral method is given in [57]. The error of the trapezoidal rule for a circle integration path is

$$\mathrm{Error}_N(f) = \frac{1}{2\pi \mathrm{i}} \int_{\Gamma} f(z) dz - \frac{\rho}{N} \sum_{j=0}^{N-1} f(\rho \omega_N^j) \omega_N^j, \quad \omega_N = \exp\left(\frac{2\pi \mathrm{i}}{N}\right), \tag{2.44}$$

where f is a holomorphic function on annulus

$$\left\{ z \in \mathbb{C} : \frac{1}{a_-} < \frac{|z|}{\rho} < a_+ \right\}, \quad a_\pm > 1.$$

For all $1 < R_- < a_-$,and $1 < R_+ < a_+$, $\mathrm{Error}_N(f)$ satisfies

$$\mathrm{Error}_N(f) \leqslant \max_{|z|=R_+\rho} |f(z)|G(R_+^{-N}) + \max_{R_-|z|=\rho} |f(z)|G(R_-^{-N}), \tag{2.45}$$

where $G(x) = x/(1-x), \quad x \neq 1$.

Referring to the corollary in [57], the maximum error of the eigenvalues is given as

$$\max_{j=1,\ldots,m} |k_j^* - k_j| \leqslant \bar{C}[R_-^{N-\kappa+1} + R_+^{N+\kappa-1}], \tag{2.46}$$

where k_j^* denotes the eigenvalue located inside Γ, k_j denotes the numerical result, $\bar{C}$ is a constant depending on $\mathbf{A}$,$\mathbf{U}$,and $\mathbf{V}$, $R_\pm$ here are

$$R_- = \max_{|k^*-\gamma|<\rho} \frac{|k^*-\gamma|}{\rho}, \tag{2.47}$$

$$R_+ = \max_{|k^*-\gamma|>\rho} \frac{\rho}{|k^*-\gamma|}, \tag{2.48}$$

where k^* is the eigenvalues of (2.24).

The algorithm for the block SS method can be the following steps:

1. Choose an appropriate integration path and input U, $V \in \mathbb{C}^{Ne\times L}$ (commonly set $\mathbf{U} = \mathbf{V}$), N, K, l, δ.

2. Set collocation points p_j, $j = 0, 1, ..., N-1$

3. Compute $\mathbf{A}(p_j)^{-1}\mathbf{V}$, $j = 0, 1, ..., N-1$

4. Compute $\hat{\mathbf{S}}_m$, $m = 0, 1, ..., 2K-1$

5. Compute $\hat{\mathbf{M}}_m = \mathbf{U}^{\mathrm{H}}\hat{\mathbf{S}}_m$, $m = 0, 1, ..., 2K-1$

6. Construct Hankel matrices $\mathbf{H}_{Kl}$ and $\mathbf{H}_{Kl}^{<} \in \mathbb{C}^{Kl\times Kl}$

7. Detect the rank of $\mathbf{H}_{Kl}$ by performing SVD

8. Filter out meaningful singular values components $\sigma_j < \delta \cdot \sigma_1$ and convert the Hankel matrix $\mathbf{H}_{Kl}^{<}$ to the form as

   $\mathbf{H} = \mathbf{C}^{\mathrm{H}}\mathbf{H}_{Kl}^{<}\mathbf{E}$,

   $\mathbf{H}' = \mathbf{H}(1 : m', 1 : m')$,

$\mathbf{H}_{m'} = \mathbf{\Sigma}_{m'}^{-\frac{1}{2}} \mathbf{H}' \mathbf{\Sigma}_{m'}^{-\frac{1}{2}}$

If the threshold δ can not be used, then we suggest carrying out the estimation for m'.

9. Compute the eigensolutions of the standard linear eigenvalue problem $\mathbf{H}_{m'}\mathbf{y} = \lambda\mathbf{y}$

10. Construct $\mathbf{S} = (\mathbf{S}_0, \mathbf{S}_1, ..., \mathbf{S}_{M-1})$

11. Compute $k_1, k_2, ...k_{m'}$, $\mathbf{x}_j = \mathbf{S}\mathbf{E}_{m'}\mathbf{\Sigma}_{m'}^{-\frac{1}{2}}\mathbf{y}_j$

CHAPTER III

Eigensolutions of Homogenous Domains

3.1 Introduction

In the field of mechanics and physics, we need to solve boundary value problems of partial differential equations. With an increasing interest in fast algorithms such as fast multipole method [47, 48, 49, 59] and adaptive cross approximation [50, 51], the BEM is becoming a more attractive numerical method for boundary value problems. Eigenvalue analysis is also important in the field such as resonance of structure, principal component analysis and design of auto mobile stereo system, etc. To solve eigenvalue problems by using the BEM is not so easy because, unlike FEM, the system matrix resulting from the BEM involves the eigenvalue parameter implicitly. In this chapter, since we consider homogenous mediums, the wave number k and circular frequency ω have the linear relation $k = \frac{\omega}{C}$, where C is the wave speed. Therefore, in this chapter, k is consider as the eigenvalue parameter. Let us write the system equations as $\mathbf{A}(k)\mathbf{x} = \mathbf{0}$, then zeros of the determinant of the system matrix $\mathbf{A}(k)$ are the eigenvalues, therefore we need to solve a transcendental eigenequation for k, thus, it is extremely difficult to solve the eigenvalues numerically. It is worth, however, investigating the eigensolver based on the BEM, because boundary-only discretization makes a smaller system matrix, and with the same level of DOFs, the BEM may give more accurate results because there is no domain discretization.

Looking into the literatures, over the last three decades, many efforts have been made in applying the BEM to eigenvalue analyses. The direct search method (DSM) [60, 61, 62], which was first employed to extract the eigenvalues of nonlinear eigenvalue problem formulated by the BEM, requires to draw the profile of $\det[\mathbf{A}]$ with respect to k with its incremental variation, and the massive computational costs make it inefficient and time consuming. In addition, it is often very difficult to distinguish

the eigenvalues located in their vicinities.

In order to avoid solving the nonlinear eigenvalue problem directly, some transform methods [63, 64, 65, 66, 67, 68, 69, 70, 71], which may convert the nonlinear eigenvalue problem to a generalized or a standard eigenvalue problem that can be solved by using standard solvers, are developed. Internal cell method (ICM) [63] sets up a generalized eigenvalue problem by treating the term involving k as a internal term in the Helmholtz equation. In the boundary integral equations, the fundamental solution of the Laplace equation is adopted instead of that of the Helmholtz equation, and in addition to the boundary discretization, the domain is divided into internal cells. Nardini and Brebbia proposed an approach named dual reciprocity method (DRM) to free vibration analyses [64, 65], in which the internal term can be transformed to boundary integrals by applying the divergence theorem twice. For acoustic problem, the sound pressure is interpolated using a global shape function, but for elasticity problems, additional internal points or zoned boundary techniques are required, in order to obtain accurate solutions [66]. Furthermore, the efficiency of the DRM for the eigenvalue extraction of two-dimensional acoustic cavities is discussed [67]. Recently, DRM is applied in hybrid variational principle based meshless method to solve eigenvalue problems [68, 69]. To transform the domain integrals into boundary integrals, Nowak and Brebbia [70] proposed the multiple reciprocity method (MRM), which is regarded as an extension of the idea of DRM. This method employs a sequence of functions related to fundamental solution to constitute a set of higher order fundamental solutions. Similarly, Kirkup and Amini [71] applied series expansion method (SEM), which solve the Helmholtz equation by making an equivalent procedure of MRM. This technique is also applied to eigenvalue problems for solid of anisotropy [72] and piezoelectric solid [73]. Advantages and drawbacks for some of these methods are discussed by Kamiya, etc. [74] and Ali [75].

In this Chapter, the block SS method is applied to solve BEM-based nonlinear eigenvalue problem of 2D and 3D acoustic cavities. The standard boundary integral equation and constant triangular elements are used. Without any internal interpolation and discretization, boundary-only discretization results in a more efficient preprocessing and a small sized of the system matrix. For multiply connected domains which includes a internal closed boundary, the methodology yields spurious eigenvalues. Burton-Miller's method is employed, and it is found that the real spurious eigenvalues shift with imaginary parts added. Numerical examples for 2D square, 3D spherical and cubic cavities are given to demonstrate the effectiveness of the proposed methodology for solving eigenfrequencies of an acoustic problem for a simply

connected region. for acoustic problem. A multiply connected region enclosed with cubic and spherical boundaries is also investigated.

3.2 Formulations

Let p be the pressure of the time-harmonic sound wave propagating in a domain $\Omega \subset \mathbb{R}^3$. Then p satisfies the Helmholtz equation:

$$\nabla^2 p(x) + k^2 p(x) + f(x) = 0 \qquad \text{in } \Omega, \tag{3.1}$$

where x is a point in Ω, $k = \omega/C$ is the wave number, and $f(x)$ is a source term.

The boundary conditions are written as

$$p(x) = \bar{p}(x) \qquad \text{on } S_p, \tag{3.2}$$

$$\frac{\partial p(x)}{\partial n(x)} = \mathrm{i}\rho\omega\bar{v}(x) \qquad \text{on } S_v, \tag{3.3}$$

$$p(x) = zv(x) \qquad \text{on } S_z, \tag{3.4}$$

where ρ, $v(x)$, and z denote the density of the medium, the normal component of the particle velocity and the acoustic impedance, respectively, i denotes the unit imaginary number and $n(x)$ denotes the outward normal direction at x to the boundary.

The fundamental solutions for the Helmholtz equation are given as

$$p^*(x, y) = \frac{1}{4} H_0^{(1)}(kr) \qquad \text{for } 2D, \tag{3.5}$$

$$p^*(x, y) = \frac{1}{4\pi r} e^{\mathrm{i}kr} \qquad \text{for } 3D, \tag{3.6}$$

where x and y are two different point in the domain and $r = |y - x|$, $H_0^{(1)}$ denotes the Hankel function of the first kind of order zero.

In this chapter, the derivation of the BEM formulations for 3D case is presented. In order to remove the spurious eigenvalues, Burton-Miller's method for 3D is employed, and the hypersingular integral resulting from the normal derivative is formulated explicitly.

The integral representation for $p(x)$ can be written as follows:

$$p(x) = \int_S p^*(x,y)\frac{\partial p(y)}{\partial n(y)}\,\mathrm{d}S_y - \int_S \frac{\partial p^*(x,y)}{\partial n(y)}p(y)\,\mathrm{d}S_y + \int_\Omega p^*(x,y)f(y)\,\mathrm{d}\Omega_y, \quad x \in \Omega. \tag{3.7}$$

Now the case in which the internal point x approaches a point on the boundary, is considered. Let the boundary be discretized into triangular constant elements and the boundary point which the internal point x approaches is assumed to be the center of geometry x of the triangle Δ_x. Since the fundamental solution and its derivative has singularities at $r = |x - y| = 0$, we attach a hemisphere domain Ω_ϵ of radius ϵ over x to circumvent $r = 0$ in evaluating the boundary integrals for the triangle Δ_x, as shown in Fig. 3.1 (b). Let also the boundary from which the circle is excluded be Γ_ϵ and the hemisphere boundary be S_ϵ. The boundary integral for Γ_ϵ and S_ϵ are evaluated separately. The integrals are defined as follows:

$$H_1 = \int_{S_\epsilon} p^*(x,y)\frac{\partial p(y)}{\partial n(y)}\,\mathrm{d}S_y, \tag{3.8}$$

$$H_2 = -\int_{S_\epsilon} \frac{\partial p^*(x,y)}{\partial n(y)}p(y)\,\mathrm{d}S_y, \tag{3.9}$$

$$I_1 = \int_{\Gamma_\epsilon} p^*(x,y)\frac{\partial p}{\partial n}(y)\,\mathrm{d}S_y, \tag{3.10}$$

$$I_2 = -\int_{\Gamma_\epsilon} \frac{\partial p^*(x,y)}{\partial n(y)}p(y)\,\mathrm{d}S_y. \tag{3.11}$$

Taking the limit $\epsilon \to 0$, above integrals are obtained as

$$\lim_{\epsilon\to 0} H_1 = 0, \tag{3.12}$$

$$\lim_{\epsilon\to 0} H_2 = \frac{1}{2}p(x), \tag{3.13}$$

$$\lim_{\epsilon\to 0} I_1 = \left[\frac{\mathrm{i}}{2k}\left(1 - \frac{1}{2\pi}\sum_{m=1}^{3}\int_{\theta_1^m}^{\theta_2^m} e^{\mathrm{i}k\bar{R}(\theta)}\mathrm{d}\theta\right)\right]\frac{\partial p}{\partial n}(x), \tag{3.14}$$

$$\lim_{\epsilon\to 0} I_2 = 0. \tag{3.15}$$

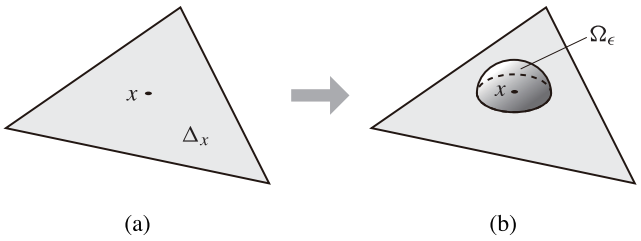

Figure 3.1: (a) A triangular element Δ_x on the boundary. (b) An infinitesimal hemisphere domain Ω_ϵ is attached to the neighborhood of x.

Finally, the conventional boundary integral equation (CBIE) is obtained as follows:

$$C(x)p(x) = \int\limits_{S\setminus\Delta_x} p^*(x,y)\frac{\partial p(y)}{\partial n(y)}\,\mathrm{d}S_y - \int\limits_{S\setminus\Delta_x} \frac{\partial p^*(x,y)}{\partial n(y)}p(y)\,\mathrm{d}S_y + \left[\frac{\mathrm{i}}{2k}\left(1 - \frac{1}{2\pi}\sum_{m=1}^{3}\int\limits_{\theta_1^m}^{\theta_2^m} e^{\mathrm{i}k\bar{R}(\theta)}\mathrm{d}\theta\right)\right]\frac{\partial p(x)}{\partial n(x)} + \int\limits_{\Omega} p^*(x,y)f(y)\,\mathrm{d}\Omega_y, \quad x \in S, \tag{3.16}$$

where $C(x) = 1/2$, if x is located at a smooth part of the boundary, the Cauchy principal-value integrals are evaluated explicitly and the variables for this evaluation are shown in Fig. 3.2.

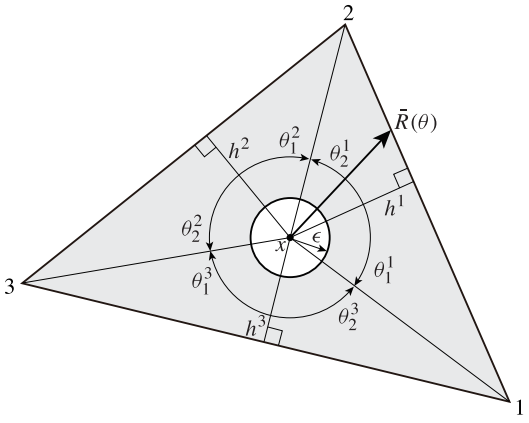

Figure 3.2: The variables used for evaluating the integrals for Γ_ϵ.

The normal derivative of the integral equation in a direction $n(x)$ defined at point x is written as

$$\frac{\partial p(x)}{\partial n(x)} = \int_S \hat{p}^*(x,y)\frac{\partial p(y)}{\partial n(y)}\,\mathrm{d}S_y - \int_S \frac{\partial \hat{p}^*(x,y)}{\partial n(y)} p(y)\,dS_y + \int_\Omega \hat{p}^*(x,y) f(y)\,\mathrm{d}\Omega_y, \quad x \in \Omega \tag{3.17}$$

where $\hat{(\ )} = \partial(\ )/\partial n(x)$, and

$$\begin{aligned} \hat{p}^*(x,y) &= \frac{\partial p^*(x,y)}{\partial n(x)} \\ &= \frac{-1}{4\pi r^2}(1 - \mathrm{i}kr)e^{\mathrm{i}kr}\frac{\partial r}{\partial n(x)}. \end{aligned} \tag{3.18}$$

The normal derivative $\partial r/\partial n(x)$ can be evaluated by using

$$\frac{\partial r}{\partial n(x)} = r_{,i} n_i(x). \tag{3.19}$$

where $r_{,i}$ and $n_i(x)$, $(i = 1, 2, 3)$ are the Cartesian components of gradients of r and the unit outward normal vector, respectively. Note that the Einstein's summation convention is applied for repeated indices.

The following integrals are defined as point x approaches a point on the boundary,

$$J_1 = \int_{S_\epsilon} \hat{p}^*(x,y)\frac{\partial p(y)}{\partial n(y)}\,\mathrm{d}S_y, \tag{3.20}$$

$$J_2 = -\int_{S_\epsilon} \frac{\partial \hat{p}^*(x,y)}{\partial n(y)} p(y)\,\mathrm{d}S_y, \tag{3.21}$$

$$K_1 = \int_{\Gamma_\epsilon} \hat{p}^*(x,y)\frac{\partial p(y)}{\partial n(y)}\,\mathrm{d}S_y, \tag{3.22}$$

$$K_2 = -\int_{\Gamma_\epsilon} \frac{\partial \hat{p}^*(x,y)}{\partial n(y)} p(y)\,\mathrm{d}S_y. \tag{3.23}$$

Taking the limit $\epsilon \to 0$, above integrals are evaluated as follows:

$$\lim_{\epsilon\to 0} J_1 = \frac{1}{6}\frac{\partial p(x)}{\partial n(x)} \tag{3.24}$$

$$J_2 = \frac{1}{2\epsilon}p(x) + \frac{1}{3}\frac{\partial p(x)}{\partial n(x)} + O(\epsilon^2), \tag{3.25}$$

$$\lim_{\epsilon\to 0} K_1 = 0, \tag{3.26}$$

$$K_2 = -\frac{1}{2\epsilon}p(x) - \frac{\mathrm{i}k}{2}p(x) + \left\{ \sum_{m=1}^{3} \int_{\theta_1^m}^{\theta_2^m} \frac{e^{\mathrm{i}k\bar{R}(\theta)}}{4\pi\bar{R}(\theta)} \mathrm{d}\theta \right\} p(x). \tag{3.27}$$

Substituting the above integrals into Eq. (3.17), the representation for normal directional derivative of the boundary integral equation (NDBIE) is obtained as

$$\begin{aligned} \frac{1}{2}\frac{\partial p(x)}{\partial n(x)} = & \int_{S\setminus\Delta_x} \hat{p}^*(x,y)\frac{\partial p(y)}{\partial n(y)}\,\mathrm{d}S_y - \int_{S\setminus\Delta_x} \frac{\partial \hat{p}^*(x,y)}{\partial n(y)} p(y)\,\mathrm{d}S_y \\ & - \frac{\mathrm{i}k}{2}p(x) + \left\{ \sum_{m=1}^{3} \int_{\theta_1^m}^{\theta_2^m} \frac{e^{\mathrm{i}k\bar{R}(\theta)}}{4\pi\bar{R}(\theta)} \mathrm{d}\theta \right\} p(x) + \int_{\Omega} \hat{p}^*(x,y) f(y)\,\mathrm{d}\Omega_y, \quad x \in S, \end{aligned} \tag{3.28}$$

in which all the Cauchy principal-value integrals are also evaluated explicitly.

To identify the spurious eigenvalues, Burton-Miller's method [55] provides the formulation that requires the combination of CBIE (3.16) and NDBIE (3.28) by multiplying a coefficient μ:

$$\mathrm{CBIE} + \mu\mathrm{NDBIE}, \tag{3.29}$$

where μ is typically set as $\mu = \mathrm{i}/k$.

For free vibrations, the source term $f(y) = 0$. Discretizing the boundary integral equation in Eq. (4.5) with Ne constant triangular elements and considering the point x of the fundamental solution at the center of geometry of each triangular element, the following Ne algebraic equations can be obtained:

$$\mathbf{Bp} = \mathbf{Gq}, \tag{3.30}$$

where $\mathbf{B}$ and $\mathbf{G}$ are two $Ne \times Ne$ matrices, and $\mathbf{p} = \{p\}$ and $\mathbf{q} = \{\frac{\partial p}{\partial n}\}$ are vectors of Ne components. Furthermore, substituting the homogenous boundary condition and rearranging the unknowns to the left-hand side, a nonlinear eigenvalue problem is obtained as follows:

$$\mathbf{A}(k)\mathbf{x} = \mathbf{0}. \tag{3.31}$$

If there is nontrivial solution to Eq. (3.31), the following relation must hold:

$$\mathsf{det}[\mathbf{A}(k)] = 0. \tag{3.32}$$

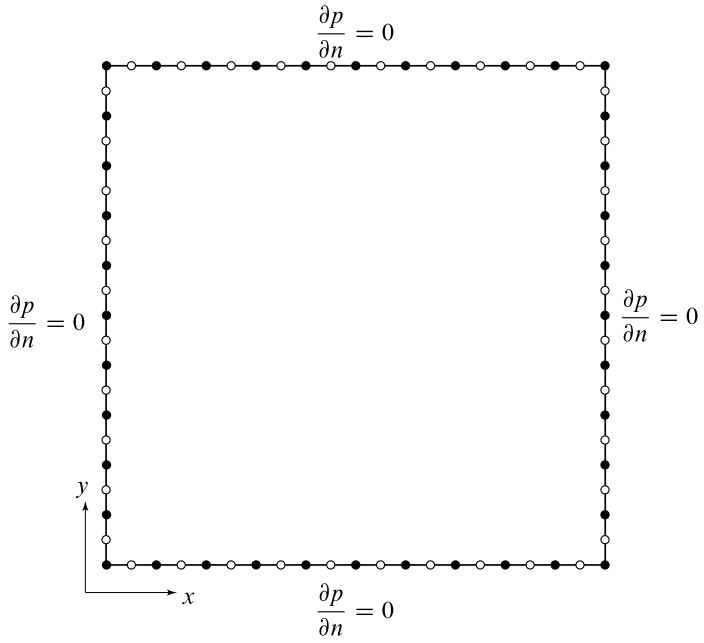

Figure 3.3: A square structure.

The algebraic equations in Eq. (3.31) finally leads to a nonlinear eigenvalue problem in which the eigenvalue parameter k is involved implicitly in the elements of matrix $\mathbf{A}$. The eigenvalues are the roots of $\mathsf{det}[\mathbf{A}(k)] = 0$. Eq. (3.32) is a highly nonlinear transcendental equation for k, hence it is very difficult to solve analytically. In order to solve the nonlinear eigenvalue problem in Eq. (3.31), the block SS method is employed as an eigensolver.

3.3 Numerical examples

3.3.1 2D acoustic cavity

Consider a simple 2D square structure with the edges of 1[m] as shown in Fig. 3.3. Neumann boundary conditions are given on all the edges.

The theoretical solution for the eigenvalues is

$$k^* = \pi\sqrt{(\frac{t_1}{L_1})^2 + (\frac{t_2}{L_2})^2} \quad (t_1 = 0, 1, \cdots, t_2 = 0, 1, \cdots) \tag{3.33}$$

for this square model $L_1 = L_1 = 1$ and the closed form of the eigenmode is

$$p_e = A\cos(t_1\pi x_1)\cos(t_2\pi x_2). \tag{3.34}$$

The boundary is discretized into 40 quadratic isoparametric elements. The circular integration path $\Gamma = \gamma + \rho e^{i\theta}$, $\gamma = (7.5, 0)$, $\rho = 5.5$ is used and the parameters $K = 4$ and $l = 10$. Fig. 3.4 shows that the normalized singular values σ_i/σ_{max}, $(i = 1, 2, ..., Kl)$ are greater than 10^{-12}. In this case, to filter out the meaningful singular values, usually one can increase either of l or N until the normalized singular values less than 10^{-12} emerge, if the fixed threshold values $\delta = 10^{-12}$ is given [1]. However, it can be found that there is a step change of the normalized singular values at $10^{-5} \sim 10^{-7}$ in Fig. 3.4.

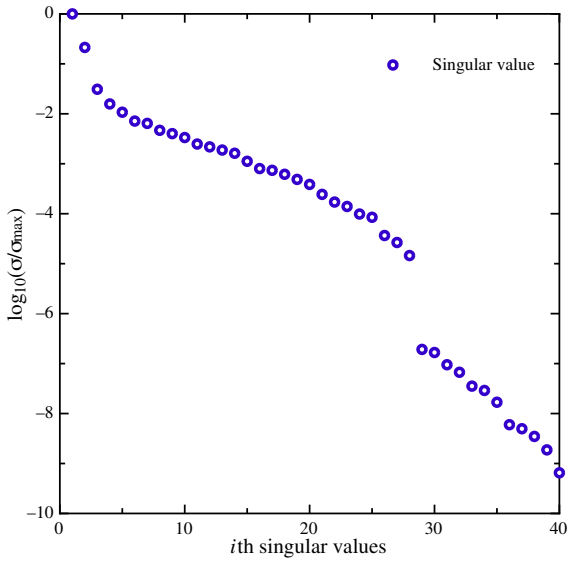

Figure 3.4: The singular values for fixed parameter $k = 4$ and $l = 10$.

The behavior of the singular values versus N is shown in Fig. 3.5. It can be found that a separation of the singular values emerges and for $N > 100$, singular values are well-separated. The open triangles represent the meaningful singular values and the open circles represent the separated small singular values. If the threshold value δ is chosen in the separation range $10^{-5} \sim 10^{-7}$ to filter the normalized singular values σ_i/σ_{max}, the small singular values can be cut off. With the imaginary tolerance threshold value set as 0.05, the result with $N = 128$ and other parameters same as in the previous computation is shown in Table 3.1. Eighteen real eigenvalues are obtained by the block SS method in reasonable accuracy. Fig. 3.6 shows the integration path, the open circles and the location of the eigenvalues represented by the rhombuses.

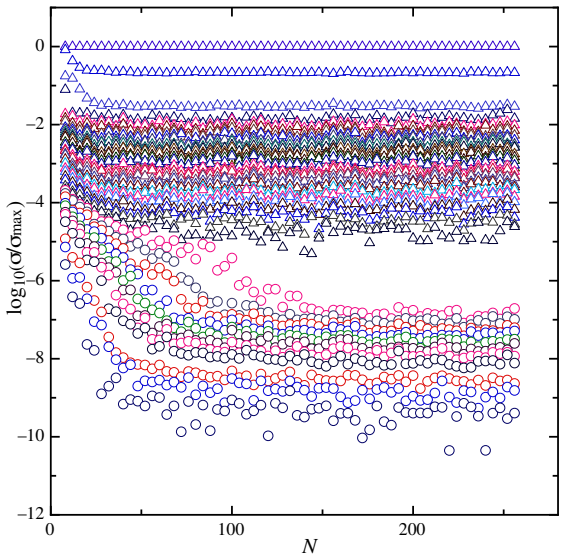

Figure 3.5: The separation of singular values.

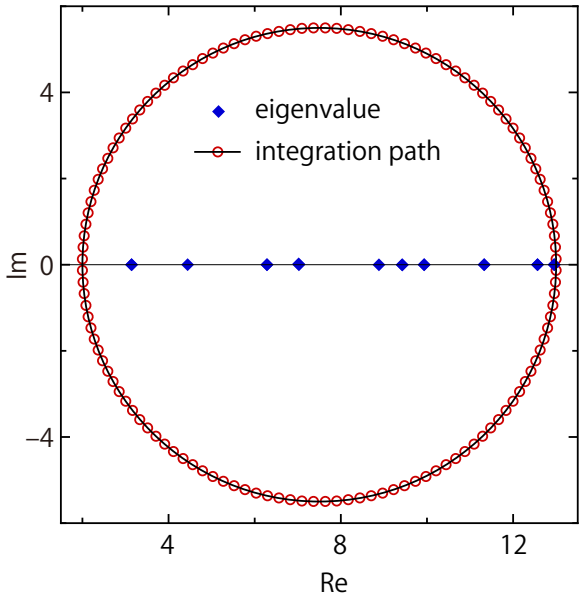

Figure 3.6: The integration path and obtained eigenvalues.

The eigenmodes of the interior domain can be computed by using the eigenpairs obtained by the block SS method. The sound pressure amplitudes of the internal points are solved by substituting the eigenvalues and eigenvectors into integral equation. The eigenmodes corresponding to the simple eigenvalues $\sqrt{2}\pi$ and $2\sqrt{2}\pi$ are shown in Fig. 3.7 and Fig. 3.8, respectively.

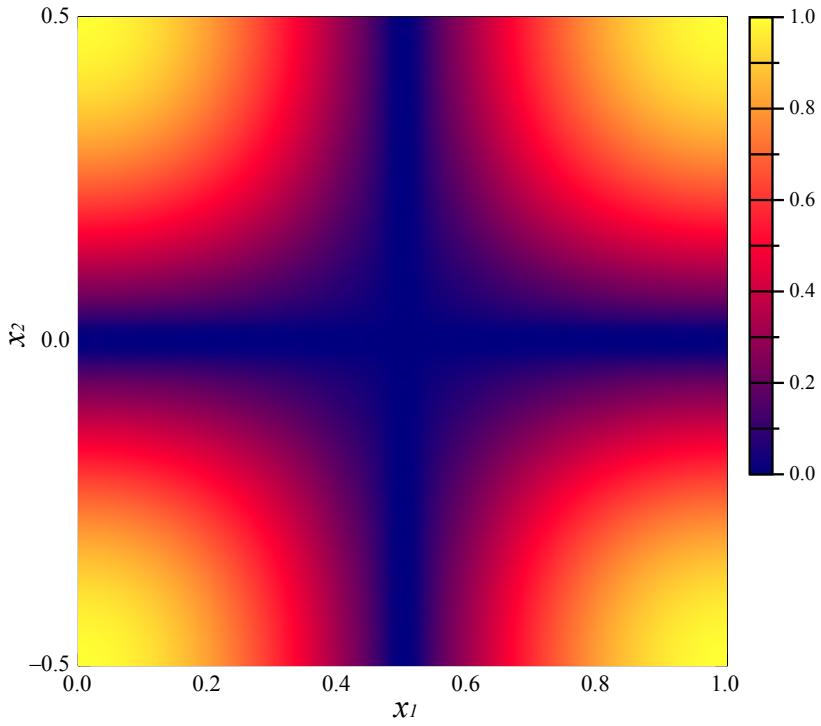

Figure 3.7: The eigenmode corresponding to $\sqrt{2}\pi$

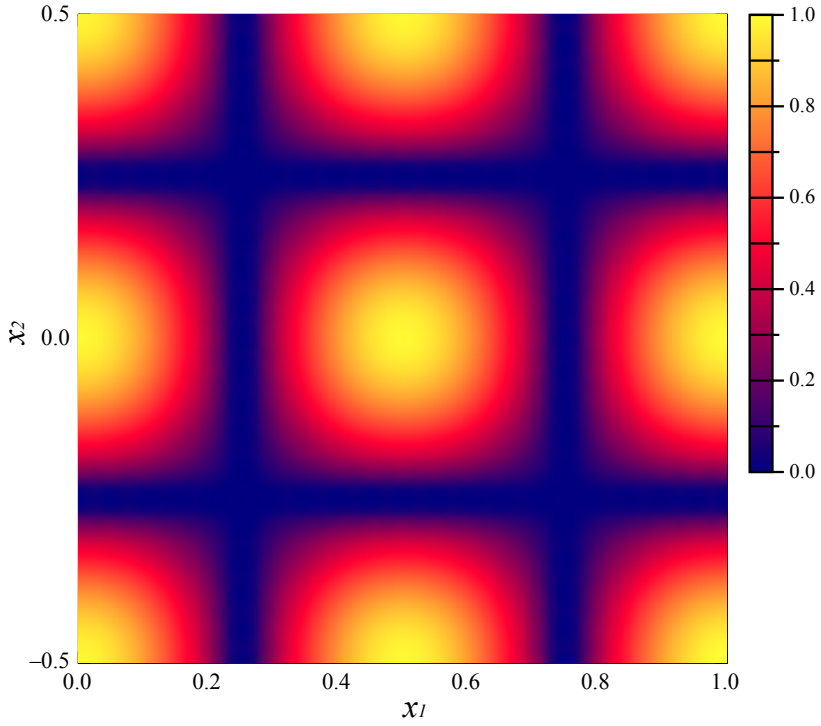

Figure 3.8: The eigenmode corresponding to $2\sqrt{2}\pi$

Table 3.1: Numerical results of the eigenvalues and the relative error

i	t_1	t_2	k_i	$\lvert\frac{k_i^*-\mathrm{Re}[k_i]}{k_i^*}\rvert \times 100$ [%]
1	1	0	$3.1415 - 2.7247 \times 10^{-4}i$	0.002930
2	0	1	$3.1419 + 2.0373 \times 10^{-4}i$	0.009471
3	1	1	$4.4428 + 5.7581 \times 10^{-4}i$	0.002261
4	2	0	$6.2832 + 1.3439 \times 10^{-5}i$	0.0009452
5	0	2	$6.2877 + 3.4249 \times 10^{-4}i$	0.07165
6	2	1	$7.0205 + 1.8360 \times 10^{-3}i$	0.06077
7	1	2	$7.0270 - 1.3931 \times 10^{-3}i$	0.03083
8	2	2	$8.8845 - 2.4201 \times 10^{-3}i$	0.01474
9	3	0	$9.4230 - 8.9682 \times 10^{-4}i$	0.01939
10	0	3	$9.4280 - 5.5301 \times 10^{-3}i$	0.03422
11	3	1	$9.9335 - 1.9236 \times 10^{-3}i$	0.01098
12	1	3	$9.9352 + 1.2624 \times 10^{-4}i$	0.006404
13	2	3	$11.3273 + 7.9114 \times 10^{-4}i$	0.0009067
14	3	2	$11.3287 - 1.5518 \times 10^{-4}i$	0.01388
15	0	4	$12.5667 + 6.3867 \times 10^{-4}i$	0.002423
16	4	0	$12.5669 + 3.1598 \times 10^{-4}i$	0.004116
17	1	4	$12.9537 + 8.2268 \times 10^{-4}i$	0.004252
18	4	1	$12.9539 + 6.1463 \times 10^{-4}i$	0.006124

3.3.2 3D acoustic cavities

For 3D case, three numerical models are presented: a spherical model with Dirichlet boundary condition, a cubic box with mixed boundary condition, both of which have the analytical solutions, and a doubly connected region consisting of cubic boundary and spherical boundary. For the cubic box model, the eigenmodes corresponding to the nondegenerate eigenvalues are presented, and for the third model, the spurious eigenvalues resulting from the spherical boundary are discussed.

In all the examples, the standard boundary element method and constant triangular elements are adopted.

3.3.2.1 Eigenvalues of interior acoustic problem of a spherical model with Dirichlet boundary condition

In Fig. 3.9(a), an internal field of a unit spherical structure with radius $R = 1$ [m] is considered. The acoustic medium is assumed to be air with the sound speed $c = 340$ [m/s]. The Dirichlet boundary condition is given on the surface of the sphere. The general solution of Helmholtz' equation, regular at the origin, is given as

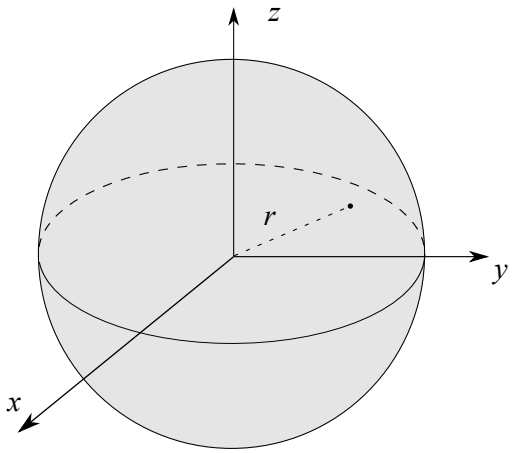

(a) Spherical field model.

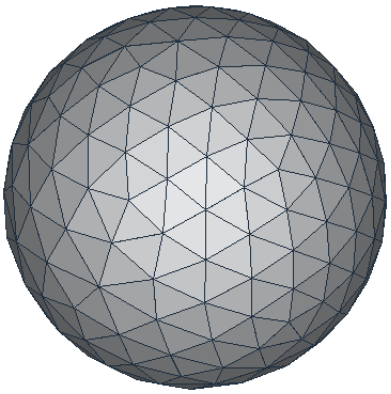

(b) Meshed model of the spherical field.

Figure 3.9: Spherical field model with 490 elements.

$$p_e(r,\theta,\varphi) = \sum_{\alpha=0}^{\infty} \sum_{\beta=-\alpha}^{\alpha} C_{\alpha\beta} j_\alpha(kr) Y_\alpha^\beta(\theta,\varphi), \tag{3.35}$$

where $k = \frac{2\pi f}{C}$ is the wave number, $C_{\alpha\beta}$ are the Fourier coefficients determined by the boundary conditions, and j_α denotes the spherical Bessel function of integer order α. Also, $Y_\alpha^\beta = C_p P_\alpha^\beta(\cos\theta) e^{i\beta\varphi}$, where $P_\alpha^\beta(\cos\theta)$ are associated Legendre polynomials, and C_p is a constant.

Obviously, the eigenvalues for k are zeros of $j_\alpha(kR)$ for the Dirichlet boundary condition. Due to the spherical Bessel function with order α and β varying from $-\alpha$ to α, we have the multiplicity of the eigenvalues corresponding to the zero points of the spherical Bessel functions. The multiplicity of the eigenvalues now becomes $2\alpha+1$. The first three zero points of the spherical Bessel functions of 0th to 5th order and their multiplicities are shown in Table 3.2.

Table 3.2: The multiplicity of the Dirichlet eigenvalues.

α	zeros points of j_α	multiplicity
0	3.14159, 6.28319, 9.42478	1
1	4.49340, 7.72525, 10.90412	3
2	5.76346, 9.09501, 12.32294	5
3	6.98793, 10.41711, 13.69802	7
4	8.18256, 11.70491, 15.03966	9
5	9.35581, 12.96653, 16.35471	11

As shown in Fig. 3.9, the boundary of the spherical field is divided into 490

triangular elements, hence the DOF of the system becomes $Ne = 490$. By taking as $\Gamma = \gamma + \rho e^{i\theta}$, $\gamma = (6, 0)$, $\rho = 2.6$ for the integration path, we obtain six different eigenvalues located in the domain as k^*=4.49340, 5.76346, 6.28319, 6.98793, 7.72525, 8.18256, with the parameter set $N = 256$, $K = 4$, $l = 15$, and $\delta = 10^{-12}$. Both the obtained simple and multiple eigenvalues are shown in Table 3.3. It is found that the multiplicities of the eigenvalues smaller than l are kept.

Fig. 3.10 shows that the eigenvalue k_1 approximating to $k^* = 3.14159$, lying outside the periphery of the domain, may also be obtained, and can be sorted from the results lying in the given domain. This is because the extension of the implicit filter function, and the situation can be improved by increasing the number of the points used for trapezoidal rule (we do not plot complex results here as the complex eigenvalues are not discussed in this thesis). Fig. 3.12 shows that the eigenvalues located on the periphery of the integration path will disappear as the filter function is approximated more accurately, however, the accuracy of the numerical results will not be improved.

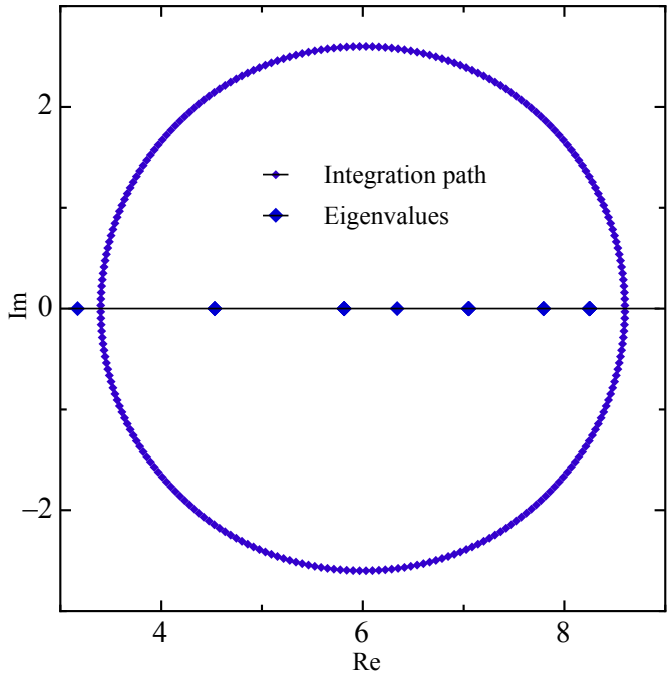

Figure 3.10: Eigenvalues of spherical model with $N = 256$.

Observing the behavior of the normalized singular values in Fig. 3.11, it is found that the singular values can be divided into three groups: (i) Becoming stable soon from the beginning (circular symbols); (ii) Decaying relatively slowly (triangular sym-

Table 3.3: The Dirichlet eigenvalues of spherical model.

i	k_i	$\lvert\frac{k_i^*-\mathrm{Re}[k_i]}{k_i^*}\rvert \times 100$ [%]
1	$3.1703 - 7.4529 \times 10^{-6}i$	0.9145
2	$4.5330 + 3.0384 \times 10^{-5}i$	0.8803
3	$4.5352 + 3.4117 \times 10^{-5}i$	0.9295
4	$4.5343 + 3.2560 \times 10^{-5}i$	0.9107
5	$6.3407 + 6.6061 \times 10^{-5}i$	0.9152
6	$5.8175 + 5.5999 \times 10^{-5}i$	0.9374
7	$5.8153 + 5.1600 \times 10^{-5}i$	0.9000
8	$5.8140 + 4.8672 \times 10^{-5}i$	0.8766
9	$5.8135 + 4.7898 \times 10^{-5}i$	0.8686
10	$5.8131 + 4.7072 \times 10^{-5}i$	0.8610
11	$7.7932 + 9.3120 \times 10^{-5}i$	0.8796
12	$7.7970 + 1.0455 \times 10^{-5}i$	0.9288
13	$7.7956 + 9.9935 \times 10^{-5}i$	0.9101
14	$7.0507 + 6.8848 \times 10^{-5}i$	0.8977
15	$7.0497 + 6.7057 \times 10^{-5}i$	0.8838
16	$7.0489 + 6.5255 \times 10^{-5}i$	0.8723
17	$7.0483 + 6.3485 \times 10^{-5}i$	0.8641
18	$7.0470 + 6.0589 \times 10^{-5}i$	0.8449
19	$7.0461 + 5.9277 \times 10^{-5}i$	0.8327
20	$7.0459 + 5.9148 \times 10^{-5}i$	0.8301
21	$8.2471 + 4.9937 \times 10^{-5}i$	0.7882
22	$8.2475 + 4.9487 \times 10^{-5}i$	0.7932
23	$8.2526 + 5.3112 \times 10^{-5}i$	0.8560
24	$8.2520 + 6.1446 \times 10^{-5}i$	0.8481
25	$8.2488 + 5.3377 \times 10^{-5}i$	0.8096
26	$8.2491 + 5.2274 \times 10^{-5}i$	0.8130
27	$8.2506 + 4.9398 \times 10^{-5}i$	0.8319
28	$8.2501 + 5.4687 \times 10^{-5}i$	0.8255
29	$8.2502 + 5.0740 \times 10^{-5}i$	0.8269

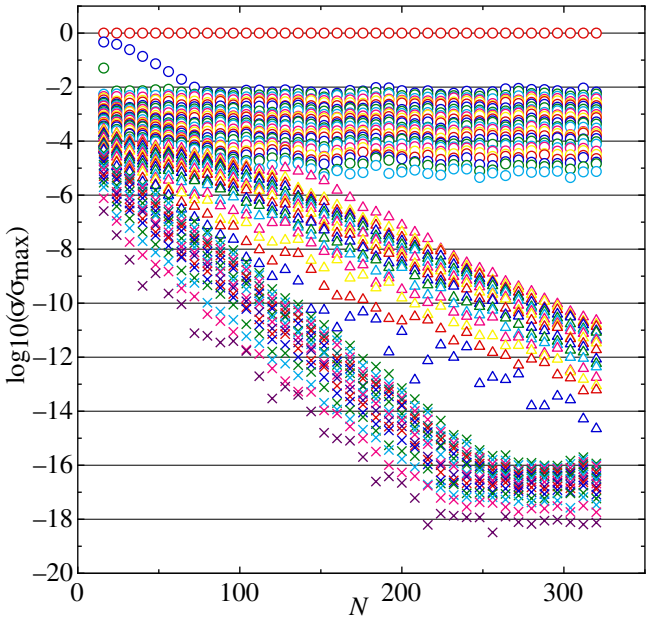

Figure 3.11: Separation of singular values of spherical model.

bols); (iii) Decaying fastest until they become somewhat stable. Group (ii) decays slowly because the corresponding eigenvalues (including some complex eigenvalues that are also spurious eigenvalues) are located near the periphery of the integration path.

Above behaviors of the singular values stem from the numerical evaluation of the contour integral, the BEM model, and also the distribution of eigenvalues.

According to Eq. (2.46), the error of the contour integral depends on N and the integrand, while the error of the eigenvalues obtained by the block SS method is related to the constants $\bar{C}$ (it is introduced in Eq. (2.46)) and N. $\bar{C}$ is independent of N in the case of a circular integration path. Therefore, when there are eigenvalues located near the periphery of integration path, $R_{\pm}$ tend to be 1. Therefore, N may not be a main factor to the accuracy of numerical results. For a certain model, it is more efficient to use small number for N as each point for trapezoidal rule costs one BEM calculation. Under the promise of a reasonable accuracy, N should be chosen as small as possible. There are two gaps formed by group (i) and group (ii), group (ii) and group (iii). If the threshold is chosen located in the first gap, only the eigenvalues located inside the integration path are obtained. However, with the threshold located in the latter gap, the eigenvalues located outside of the neighborhood of the integration path may be obtained. In both cases, the results are in reasonable accuracy.

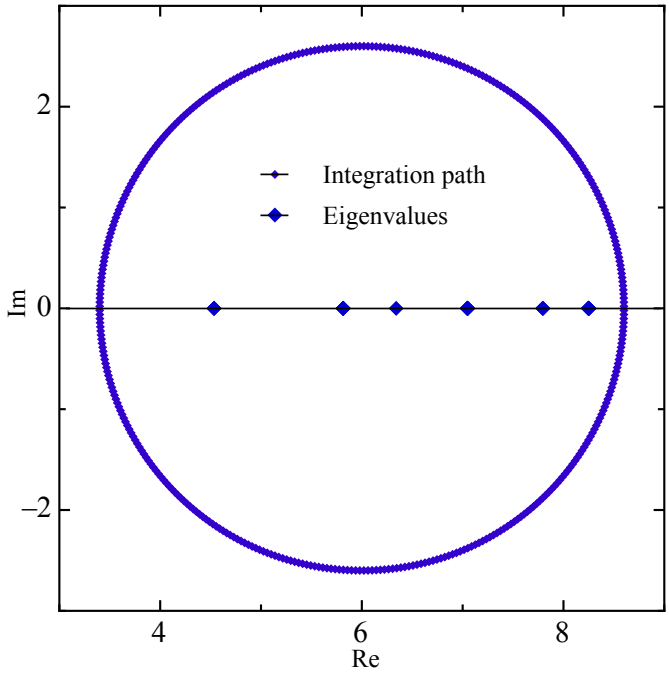

Figure 3.12: Eigenvalues of spherical model with N increased.

However, if a threshold located out of the gaps is used ghost results may be obtained, and they can be considered as eigenvalues located out of the domain, but they are not accurate.

It is found that the errors in the BEM are rather large comparing with those of the nonlinear eigenvalue problem example in [1]. The phenomenon is attributed to the discretization of the boundary of the BEM model. The next example shows that the method works well for a mixed boundary condition, furthermore, the eigenvectors are obtained and the accuracy may be improved by increasing the number of the meshes of the BEM model.

3.3.2.2 Cubic model with mixed boundary condition

Another example is a cubic box with edge length $L = 1$ [m], as depicted in Fig. 3.13(a), with the same acoustic medium with the previous model, the Dirichlet boundary condition is given on its left and right surfaces, while Neumann boundary condition is given on the other four surfaces that are considered as rigid wall. In this case the eigenvalues for the wave number k are given in the form [76]:

$$\pi\sqrt{n_1^2 + n_2^2 + n_3^2}, \tag{3.36}$$

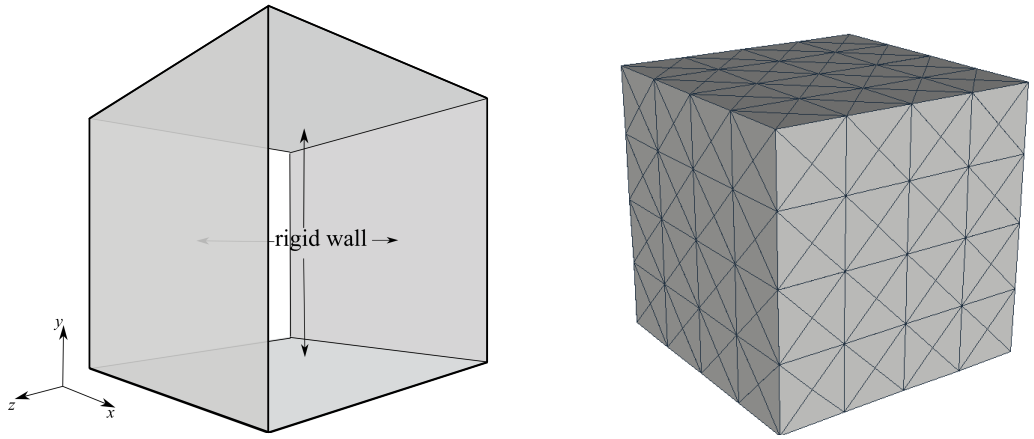

(a) Cubic box model. (b) Meshed model of cubic box.

Figure 3.13: Cubic model with 384 elements.

and the eigenmode is given as

$$p_e(x, y, z) = \sin(n_1\pi x)\cos(n_2\pi y)\cos(n_3\pi z), \tag{3.37}$$

where $n_1 = 1, 2, 3, \cdots$, $n_2 = 0, 1, 2, 3, \cdots$, and $n_3 = 0, 1, 2, 3, \cdots$. Degenerate eigenvalues also exist because of the cubic structure. Noticing that $n_1 \neq 0$, the analytical solutions are given in Table 3.4.

Table 3.4: Multiplicity of eigenvalues.

$\sqrt{n_1^2 + n_2^2 + n_3^2}$	k^*	multiplicity
1	3.14159	1
$\sqrt{2}$	4.44288	2
$\sqrt{3}$	5.44140	1
2	6.28319	1
$\sqrt{5}$	7.02481	4
$\sqrt{6}$	7.69530	3

As shown in Fig. 3.13(b), the surface of the cubic box is divided into 384 triangular constant elements. By taking as $\Gamma = \gamma + \rho e^{\mathrm{i}\theta}$, $\gamma = (5.5, 0)$, and $\rho = 2.4$ to define the integration path, six eigenvalues located in the domain are obtained: k^*=3.14159, 4.44288, 5.44140, 6.28319, 7.02481, and 7.69530, with the parameters set $N = 256$, $K = 4$, $l = 15$, and $\delta = 10^{-12}$. The four-point Gausian quadrature rule is also used for the evaluation of the contour integral, and the integral interval is divided into 64 segments. The total number of BEM analyses is $64 \times 4 = 256$ and the same

results are obtained with the same computation cost as that of trapezoidal rule. The numerical results and relative errors are given in Table 3.5. Both in the previous

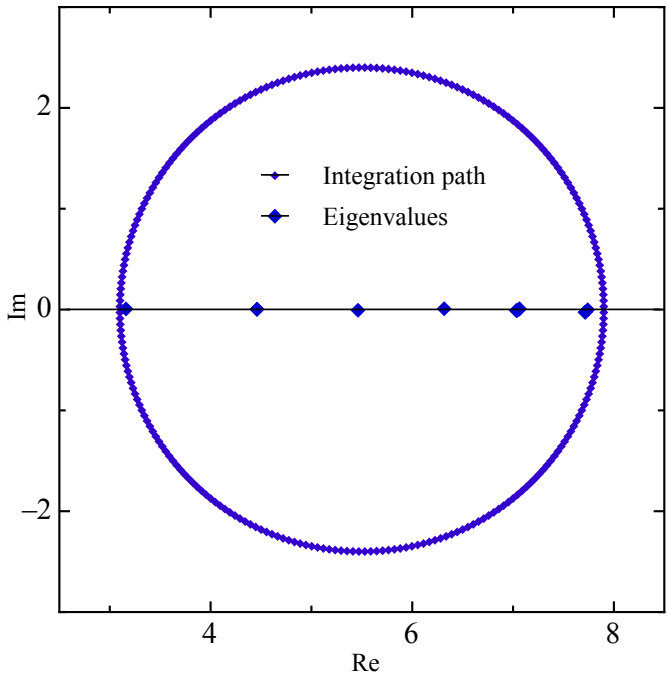

Figure 3.14: Eigenvalues of cubic model with mixed boundary condition.

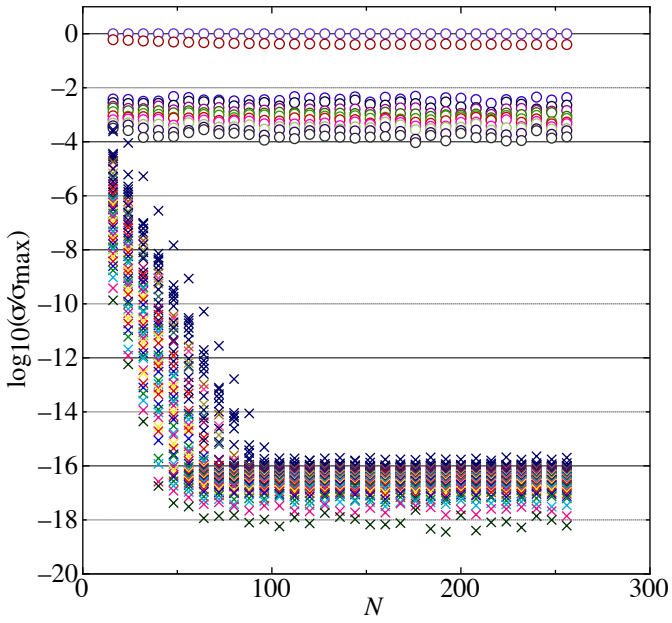

Figure 3.15: Separation of singular values of cubic model.

Table 3.5: The mixed boundary eigenvalues of cubic model.

i	k_i	$\lvert\frac{k_i^*-\mathrm{Re}[k_i]}{k_i^*}\rvert \times 100$ [%]
1	$3.1609 + 5.8744 \times 10^{-3}i$	0.6154
2	$5.4619 - 7.1328 \times 10^{-3}i$	0.3767
3	$6.3164 - 8.1983 \times 10^{-3}i$	0.5289
4	$7.7401 - 1.7383 \times 10^{-3}i$	0.5817
5	$7.7152 - 2.6113 \times 10^{-2}i$	0.2583
6	$7.7152 - 2.6113 \times 10^{-2}i$	0.2583
7	$7.0406 - 9.0043 \times 10^{-3}i$	0.2243
8	$7.0624 + 6.0769 \times 10^{-3}i$	0.5347
9	$7.0624 + 6.0769 \times 10^{-3}i$	0.5347
10	$7.0319 - 9.7160 \times 10^{-3}i$	0.1002
11	$4.4601 + 2.5835 \times 10^{-3}i$	0.3878
12	$4.4601 + 2.5835 \times 10^{-3}i$	0.3878

and this examples, we used the same threshold $\delta = 10^{-12}$ to filter out the small singular values of the Hankel matrix $\mathbf{H}_{Kl}$. This threshold is so small that it can be considered as a conservative choice. Because we choose the parameters such as l and K to make as there is no rank deficiency for the reduced eigenspace, there are always small singular values or we can increase l and K. In Fig. 3.15, we find that the small singular values decay rapidly while N increases, and the gap between the remaining singular values and the small singular values become sufficiently large at $N = 50$, and becomes stable at $N = 100$. Different from the previous example, there is no eigenvalue located outside the neighborhood of integration path, thus it can be found that there are only two groups of singular values.

The eigenmodes corresponding to the non-degenerated eigenvalues can be calculated by using Eq. (2.43), in which $\mathbf{S}$ may be formed using intermediate data $\mathbf{S}_j$. A τ-multiplicity eigenvalue is, however, corresponding to τ independent eigenvectors, so that the basis is not unique for this case. Fig. 3.16 shows the eigenmodes corresponding to the non-degenerate eigenvalues.

The numbers of boundary elements used for analyzing the cubic model are 384, 864, 1536, 2400, and 3456. The same parameter values as those used in the previous examples are used for the block SS method. It is found that the accuracy is improved effectively by increasing the number of boundary elements of the model, but increase in the number of points for trapezoidal rule does not change the accuracy much when a threshold located in the separation area of singular values is chosen. The convergence behavior of the relative error of the eigenvalues is shown in Fig. 3.17.

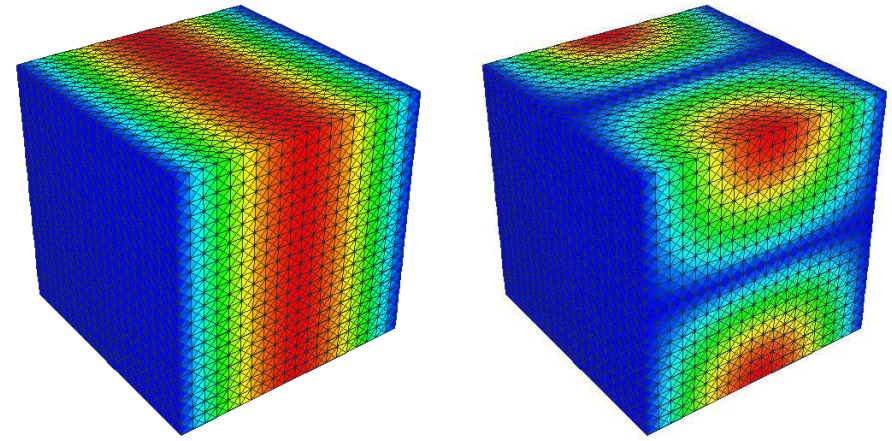

(a) $k = 3.16093$.

(b) $k = 5.46190$.

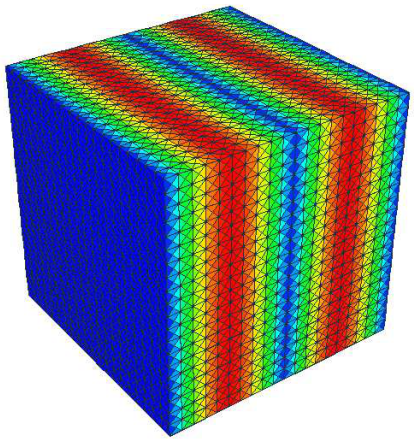

(c) $k = 6.31642$.

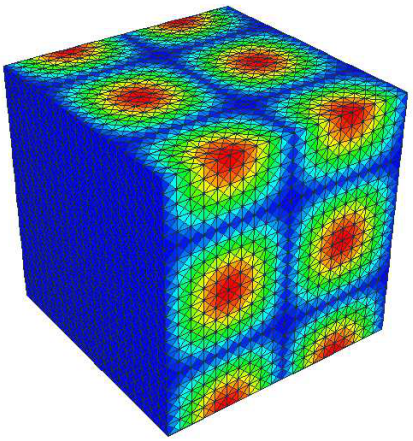

(d) $k = 10.90076$.

Figure 3.16: Eigenmodes of the cubic cavity.

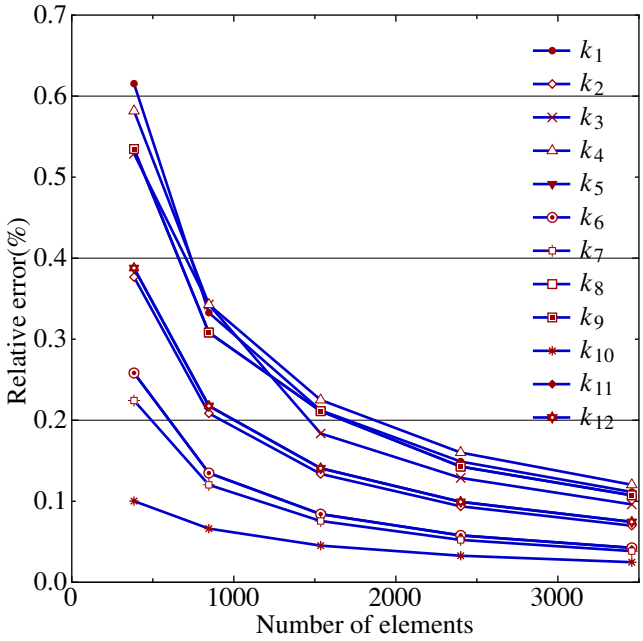

Figure 3.17: The relative error corresponding to the different number of elements of cubic model.

3.3.2.3 Multiply connected domain with cubic and spherical boundary

Another example is shown in Fig. 3.18(a), in which a multiply connected domain enclosed with a cubic with edge length $L_c = 1$[m] and spherical boundary S_s with radius $r_c = 0.4$[m] is considered. Neumann boundary condition is given on all the boundaries of the model. This example is given to demonstrate that the proposed methodology gives spurious eigenvalues resulting from the spherical boundary. Although it is an interior problem, the problem is regarded, for the spherical boundary S_s, as an exterior problem with Neumann boundary condition by the block SS method. Therefore, the spurious eigenvalues, which are given by corresponding interior problem with Dirichlet boundary condition, are also obtained. The elimination of the spurious eigenvalues resulted by the BEM for multiply-connected domain has been investigated by previous research [54, 77, 78, 79], wherein the real spurious eigenvalues are removed from the real axis. However, what is actually done by the Burton-Miller method is that a large imaginary part is given to the spurious eigenvalue and thus the spurious eigenvalue is removed from the real axis. The block SS method calculate all the eigenvalues within the contour in the complex plane, therefore, the removed real spurious eigenvalues may appear as complex values within this contour.

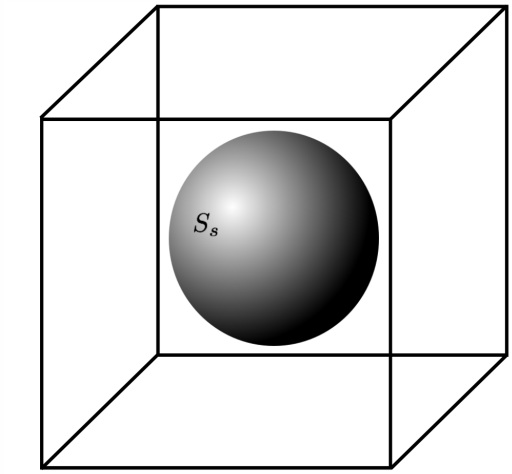

(a) Doubly connected region.

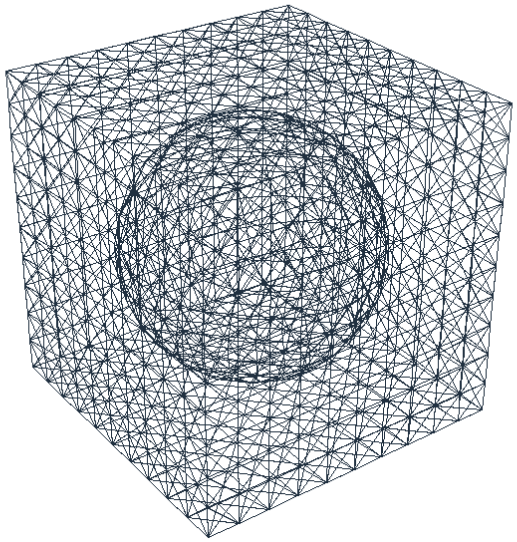

(b) Meshed model of doubly connected region.

Figure 3.18: Structure of doubly connected region with cubic and spherical boundary and its meshed model.

Table 3.6: The eigenvalues of the the multiply connected domain.

i	k_i	i	k_i
1	$6.4841 + 4.2477 \times 10^{-3}i$	20	$9.9249 + 1.2185 \times 10^{-2}i$
2	$6.4847 + 4.2491 \times 10^{-3}i$	21	$9.9257 + 1.2188 \times 10^{-2}i$
3	$6.4852 + 4.2494 \times 10^{-3}i$	22	$9.9268 + 1.2195 \times 10^{-2}i$
4	$6.9832 + 5.3121 \times 10^{-3}i$	23	$10.050 + 1.1011 \times 10^{-2}i$
5	$6.9843 + 5.3178 \times 10^{-3}i$	24	$10.051 + 1.1018 \times 10^{-2}i$
6	$6.9860 + 5.3255 \times 10^{-3}i$	25	$10.053 + 1.1035 \times 10^{-2}i$
7	$7.4343 + 7.2119 \times 10^{-3}i$	26	$10.165 + 1.1043 \times 10^{-2}i$
8	$7.4345 + 7.2137 \times 10^{-3}i$	27	$10.165 + 1.1047 \times 10^{-2}i$
9	$7.4347 + 7.2155 \times 10^{-3}i$	28	$10.238 + 1.1373 \times 10^{-2}i$
10	$7.5648 + 8.9061 \times 10^{-3}i$	29	$10.413 + 1.7243 \times 10^{-2}i$
11	$7.9366 - 5.7301 \times 10^{-5}i^*$	30	$10.921 + 1.3084 \times 10^{-2}i$
12	$8.5184 + 8.9087 \times 10^{-3}i$	31	$10.922 + 1.3084 \times 10^{-2}i$
13	$8.5203 + 8.9195 \times 10^{-3}i$	32	$10.922 + 1.3089 \times 10^{-2}i$
14	$8.9685 + 9.8402 \times 10^{-3}i$	33	$11.348 + 3.1952 \times 10^{-5}i^*$
15	$8.9687 + 9.8319 \times 10^{-3}i$	34	$11.354 + 1.9501 \times 10^{-5}i^*$
16	$8.9701 + 9.8340 \times 10^{-3}i$	35	$11.361 + 1.0512 \times 10^{-5}i^*$
17	$9.3733 + 6.5595 \times 10^{-3}i$	36	$11.417 + 1.7828 \times 10^{-2}i$
18	$9.3735 + 6.5617 \times 10^{-3}i$	37	$11.417 + 1.7835 \times 10^{-2}i$
19	$9.3743 + 6.5659 \times 10^{-3}i$	38	$11.417 + 1.7840 \times 10^{-2}i$

* Spurious eigenvalues corresponding to the boundary S_s.

Table 3.7: The modified spurious eigenvalues obtained by Burton-Miller's method.

i	$\tilde{k}_i$
11	$9.4506 - 2.6060i$
33	$12.7665 - 3.0248i$
34	$12.7919 - 3.0088i$
35	$12.7783 - 3.0165i$

The spurious eigenvalues and their multiplicities shown in Table 3.6 are in conformity with the corresponding interior problem's analytical solution that is determined by Eq. (3.35). Among these spurious eigenvalues, $(7.9366, -5.7301 \times 10^{-5})$ corresponds

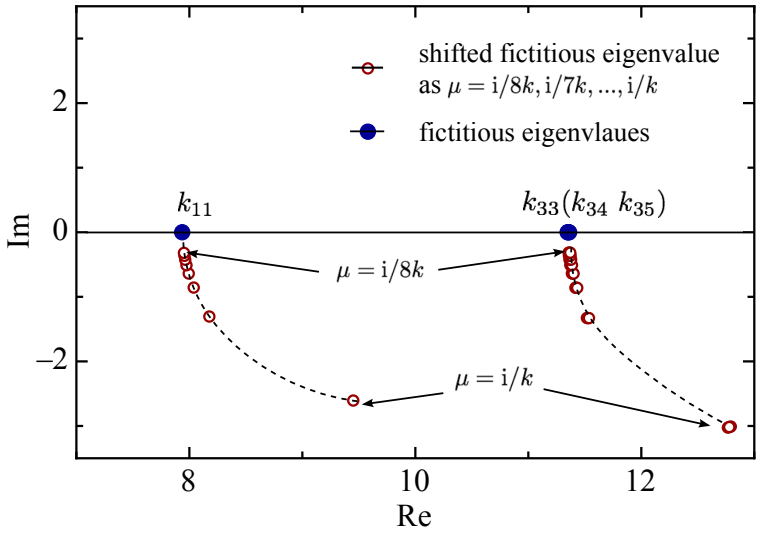

Figure 3.19: The shift of spurious eigenvalues (the dashed lines denote the shift tracks).

to the first zero point of j_0, whose multiplicity is 1, and $(11.354, 1.95006 \times 10^{-5}i)$ corresponds to the first zero point of j_1 whose multiplicity is 3. In Fig. 3.19, the shift of the spurious eigenvalues is shown as the parameter μ changes as i/8k,i/7k,...,i/k, and it is found that larger μ gives larger imaginary parts for the spurious eigenvalues. Most interestingly, from the Fig. 3.20, it can be seen that the eigenmode corresponding to the spurious eigenvalue $k = 7.9366$ is very similar to the eigenmode corresponding to $k = 7.5648$, since the real spurious eigenvalue 7.9366 is similar to 7.5648, and waves with similar wave lengths and wave numbers propagate in the structure. So, the eigenmodes shown in Fig. 3.20 also have difference in the distribution of the amplitude of the sound pressure.

It seems very difficult to distinguish the spurious eigenvalues from the numerical results if the analytical solution of the problem is not known in advance. However, as we show in Table 3.7 the modified spurious eigenvalues corresponding to the eigenvalues for number 11, 33, 34, and 35 shown in Table 3.6, it can be seen that large imaginary components are added to the spurious eigenvalues by using Burton-Miller's method. This means that Burton-Miller's method can shift the spurious eigenvalues to complex numbers. Therefore, these spurious results can be filtered out very easily by checking the imaginary parts. Comparing the results in Table 3.6 and Table 3.7, it is found that the added number should not be constant but depend on the eigenvalue and the parameter μ.

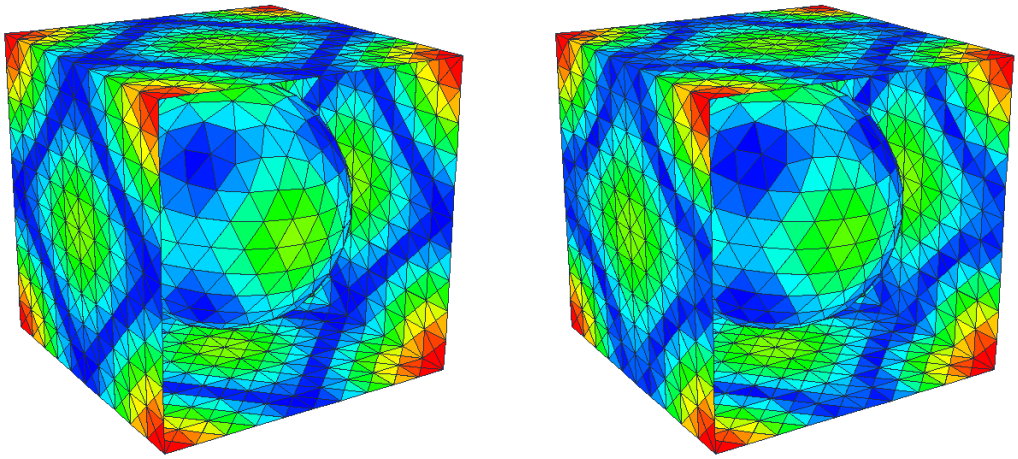

(a) $k = 7.5648$. (b) $k = 7.9366$ (spurious eigenvalues).

Figure 3.20: Eigenmodes of the cubic cavity with rigid spherical inclusion.

3.4 Conclusion

In this chapter the BEM combined with the block SS method is applied to the calculation of eigenfrequencies of 2D/3D acoustic cavities. With this methodology, we can extract the accurate eigenvalues lying in a given domain in the complex plane of wave number by solving a generalized eigenvalue problem by means of numerical contour integration, by which we can convert the original eigenspace to a relatively small one under concern.

For the 2D acoustic cavity, a relatively large threshold $\delta = 10^{-6}$ is chosen for the rank detection of the Hankel matrices. Also for the 3D cases, by observing the behavior of the singular values, a relatively larger threshold value can be determined to filter out the meaningful eigenvalues. The threshold is not unique for different models. Moreover, if a multiply connected domain with a inclusion is considered as an acoustic cavity, the boundary of the rigid inclusion generates spurious eigenfrequencies of real numbers. To identify the spurious eigenvalues obtained numerically, we employed the boundary integral equation provided by Burton-Miller's method, by which large imaginary components are added to these spurious eigenvalues.

Although we applied the methodology only to the interior acoustic problem, it can also be a promising solver for the computation of scattering frequencies [46], since it can calculate the complex eigenvalues directly and the BEM satisfies the radiation condition for infinite problem automatically. The resonance of exterior problem remains as a future research topic.

In the next chapter, the Bloch eigenvalue problem is calculated repeatedly for the characterization of the dispersion relation, and the rank detection is performed by observing the difference of singular values. Furthermore, Burton-Miller's method is used to remove the spurious eigenvalues resulted by the embedded scatterers in coefficient matrix of the BEM.

CHAPTER IV

Phononic Structures for Acoustic Problem

4.1 Introduction

The composite structures so-called phononic crystals, which show band structures for acoustic/elastic waves, are considered as elastic analogous extensions of photonic crystals. The existence of band gaps in phononic crystals is also observed by both theoretical studies [23, 24] and experimental investigations [80, 81]. It is shown that the propagation of elastic waves with particular frequencies within band gaps is forbidden by the phononic crystals. This property enables phononic crystals to provide a sound and vibration isolated environment as a result of the created band gaps. Furthermore, phononic crystals can also be used as wave filters or waveguides with a moderate number of dot defects or linear defects distributed in a certain way [82, 83, 84].

Several numerical methods have already been developed for computation of band structures of phononic crystals, for example, plane wave expansion (PWE) method [23, 24, 32], multiple-scattering theory (MST) method [33, 34, 35], finite difference time domain (FDTD) method [36, 37, 85], wavelet method [38] and finite element method (FEM) [39].

The research interest in the analysis of phononic crystals is the band gaps searching. Similar to photonic crystals, numerical analyses of band gaps for phononic crystals usually result in eigenvalue problems. The boundary element method (BEM) is one of the widely used numerical computation tools for wave problems, requiring the discretization of the boundary only. For scattering problems, it satisfies the radiation conditions by giving appropriate Green's function. There are two methodologies of analysis for periodic composite structures: one is to give the Bloch conditions on a unit cell and use the conventional Green's function [40], and the other is to apply the Bloch conditions directly to the wave equation [41, 42]. However, both methodologies

result in nonlinear eigenvalue problems when they are applied to obtaining dispersion curves of phononic crystals. The transcendental eigenequation makes it difficult to solve the eigenvalues by standard eigensolvers directly. For photonic crystals, there is a work in which the nonlinear eigenvalue problem is converted to a generalized one by transforming the system matrix with the former methodology [40].

In this section, the work is undertaken to provide a new methodology of band structure calculation for two-dimensional acoustic phononic crystals. The BEM combined with the block SS method is employed to compute dispersion curves. The constant elements are adopted for simplicity of numerical treatment. We have to mention that the scattering problem analyzed by the BEM yields spurious frequencies, which can be removed by Burton-Miller's method [86]. The application of the technique is demonstrated through band gap analyses of homogenous and composite structures. The results show the effectiveness of the proposed method.

4.2 Formulations

For 2D acoustic phononic crystals, we have the same governing equation in Eq. (3.1), and the fundamental solution in 2D case in Eq. (3.5). Moreover, it is an exterior problem which is defined in an infinite domain and no energy is radiated from infinity to the field, therefore the sound pressure must satisfy the Sommerfeld radiation condition [87]:

$$\lim_{|\xi|\to+\infty} |\xi|^{\frac{\tau-1}{2}} \left(\frac{\partial p(\xi)}{\partial |\xi|} - \mathrm{i}kp(\xi) \right) = 0, \tag{4.1}$$

where τ=2 for 2D case.

Since Burton-Miller's method requires NDBIE, we give the normal derivatives of the 2D fundamental solution as follows,

$$q^*(x,y) = \frac{\partial p^*(x,y)}{\partial n(y)} = -\frac{k\mathrm{i}}{4} H_1^{(1)}(kr) \frac{\partial r}{\partial n(y)}, \tag{4.2}$$

$$\hat{p}^*(x,y) = \frac{\partial p^*(x,y)}{\partial n(x)} = -\frac{k\mathrm{i}}{4} H_1^{(1)}(kr) \frac{\partial r}{\partial n(x)}, \tag{4.3}$$

$$\begin{aligned}\hat{q}^*(x,y) &= \frac{\partial q^*(x,y)}{\partial n(x)} \\ &= -\frac{k^2\mathrm{i}}{8}[H_0^{(1)}(kr) - H_2^{(1)}(kr)]\frac{\partial r}{\partial n(x)}\frac{\partial r}{\partial n(y)} \\ &\quad -\frac{k\mathrm{i}}{4}H_1^{(1)}(kr)\frac{\partial^2 r}{\partial n(x)\partial n(y)}. \end{aligned} \tag{4.4}$$

where $(\ )^*$ denotes the fundamental solution, and $\hat{(\ )} = \partial(\ )/\partial n(x)$.

Let us write the boundary integral equation given by Burton-Miller's method, presented by Eqs. (3.5), (4.2), (4.3) and (4.4) as follows,

$$\begin{aligned}&\frac{1}{2}p(x) + \fint_S q^*(x,y)p(y)\mathrm{d}S(y) - \int_S p^*(x,y)q(y)\mathrm{d}S(y) \\ &+\frac{1}{2}\mu q(x) + \mu\fint_S \hat{q}^*(x,y)p(y)\mathrm{d}S(y) - \mu\fint_S \hat{p}^*(x,y)q(y)\mathrm{d}S(y) = 0, \end{aligned} \tag{4.5}$$

where μ is chosen as $\mathrm{i}/2k$, $\fint$ denotes that the integral is evaluated in the sense of Cauchy-principal value (CPV), $\fint\!\!\!\!\!\!=$ denotes that the integral is evaluated in the sense of finite-part of divergent integral [88]. One can also eliminate the hyper-singularity in Eq. (3.28) using the regularization method [89]. Discretizing Eq. (4.5) with n constant elements, the discretized form of the boundary integral equation is obtained as follows:

$$\begin{aligned}&\frac{1}{2}p^i(x) + \frac{1}{2}\mu q^i(x) + \sum_{j=1}^{n}\int_{S_j}[q^*(x,y) + \mu\hat{q}^*(x,y)]\,\mathrm{d}S(y)p^j(y) \\ &-\sum_{i=1}^{n}\int_{S_j}[p^*(x,y) + \mu\hat{p}^*(x,y)]\,\mathrm{d}S(y)q^j(y) = 0, \end{aligned} \tag{4.6}$$

where S_j denotes j-th element, p^j, q^j are the sound pressure and its normal derivative on the S_j element respectively. Let the integrals in Eq. (4.6) be denoted as

$$\tilde{B}^{ij} = \int_{S_j}[q^*(x,y) + \mu\hat{q}^*(x,y)]\,\mathrm{d}S(y), \tag{4.7}$$

$$\tilde{G}^{ij} = \int_{S_j}[p^*(x,y) + \mu\hat{p}^*(x,y)]\,\mathrm{d}S(y). \tag{4.8}$$

Furthermore, let us write

$$B^{ij} = \begin{cases} \tilde{B}^{ij} & i \neq j \\ \tilde{B}^{ij} + \frac{1}{2} & i = j \end{cases}, \tag{4.9}$$

and

$$G^{ij} = \begin{cases} \tilde{G}^{ij} & i \neq j \\ \tilde{G}^{ij} + \frac{1}{2} & i = j \end{cases}. \tag{4.10}$$

By using the representations in Eqs. (4.9) and (4.10), Eq. (4.6) is written as

$$\sum_{j=1}^{n} B^{ij} p^j = \sum_{j=1}^{n} G^{ij} q^j. \tag{4.11}$$

Assuming the fundamental solution is applied at each center of the constant element, a system of algebraic equations is obtained in the matrix form:

$$\begin{pmatrix} B^{11} & B^{12} & \cdots & B^{1n} \\ B^{21} & B^{22} & \cdots & B^{2n} \\ \vdots & \vdots & \ddots & \vdots \\ B^{n1} & B^{n2} & \cdots & B^{nn} \end{pmatrix} \begin{pmatrix} p^1 \\ p^2 \\ \vdots \\ p^n \end{pmatrix} = \begin{pmatrix} G^{11} & G^{12} & \cdots & G^{1n} \\ G^{21} & G^{22} & \cdots & G^{2n} \\ \vdots & \vdots & \ddots & \vdots \\ G^{n1} & G^{n2} & \cdots & G^{nn} \end{pmatrix} \begin{pmatrix} q^1 \\ q^2 \\ \vdots \\ q^n \end{pmatrix}, \tag{4.12}$$

or

$$\mathbf{Bp} = \mathbf{Gq}, \tag{4.13}$$

where $\mathbf{B}$ and $\mathbf{G}$ are $n \times n$ matrices, $\mathbf{p}$ and $\mathbf{q}$ are vectors that contain the sound pressure and its normal derivative of the boundary element, respectively. Moreover, in this work, both vectors are unknowns but have certain periodic relations given by extra equations.

Let us consider a 2D phononic structure as shown in Fig. 4.1. The cylindrical scatterers, infinitely long in x_3 direction, are periodically collocated in the matrix medium that is assumed to be air in this study. With the radius of the cylinders R, and the lattice constant a, the filling fraction can be obtained as follows,

$$f = \pi R^2 / a^2. \tag{4.14}$$

To calculate the band structure, it is needed to analyze only a unit cell shown in Fig. 4.2(a), and apply the periodic boundary condition on the boundary of the unit cell. The reciprocal lattice and the first Brillouin zone [90] are shown in Fig. 4.2(b).

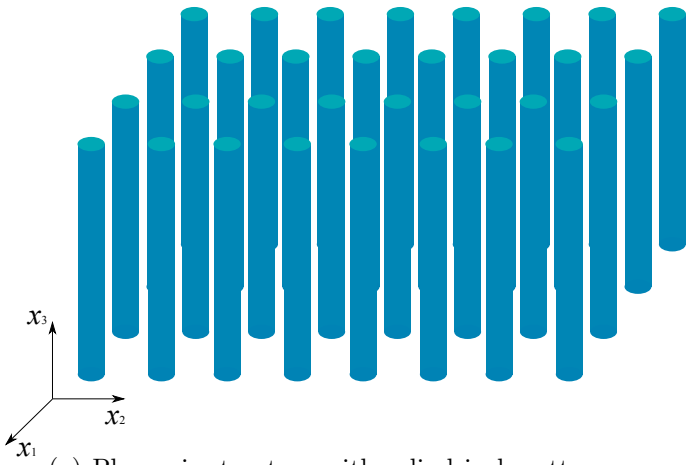

(a) Phononic structure with cylindrical scatterers.

(b) 2D square lattice (dashed line).

Figure 4.1: 2D Phononic crystal.

$\mathbf{k} = (k_1, k_2)$ is the Bloch wave vector in x-y plane.

The periodic structure requires that the sound pressure $p(\mathbf{r})$ must satisfy the following relationship according to the Bloch theorem:

$$p(\mathbf{r} + \mathbf{l}) = \mathrm{e}^{\mathrm{i}\mathbf{k}\cdot\mathbf{l}} p(\mathbf{r}), \tag{4.15}$$

where $\mathbf{l} = n_1\mathbf{a}_1 + n_2\mathbf{a}_2$ is the translation vector, $\mathbf{a}_1$, $\mathbf{a}_2$ are the lattice base vectors. The periodic boundary condition is applied on the boundary elements of the unit cell, which restricts the infinite problem to a bounded one. Because of the symmetry of the Brillouin zone, the wave vector $\mathbf{k}$ varies only along the boundary of the first Brillouin zone: $\mathrm{M} \to \Gamma \to \mathrm{X} \to \mathrm{M}$. Then, all the waves propagating in the composite structure are obtained.

In order to introduce the periodic boundary condition, the elements are separated into three groups: (i) the dependent elements; (ii) the independent elements; (iii) the internal elements, which are illustrated in Fig. 4.3. The dependent elements are represented by open circular symbols, the independent elements are represented by solid circular ones, and internal elements are represented by cross symbols.

The quantities corresponding to the three element groups are represented by the following expressions:

$\mathbf{p}^D, \mathbf{q}^D$: Nodal sound pressure and normal derivative at dependent elements.

$\mathbf{p}^I, \mathbf{q}^I$: Nodal sound pressure and normal derivative at independent elements.

$\mathbf{p}^C, \mathbf{q}^C$: Nodal sound pressure and normal derivative at internal elements.

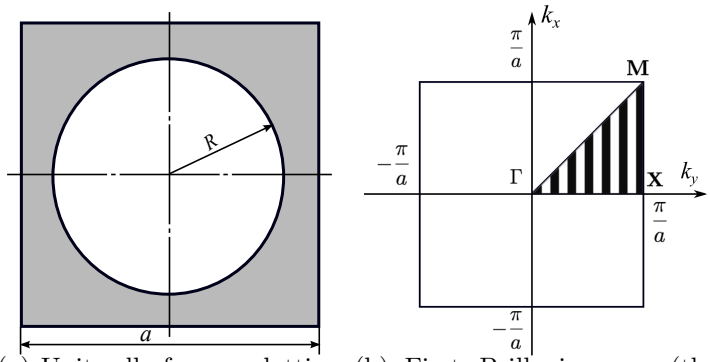

(a) Unit cell of square lattice. (b) First Brillouin zone (the square primitive cell defined in reciprocal space) and the irreducible Brillouin zone (the shade triangular).

Figure 4.2: Unit cell and Brillouin zone.

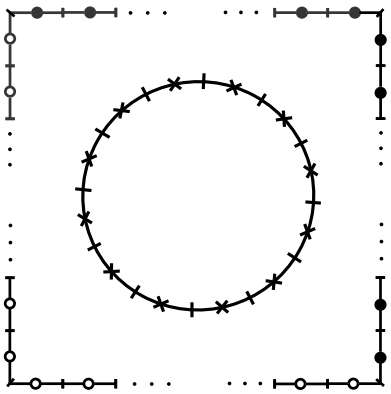

Figure 4.3: The meshed model of the unit cell. The open circular symbols denote the independent element; the solid circular symbols denote the dependent element; the cross symbols denote the internal elements

With the above definitions, Eq. (4.13) can be written as

$$\begin{pmatrix} \mathbf{B}^D & \mathbf{B}^I & \mathbf{B}^C \end{pmatrix} \begin{pmatrix} \mathbf{p}^D \\ \mathbf{p}^I \\ \mathbf{p}^C \end{pmatrix} = \begin{pmatrix} \mathbf{G}^D & \mathbf{G}^I & \mathbf{G}^C \end{pmatrix} \begin{pmatrix} \mathbf{q}^D \\ \mathbf{q}^I \\ \mathbf{q}^C \end{pmatrix}. \tag{4.16}$$

According to Eq. (4.15), $\mathbf{p}^I$ and $\mathbf{p}^D$ satisfy the relation:

$$\mathbf{P}^D = \mathrm{e}^{\mathrm{i}[\mathbf{ka}]_{12}} \mathbf{P}^I, \tag{4.17}$$

for the normal derivatives $\mathbf{q}$, it has the opposite normal direction, so we have

$$\mathbf{q}^D = -\mathrm{e}^{\mathrm{i}[\mathbf{ka}]_{12}}\mathbf{q}^I, \tag{4.18}$$

where $[\mathbf{ka}]_{12} = k_1 a_1$ when the relation between $\mathbf{P}^D$ and $\mathbf{P}^I$ is along the x_1 direction, $[\mathbf{ka}]_{12} = k_2 a_2$ when the relation is along the x_2 direction.

Substituting Eqs. (4.17) and (4.18) into Eq. (4.16), we obtain a system of equations represented only by the quantities of the independent and internal elements. Eq. (4.16) can be rewritten as follows:

$$\begin{pmatrix} \mathbf{B}^D\mathrm{e}^{\mathrm{i}[\mathbf{ka}]_{12}} & \mathbf{B}^I & \mathbf{B}^C \end{pmatrix} \begin{pmatrix} \mathbf{p}^I \\ \mathbf{p}^I \\ \mathbf{p}^C \end{pmatrix} = \begin{pmatrix} -\mathbf{G}^D\mathrm{e}^{\mathrm{i}[\mathbf{ka}]_{12}} & \mathbf{G}^I & \mathbf{G}^C \end{pmatrix} \begin{pmatrix} \mathbf{q}^I \\ \mathbf{q}^I \\ \mathbf{q}^C \end{pmatrix}. \tag{4.19}$$

Then, combining the coefficients column vectors corresponding to the same quantities, we obtain the following system of equations:

$$\begin{pmatrix} \mathbf{B}^D\mathrm{e}^{\mathrm{i}[\mathbf{ka}]_{12}} + \mathbf{B}^I & \mathbf{B}^C \end{pmatrix} \begin{pmatrix} \mathbf{p}^I \\ \mathbf{p}^C \end{pmatrix} = \begin{pmatrix} -\mathbf{G}^D\mathrm{e}^{\mathrm{i}[\mathbf{ka}]_{12}} + \mathbf{G}^I & \mathbf{G}^C \end{pmatrix} \begin{pmatrix} \mathbf{q}^I \\ \mathbf{q}^C \end{pmatrix}. \tag{4.20}$$

We finally obtain the following equations by moving the unknowns to the left-hand side,

$$\begin{pmatrix} \mathbf{B}^D\mathrm{e}^{\mathrm{i}[\mathbf{ka}]_{12}} + \mathbf{B}^I & \mathbf{G}^D\mathrm{e}^{\mathrm{i}[\mathbf{ka}]_{12}} - \mathbf{G}^I & \mathbf{A}^C \end{pmatrix} \begin{pmatrix} \mathbf{p}^I \\ \mathbf{q}^I \\ \mathbf{x}^C \end{pmatrix} = 0, \tag{4.21}$$

where $\mathbf{x}^C$ denotes the unknowns on the internal elements, and $\mathbf{A}^C$ denotes the coefficient matrix of $\mathbf{x}^C$. The constant elements guarantee that the number of dependent elements is equal to that of the independent elements, which results in a square system matrix. Eq. (4.21) can be written in the form of a nonlinear Bloch's eigenvalue problem:

$$\mathbf{F}(\omega)(\mathbf{x}) = 0, \tag{4.22}$$

where $\mathbf{F}$ is a square matrix that contains ω implicitly and transcendentally. In the next section, we use block SS method to solve Eq. (4.22) which determines the dispersion relation.

The calculation of the eigenvalue problem in Eq. (4.22) is carried out repeatedly with given different k_1 and k_2 for the periodic boundary condition. This means that the location of gap in the singular values may change when the periodic boundary

condition is different. Therefore, it is not appropriate to specify a constant threshold δ for the repeated computations with different periodic boundary conditions.

Let $\sigma_1, \sigma_2, \ldots, \sigma_{Kl}$ be the singular values of $\mathbf{H}_{Kl}$, the singular values corresponding to the eigenvalues actually existing in the integration path and the small singular values are separated by a threshold. The threshold is used to determine the rank of the Hankel matrices. Since the threshold values are not the same among different problems, it is necessary to find the location of the gap in the singular values sorted in descendent order. Another set of values $\delta_1, \delta_2, \ldots, \delta_{Kl-1}$ is introduced as follows:

$$\delta_{i-1} = \Delta\sigma_i = \frac{\log_{10}(\sigma_i) - \log_{10}(\sigma_{i-1})}{\Delta h}, \qquad (i = 2, 3, ..., Kl), \tag{4.23}$$

where $\Delta h = i - (i-1) = 1$. The set of δ_i implies the variation of singular values. If δ_i is larger than a threshold δ^*, it is indicated that the $(i+1)$-th singular value can be considered as a small singular value that should be removed. In this thesis, $\delta^* = 1$ is chosen. It is noted that Kl is rather small and the computation cost for SVD is negligible.

4.3 Numerical examples

4.3.1 Phononic crystal with rigid cylinders

In Fig. 4.4, the unit cell of the analysis model including rigid cylinders in the medium is shown. The parameters of the homogeneous structure are shown in Tab. 6.1. The unit cell with the periodic boundary condition results in a plane exterior problem of a circular boundary.

Table 4.1: The parameters of homogenous structure

Domain	Density [kg/m^3]	Wave speed [m/s]	Filling fraction
1	$\rho_1 = 1.22$	$C_1 = 337.20$	$f = 0.55$

The eigenfrequencies of the structure are extracted with CBIE and Burton-Miller's method. The results are shown in Fig. 4.5 and Fig. 4.6, respectively. The integration path is a circle in the complex plane, centered at $\gamma = (2550, 0)$ and its radius is $\rho = 2000$, the range of eigenvalues to calculate is $[550, 4550]$.

The dispersion curve in Fig. 4.5 indicates that some spurious eigenfrequencies are also obtained, compared with previous research [25]. When the wave vector k is varying, the spurious eigenfrequencies are constants, and observed as horizontal

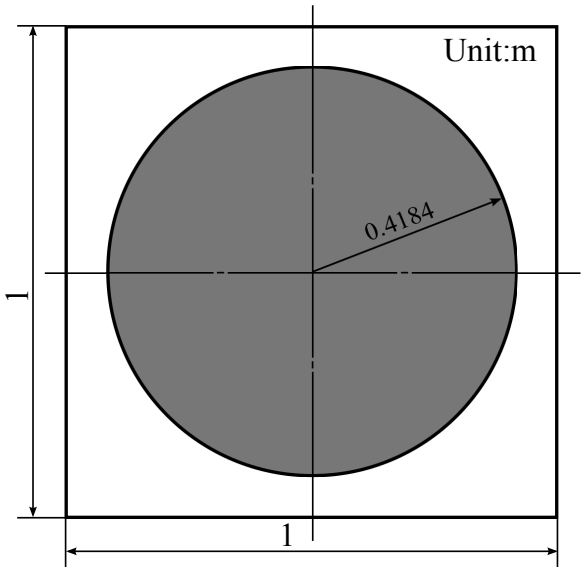

Figure 4.4: The unit cell with a rigid scatterer (the rigid scatterer is shown in gray and the matrix material is in white).

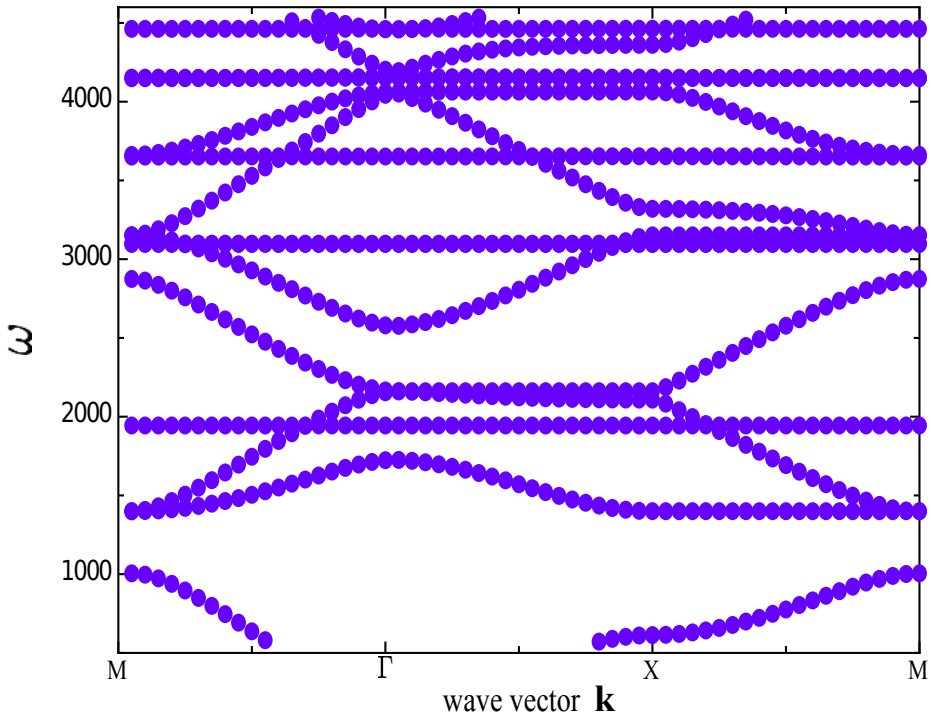

Figure 4.5: Dispersion curves obtained for the homogenous model by CBIE.

lines in Fig. 4.5. These real spurious eigenfrequencies correspond to the boundary of the rigid cylinder with Neumann boundary condition. This means the eigenvalue problem for interior closed boundary is also computed by the block SS method.

These real spurious eigenfrequencies satisfy

$$J_j\left(\frac{\omega R}{c}\right) = 0, \qquad (j = 0, 1, 2, \cdots), \tag{4.24}$$

where J_j is the Bessel function of the j-th order. The spurious eigenfrequencies are related to the zeros of the Bessel function. These real spurious eigenvalues are produced by the interior of the circular closed boundary, and they are called Neumann eigenvalues [91].

Since complex eigenvalues are also included in the results, we pick out the real ones by checking the values of the imaginary part. The imaginary part must satisfy the following condition:

$$\frac{\mathrm{Im}(\omega)}{\rho} < \beta, \tag{4.25}$$

where β is a very small positive threshold. In the present work, it is taken as $\beta = 0.0085$.

However, those real spurious eigenfrequencies cannot be distinguished in this way because they do not result from numerical error, but from a mathematical reason. Burton-Miller's method [86] can add a relatively large imaginary part to the real spurious eigenfrequencies. Hence, we can exclude these spurious frequencies from the results.

We find that from the comparisons of the results shown in Fig. 4.5 and Fig. 4.6 the horizontal lines formed by real spurious eigenfrequencies are removed by applying Burton-Miller's method. Actually, the real spurious ones are moved to one side of the real axis, then eliminated by considering their large imaginary parts.

The dispersion curves illustrated in Fig. 4.6 show excellent agreement with the results given by the literature [25].

4.3.2 Phononic crystal with composite mediums

We show in Fig. 4.7 a unit cell containing an inclusion in the medium.

Tab. 4.2 contains the material constants and parameters of the composite structure. The structure of the previous example has a closed boundary, and Neumann boundary condition is given on it, however, the boundary of domain 1 of this example is the interface between domain 1 and domain 2.

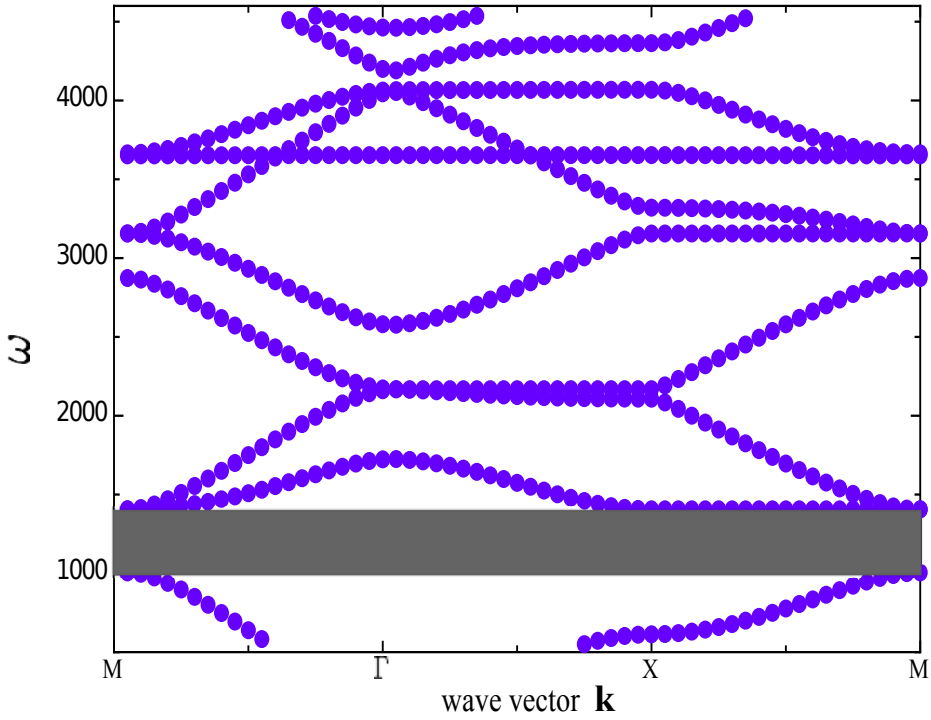

Figure 4.6: Dispersion curves obtained for the homogenous model by Burton-Miller's method. The shaded range implies the band gap.

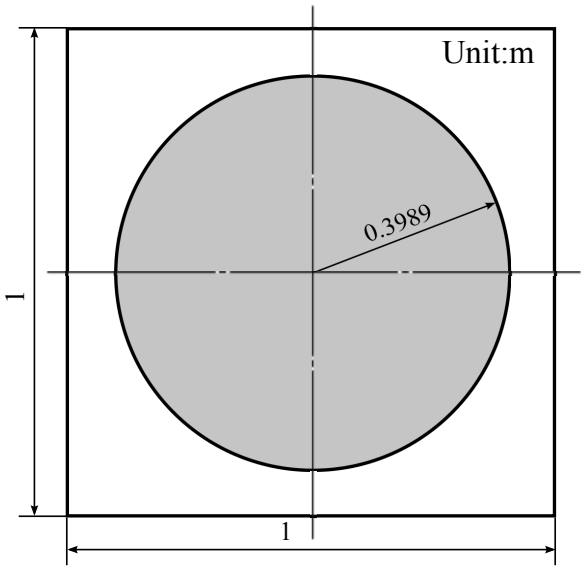

Figure 4.7: The unit cell with an inclusion (domain 2 is shown in gray and domain 1 is shown in white).

Table 4.2: The parameters of composite structure

Domain	Density [kg/m^3]	Wave speed [m/s]	Filling fraction
1	$\rho_1 = 1.22$	$C_1 = 337.20$	$f = 0.5$
2	$\rho_2 = 0.09$	$C_2 = 1241.50$	

The results presented in this section are aimed to illustrate that the spurious eigenfrequencies are also generated by the interior closed interface. It should be noted that the spurious eigenfrequencies are decided by the material of domain 1 but not by that of domain 2. The results in Fig. 4.8 are also showing spurious

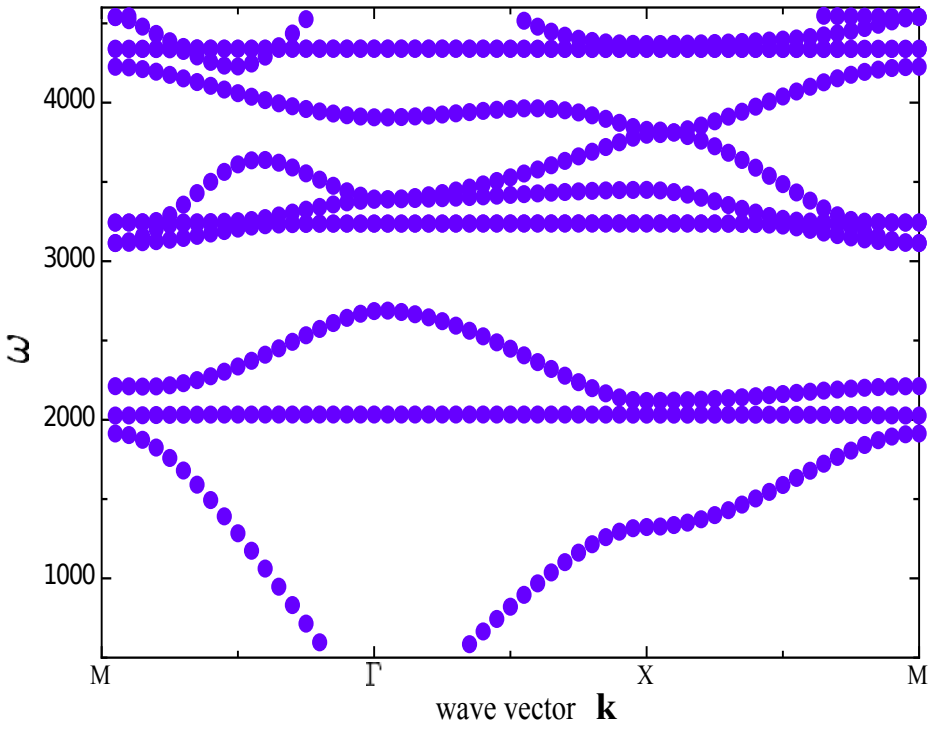

Figure 4.8: Dispersion curves of the composite model obtained by CBIE

eigenfrequencies as those shown in Fig. 4.5. The boundary condition on the interior boundary between domain 1 and domain 2 is different from Neumann boundary condition in this example.

Because the filling fraction is different in this example, the real spurious eigenfrequencies are different from those of the previous example, but, they also satisfy Eq. (4.24). This means that they are also the eigenfrequencies corresponding to the circular domain with the Neumann boundary condition on its boundary. It may be found in the results shown in Fig. 4.9 that the spurious eigenfrequencies are also removed

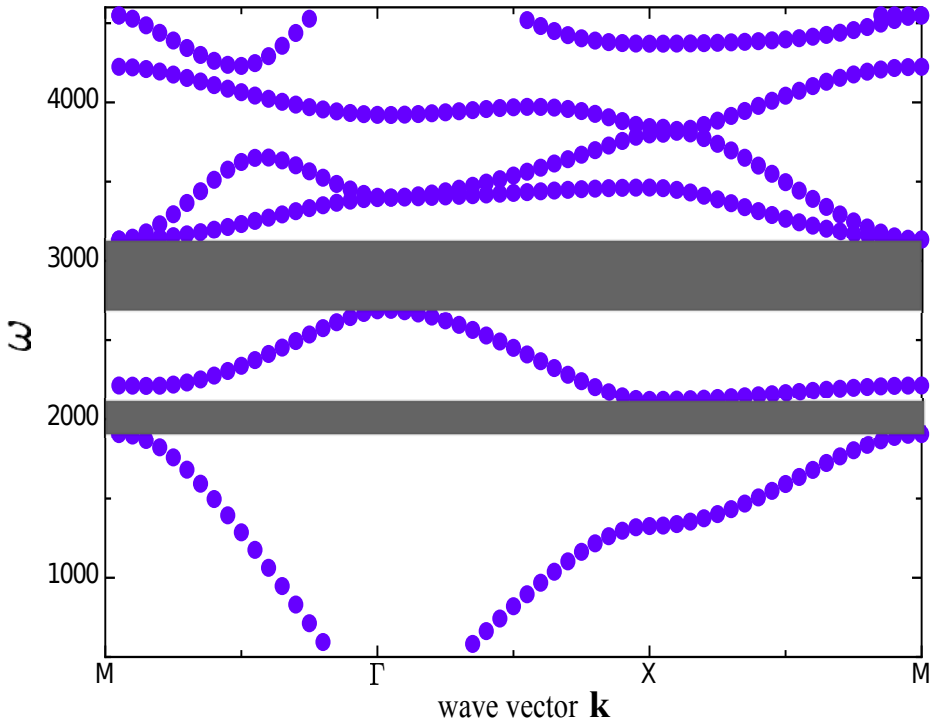

Figure 4.9: Dispersion curves of the composite model obtained by applying Burton-Miller's method. The shaded ranges imply the band gaps.

using Burton-Miller's method. For this phononic composite structure, two band gaps are found in the band structure in the same range as that of Fig. 4.6.

4.4 Conclusion

In this chapter, the present approach has been demonstrated to be effective through the numerical examples for eigenfrequency analyses of phononic structures. A new methodology for calculations of band structures of acoustic phononic composite structures is presented. This is achieved by combining the BEM with the block SS method. The band gaps have been observed correctly both in homogeneous and composite phononic structures. When applying the CBIE, the spurious real eigenfrequencies have appeared in the dispersion curves as the eigenfrequencies of the inclusions with the Neumann boundary conditions. To exclude the spurious eigenfrequencies, Burton-Miller's method, which adds a number that has a large imaginary component on the real spurious ones, can be used.

In next chapter, the methodology is applied to the elastic phononic structures, and a new integration path is proposed to exclude the complex eigenvalues which are

considered as spurious ones in the calculation of band structure of phononic crystals.

CHAPTER V

Phononic Structures for Linear Elastic Problem

5.1 Introduction

The frequency-banded nature of phononic crystals is usually based on two mechanisms: Bragg scattering and local resonances. The former one usually exists in the structure that has stiff/dense scatterers imbedded in a soft/light host periodically [23] and the latter one is caused by the local resonances of the soft material coated scatterers embedded in a stiff host [92].

The band structures of the acoustic phononic structures have been investigated by combining the BEM with the block SS method in the last chapter. For multiply connected domains, the eigenvalue problem formulated by the BEM may yield real spurious eigenfrequencies that also exist in the Bloch eigenvalue problem of phononic crystals. Using Burton-Miller's method, the real spurious eigenfrequencies are shifted by adding components with imaginary parts. Then they can be identified.

In this chapter, the method is extended to the analyses of elastic phononic crystals. The elastic waves propagating in elastic mediums are more complicated since they have both longitudinal and transverse waves. The real spurious eigenfrequencies are moved off the real axis by using Burton-Miller's method, but they may still stay in the contour integration path. This means that the total number of eigenfrequencies within the contour integration path is not reduced. However, for interior problems with linear elastic materials, only those real eigenfrequencies that correspond to the true eigensolutions are required. The additional spurious complex eigenfrequencies may result in higher computing cost. To compute large number of eigenfrequencies, higher order of the moment matrices or more nonzero arbitrary column vectors are required. The higher order of the moment matrices, however, requires more collocation points along the contour integration path to keep the accuracy [56]. Each

collocation point requires to solve a response problem by the BEM. The increase in nonzero arbitrary column vectors also results in more computing cost and memory consumption. In order to exclude the complex spurious eigenfrequencies from solving the domain surrounded by the contour integration path in the complex plane, a fusiform integration path is proposed to confine the selected domain close to the neighborhood of the real axis. The proposed method is applied to three types of phononic structures: a two-phase phononic structure based on Bragg scattering, a unidirectional phononic plate and a three-phase phononic structure. The numerical results show the effectiveness of the proposed method for elastic phononic crystals. The complex spurious eigenfrequencies are also excluded by the fusiform integration path effectively.

5.2 Formulations

Considering an elastic wave propagating in a homogeneous and isotropic medium without body force, the expression of governing continuum equation by displacements is

$$(C_1^2 - C_2^2)u_{j,je}(x,t) + C_2^2 u_{e,jj}(x,t) = \ddot{u}_e(x,t) \;\; x \in \Omega,\; t \in [0,\infty],\; (e,j=1,2) \quad (5.1)$$

where x is a point in the domain Ω, t is time, u_e denotes the e-th component of the displacement vector, $\ddot{u}_e$ is the second derivative of u_e with respect to time. An index after a comma denotes a differentiation with respect to the coordinate corresponding to the index, and the summation convention is applied for repeated indices. C_1 and C_2 are the P (longitudinal) wave speed and S (transverse) wave speed respectively, written as,

$$C_1 = \sqrt{(\bar{\lambda} + 2\bar{\mu})/\bar{\rho}} = \sqrt{E(1-\bar{\nu})/\big\{\bar{\rho}(1+\bar{\nu})(1-2\bar{\nu})\big\}}, \quad (5.2)$$

$$C_2 = \sqrt{\bar{\mu}/\bar{\rho}} = \sqrt{E/\big\{2\bar{\rho}(1+\bar{\nu})\big\}}, \quad (5.3)$$

where $\bar{\rho}$ is the density of the medium, $\bar{\lambda}$ and $\bar{\mu}$ are Lamé's constants, E is Young's modulus, and $\bar{\nu}$ is Poisson's ratio.

For free vibration, no excitation is considered, hence the displacement can be written in a time-independent form:

$$u_e(x,t) = U_e(x,\omega)\mathrm{e}^{-\mathrm{i}\omega t}. \quad (5.4)$$

Substituting Eq.(5.4) into (5.1), the time-independent form of governing equation is obtained as follows:

$$(C_1^2 - C_2^2)U_{j,je}(x,\omega) + C_2^2 U_{e,jj}(x,\omega) + \omega^2 U_e(x,\omega) = 0. \tag{5.5}$$

The boundary integral equation corresponding to the above differential equation is obtained as [93]

$$\begin{aligned} c_{el}(y)U_e(y,\omega) + \int_S t^*_{el}(x,y,\omega)U_e(x,\omega)\mathrm{d}S(x) \\ - \int_S u^*_{el}(x,y,\omega)T_e(x,\omega)\mathrm{d}S(x) = 0 \quad y \in S, \end{aligned} \tag{5.6}$$

where S is the boundary of the domain, c_{el} depends on the geometry of the boundary at point y, the kernels $u^*_{el}(x,y)$ and $t^*_{el}(x,y)$ are known as displacement and traction fundamental solutions which are given for two-dimensional case [93] as

$$u^*_{el}(x,y) = \frac{1}{2\pi\bar{\rho}C_2^2}\left[\psi\delta_{el} - \chi r_{,e}r_{,l}\right], \tag{5.7}$$

$$\begin{aligned} t^*_{el}(x,y) = \frac{1}{2\pi}\Bigg\{ \left(\frac{d\psi}{dr} - \frac{1}{r}\chi\right)\left(\delta_{el}\frac{\partial r}{\partial n} + r_{,l}n_e\right) - \frac{2}{r}\chi\Bigg(n_e r_{,l} \\ - 2r_{,e}r_{,l}\frac{\partial r}{\partial n}\Bigg) - 2\frac{d\chi}{dr}r_{,e}r_{,l}\frac{\partial r}{\partial n} + \left(\frac{C_1^2}{C_2^2} - 2\right)\left(\frac{\psi}{dr} - \frac{d\chi}{dr} - \frac{1}{r}\chi\right)r_{,e}n_l\Bigg\}, \end{aligned} \tag{5.8}$$

where δ_{el} is Kronecker's delta, $r = |x-y|$, n_i is the unit of the outward normal vector to the boundary, and

$$\psi = K_0\left(\frac{sr}{C_2}\right) + \frac{C_2}{sr}\left[K_1\left(\frac{sr}{C_2}\right) - \frac{C_2}{C_1}K_1\left(\frac{sr}{C_1}\right)\right], \tag{5.9}$$

$$\chi = K_2\left(\frac{sr}{C_2}\right) - \frac{C_2^2}{C_1^2}K_2\left(\frac{sr}{C_1}\right), \tag{5.10}$$

where $s = \mathrm{i}\omega$, and K_0, K_1, and K_2 are the modified Bessel functions of order 0, 1, and 2, respectively.

Discretizing Eq.(5.6) with N constant boundary elements, a linear equation is

obtained as follows:

$$c_{el}(y)U_e^i(y,\omega) + \sum_{h=1}^{N}\left(\int_{S_h} t_{el}^*(x,y,\omega)\,\mathrm{d}S(x)\right)U_e^h(x,\omega) - \sum_{h=1}^{N}\left(\int_{S_h} u_{el}^*(x,y,\omega)\,\mathrm{d}S(x)\right)T_e^h(x,\omega) = 0, \tag{5.11}$$

where $c_{el} = \frac{1}{2}\delta_{el}$ when the boundary is smooth, and $U_e^h(y,\omega)$ and $T_e^h(x,\omega)$ denote e-th component of the displacement and traction on boundary S_h of the h-th element.

Let i vary from 1 to N, then a system of $2N$ linear algebraic equations is obtained as

$$\mathbf{BU} = \mathbf{GT}, \tag{5.12}$$

where $\mathbf{U}$, $\mathbf{T} \in \mathbb{C}^{2N}$, and $\mathbf{B}$, $\mathbf{G} \in \mathbb{C}^{2N\times 2N}$, formed by the following 2×2 local matrices:

$$\begin{aligned}\mathbf{b}^{ih} &= [b_{le}],\\ \mathbf{g}^{ih} &= [g_{le}],\end{aligned} \tag{5.13}$$

where $\mathbf{b}^{ih}$, $\mathbf{g}^{ih}$, $\in \mathbb{C}^2$, $(i,h = 1,2,...,N)$ and

$$\begin{aligned}b_{le} &= \int_{S_h} t_{el}^*(x,y,\omega)\mathrm{d}S(x),\\ g_{le} &= \int_{S_h} u_{el}^*(x,y,\omega)\mathrm{d}S(x).\end{aligned} \tag{5.14}$$

A 2D phononic structure is shown in Fig. 5.1 wherein scatterers are imbedded in a host periodically and the square area enclosed by dashed lines denotes a square unit cell.

The unit cell shown in Fig. 5.2 has the additional virtual square boundary which is divided into two groups: dependent boundary (in black color) denoted by subscript 'D' and independent boundary (in gray color) denoted by subscript 'I'. The boundary of scatterer is denoted by the subscript 'C'.

With above definitions for boundaries of the unit cell, the system matrix for the unit cell can be written as

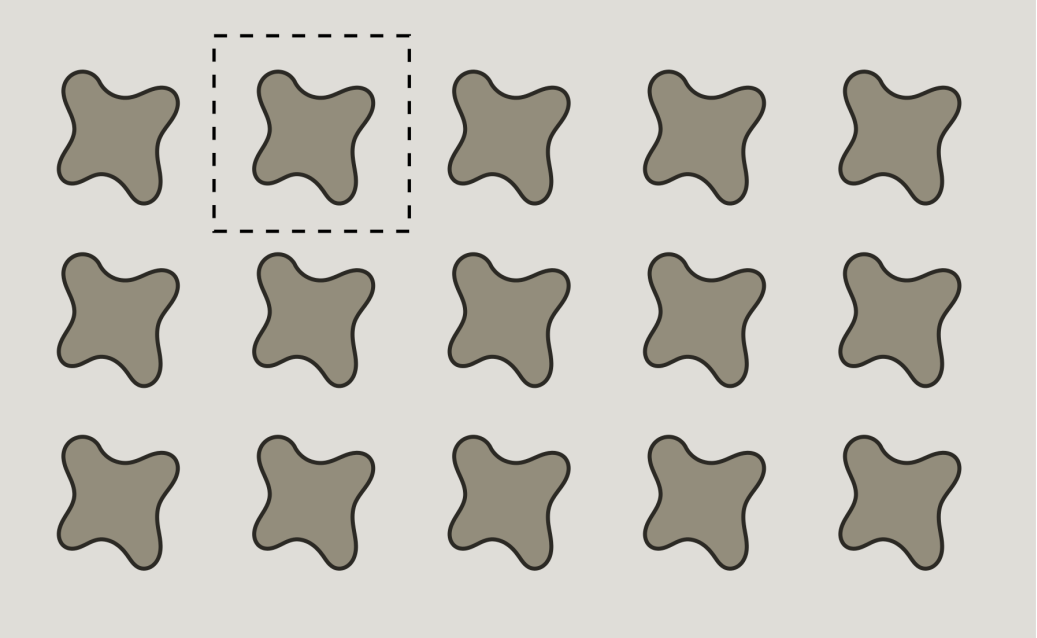

Figure 5.1: 2D two-phase elastic phononic crystal.

$$\begin{pmatrix} \mathbf{B}_I & \mathbf{B}_D & \mathbf{B}_C \end{pmatrix} \begin{pmatrix} \mathbf{U}_I \\ \mathbf{U}_D \\ \mathbf{U}_C \end{pmatrix} = \begin{pmatrix} \mathbf{G}_I & \mathbf{G}_D & \mathbf{G}_C \end{pmatrix} \begin{pmatrix} \mathbf{T}_I \\ \mathbf{T}_D \\ \mathbf{T}_C \end{pmatrix}. \tag{5.15}$$

Usually, the homogeneous boundary conditions:

$$\begin{aligned} \bar{U}_C(x) &= 0 \quad x \in S_U, \\ \bar{T}_C(x) &= 0 \quad x \in S_T, \end{aligned} \tag{5.16}$$

are given to the boundary $S_C = S_U \bigcup S_T$ for free vibrations.

The Bloch theorem makes the quantities of displacements and tractions on dependent boundary S_D and independent boundary S_I hold,

$$\mathbf{U}_D = \mathrm{e}^{[\mathbf{ka}]_{12}} \mathbf{U}_I, \tag{5.17}$$

$$\mathbf{T}_D = (-\mathrm{e}^{[\mathbf{ka}]_{12}}) \mathbf{T}_I, \tag{5.18}$$

where $[\mathbf{ka}]_{12} = k_1 a_1$ when the relation between $\mathbf{U}^D$ and $\mathbf{U}^I$ is along the x_1 direction, $[\mathbf{ka}]_{12} = k_2 a_2$ when the relation is along the x_2 direction. The normal direction of traction is opposite, therefore, a minus symbol is added in Eq. (5.18).

Substituting the periodic boundary conditions Eqs. (5.17), (5.18) and homoge-

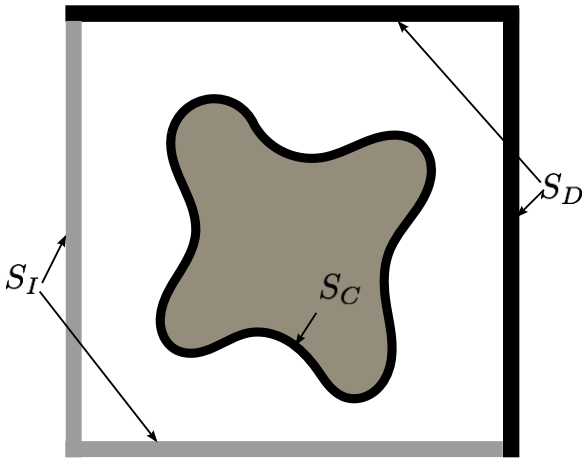

Figure 5.2: A square unit cell (the boundary of the square in black denotes the dependent boundary, and the one in gray denotes the independent boundary).

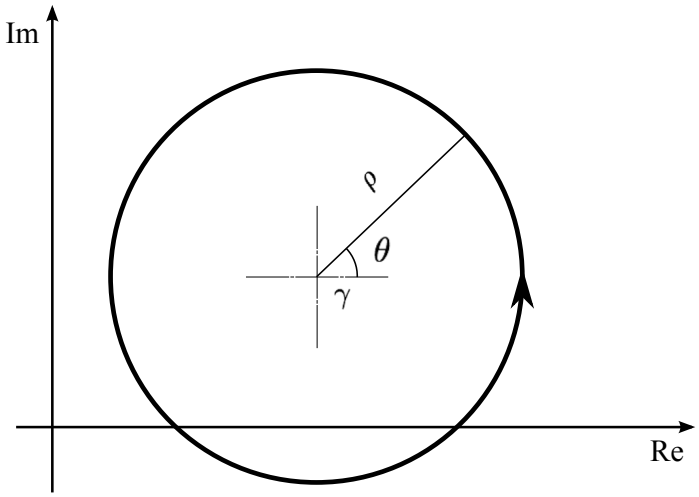

Figure 5.3: The circular contour integration path.

neous boundary condition Eq. (5.16) into Eq. (5.15), and moving all unknown quantities to left-hand side, the following equations can be obtained as

$$\left(\begin{array}{ccc} \mathbf{B}_I + \mathbf{B}_D \mathrm{e}^{[\mathbf{ka}]_{12}} & \mathbf{G}_I - \mathbf{G}_D \mathrm{e}^{[\mathbf{ka}]_{12}} & \mathbf{A}_C \end{array} \right) \left(\begin{array}{c} \mathbf{U}_I \\ \mathbf{T}_I \\ \mathbf{X}_C \end{array} \right) = \mathbf{0}. \tag{5.19}$$

where $\mathbf{X}_C$ is the unknown vector of quantities on the S_C. By now, a similar form of Eq. (4.22) is obtained.

Considering the circular integration path adopted by now depicted in Fig. 5.3, not only the real axis but also a certain area of complex plane is enclosed by the

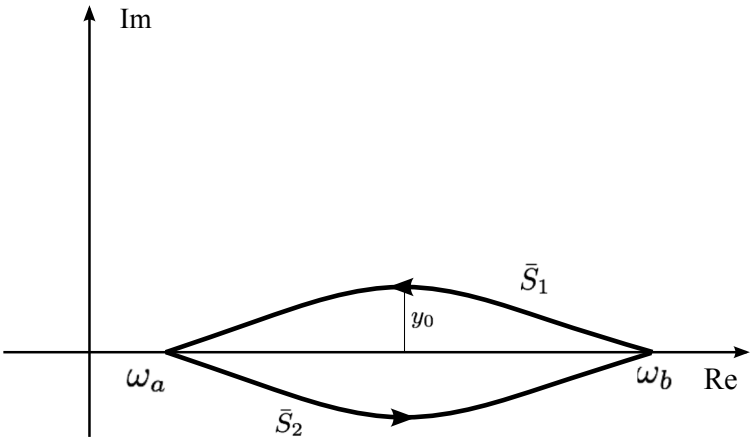

Figure 5.4: The shuttle contour integration path.

circular contour integration path. In some cases, there are spurious eigenfrequencies that have large imaginary parts and exist in the contour integration path, usually this phenomenon depends on the problem we solved. However, the increase of the number of eigenfrequencies located within the integration path requires higher order moment matrices, more number of $\mathbf{v}$ vectors, or more collocation points. To avoid these complex eigenfrequencies, we propose a new shape of integration path shown in Fig. 5.4 which excludes the complex eigenfrequencies.

Let $z = \xi + \mathrm{i}\eta$, and the proposed fusiform integration path in Fig. 5.4 is defined as follows:

$$\bar{S}_1 = \xi + \mathrm{i}y_0 \sin\left(\frac{\xi - \omega_a}{\omega_b - \omega_a}\pi\right), \tag{5.20}$$

$$\bar{S}_2 = \xi - \mathrm{i}y_0 \sin\left(\frac{\xi - \omega_a}{\omega_b - \omega_a}\pi\right), \tag{5.21}$$

where $[\omega_a, \omega_b]$ is the solving range for real eigenfrequencies, and y_0 is the largest amplitude of the imaginary part $|\eta|$.

The fusiform domain enclosed by $\bar{S}_1$ and $\bar{S}_2$ defined in Eqs. (5.20) and (5.21) provides a parameter y_0 that can be specified to exclude the eigenfrequencies whose imaginary parts are larger than it. Since the complex eigenfrequencies with large imaginary parts are are filtered out, the order of the moment matrices, the number of nonzero random vectors, or the number of collocation points can be chosen as a smaller number. This means that the proposed fusiform integration path is more efficient in solving real eigenvalue problems. In this work, the contour integral along

$\bar{S}_1$ and $\bar{S}_2$ is also evaluated by trapezoidal rule. The interval $[\omega_a, \omega_b]$ is discretized into $\bar{N} = N/2$ subranges equally by $\bar{N}+1$ points $\xi_1, \xi_2, ..., \xi_{\bar{N}+1}$ and $\bar{h} = (\omega_b - \omega_a)/\bar{N}$. The collocation points on the contour integration path $\bar{S}_1$ and $\bar{S}_2$ can be written as

$$p_n = \xi_n + \mathrm{i}y_0 \sin\left(\frac{\xi_n - \omega_a}{\omega_b - \omega_a}\pi\right) \text{ on } \bar{S}_1 \tag{5.22}$$

$$\bar{p}_n = \xi_n - \mathrm{i}y_0 \sin\left(\frac{\xi_n - \omega_a}{\omega_b - \omega_a}\pi\right) \text{ on } \bar{S}_2 \tag{5.23}$$

where $n = 1, 2, ..., \bar{N} + 1$.

The moment matrices of order m can be obtained by evaluating the summation of the following two parts:

$$\mathbf{M}_m \approx \hat{\mathbf{M}}_m = \hat{\mathbf{M}}_m^1 + \hat{\mathbf{M}}_m^2 \tag{5.24}$$

where $\hat{\mathbf{M}}_m^1$ and $\hat{\mathbf{M}}_m^2$ are the integrals evaluated numerically along $\bar{S}_1$ and $\bar{S}_2$, respectively, as follows:

$$\hat{\mathbf{M}}_m^1 = \frac{\bar{h}}{4\pi\mathrm{i}}\left[\mathbf{F}^1{}_m(p_1) + 2\mathbf{F}^1{}_m(p_2) + 2\mathbf{F}^1{}_m(p_3) + \cdots + 2\mathbf{F}^1{}_m(p_{\bar{N}}) + \mathbf{F}^1{}_m(p_{\bar{N}+1})\right] \tag{5.25}$$

$$\hat{\mathbf{M}}_m^2 = \frac{\bar{h}}{4\pi\mathrm{i}}\left[\mathbf{F}^2{}_m(\bar{p}_1) + 2\mathbf{F}^2{}_m(\bar{p}_2) + 2\mathbf{F}^2{}_m(\bar{p}_3) + \cdots + 2\mathbf{F}^2{}_m(\bar{p}_{\bar{N}}) + \mathbf{F}^2{}_m(\bar{p}_{\bar{N}+1})\right] \tag{5.26}$$

where $\mathbf{F}_m^1$ and $\mathbf{F}_m^2$ are defined as follows:

$$\mathbf{F}^1{}_m(p_n) = -\left[\mathbf{U}^H\mathbf{A}^{-1}(p_n)\mathbf{V}\right] p_n^m \left[1 + \frac{\mathrm{i}\pi y_0}{\omega_b - \omega_a}\cos\left(\frac{\xi_n - \omega_a}{\omega_b - \omega_a}\pi\right)\right] \tag{5.27}$$

$$\mathbf{F}^2{}_m(\bar{p}_n) = \left[\mathbf{U}^H\mathbf{A}^{-1}(\bar{p}_n)\mathbf{V}\right] p_n^m \left[1 - \frac{\mathrm{i}\pi y_0}{\omega_b - \omega_a}\cos\left(\frac{\xi_n - \omega_a}{\omega_b - \omega_a}\pi\right)\right] \tag{5.28}$$

5.3 Numerical examples

5.3.1 Phononic structure based on Bragg scattering

A unit cell which contains a square inclusion is shown in Fig. 5.5, where domain in gray color assumed to be a stiff and dense material (denoted by subscript '2') and the domain in white color is assumed to be a compliant and light material (denoted by subscript '1'). The material constants are given in Fig. 5.1 This 2D structure is considered to be periodic in x_1 and x_2 directions.

Let the wave vector $\mathbf{k}$ vary along the boundary of irreducible Brillouin zone M $\rightarrow$

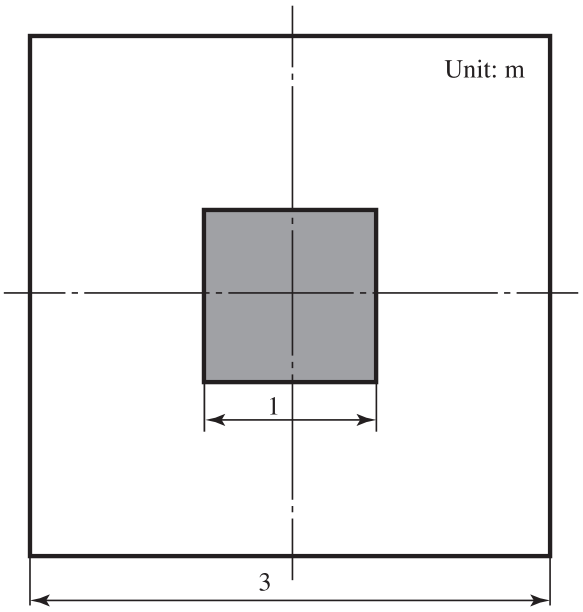

Figure 5.5: A square unit cell with a square inclusion(the white denotes the material 1, the gray denotes the material 2).

Table 5.1: The material constants for the phononic structure based on the Bragg scattering and the phononic plate

Material	Density [kg/m^3]	Young's modulus [Pa]	Poisson's ratio
1	$\bar{\rho}_1 = 2.0 \times 10^3$	$E_1 = 7.8 \times 10^6$	$\bar{\nu}_1 = 0.34$
2	$\bar{\rho}_2 = 1.6 \times 10^4$	$E_2 = 1.248 \times 10^8$	$\bar{\nu}_2 = 0.34$

$\Gamma \rightarrow \mathrm{X} \rightarrow \mathrm{M}$, and the eigenfrequencies ω is computed to plot the dispersion curves as shown in Fig. 5.6. The band structure obtained by the proposed method shows a good agreement with the result in the reference [94] which has used the same material ratio definition: $\bar{\rho}_1/\bar{\rho}_2 = 1/8$, $E_1/E_2 = 1/16$, $\bar{\nu}_1 = \bar{\nu}_2 = 0.34$, and employed FEM based on reduced Bloch mode expansion.

The parameters of the block SS method for both integration paths are as follows: $N = 128$, $K = 4$, $l = 30$. The selected range for the real axis is [10, 110] [Hz]. For simplicity, $\mathbf{k}$ varies only along $\mathrm{M} \rightarrow \Gamma$. The comparison between the numbers of eigenfrequencies obtained by the circular integration path and fusiform integration path is shown in Fig. 5.7. It is found that the circular integration path extracts more eigenfrequencies including complex and real eigenfrequencies outside the selected range. Furthermore, at two points, the numbers of eigenfrequencies are zero, and this means that the number of collocation points N is insufficient for observing the gap in singular values. It is also found that the results obtained by fusiform integration path

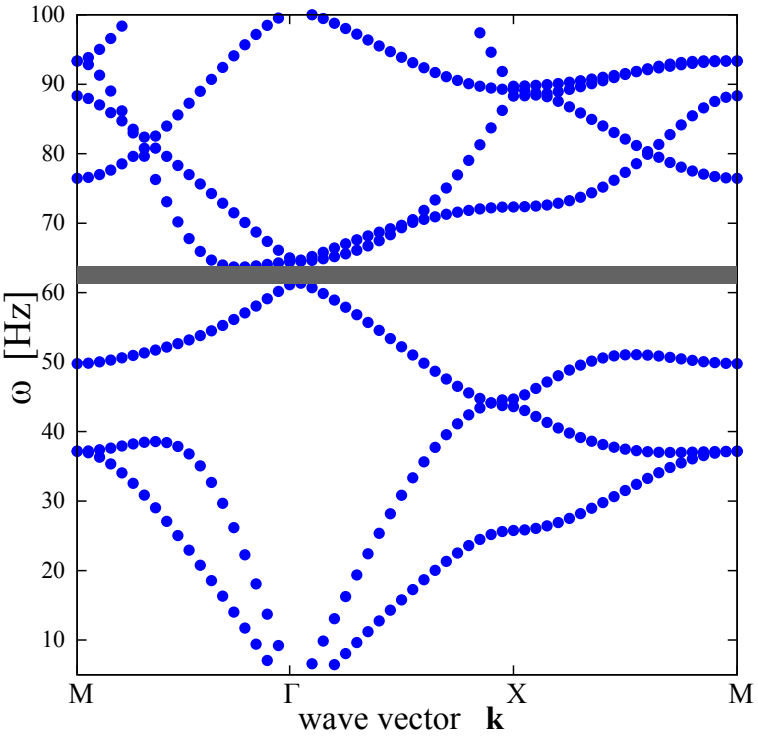

Figure 5.6: The band structure of phononic crystal in Fig.5.5.

are more close to the analytical solutions. The numbers of extra real eigenfrequencies obtained by the two integration paths are also shown in Fig. 5.8. It can be seen that more eigenfrequencies located outside the selected range are obtained by the circular integration path. It implies that the extension of the implicit filter function for the fusiform path is smaller than that of the filter function for circular path.

5.3.2 Phononic plate defined in unidirection with a traction-free boundary condition

Let us see the simple alternative layer structure shown in Fig. 5.10. The filling fraction for material 1 and 2 is 1:1, and the white denotes the material 1 and the gray denotes the material 2. Different from example 1, the periodicity is only exist in one direction, and the traction-free boundary condition is given on the top and bottom boundaries. This structure can be considered as a phononic crystal plate in which the irreducible Brillouin zone of the unit cell is the interval $[0, \pi/d]$. The wave number k now is a scalar and varies from 0 to π/d. The band structure is shown in Fig. 5.10 wherein three band gaps (gray ranges) are found in the selected range $[10, 130]$ [Hz]. For this structure, the numbers of eigenfrequencies obtained by the circular and fusiform integration paths are also presented in Fig. 5.11, as k is varying

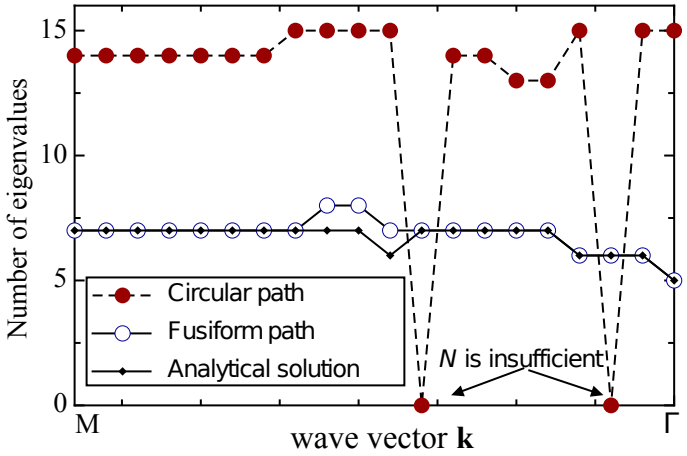

Figure 5.7: The number of eigenfrequencies obtained by the circular path and fusiform path.

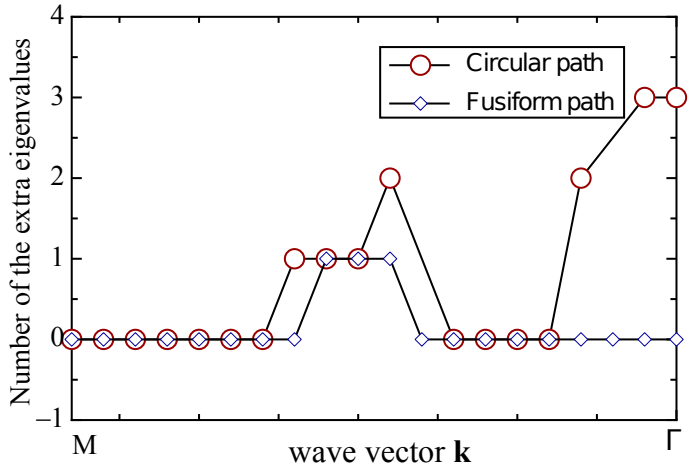

Figure 5.8: The number of extra eigenfrequencies outside the selected range obtained by the circular path and fusiform path .

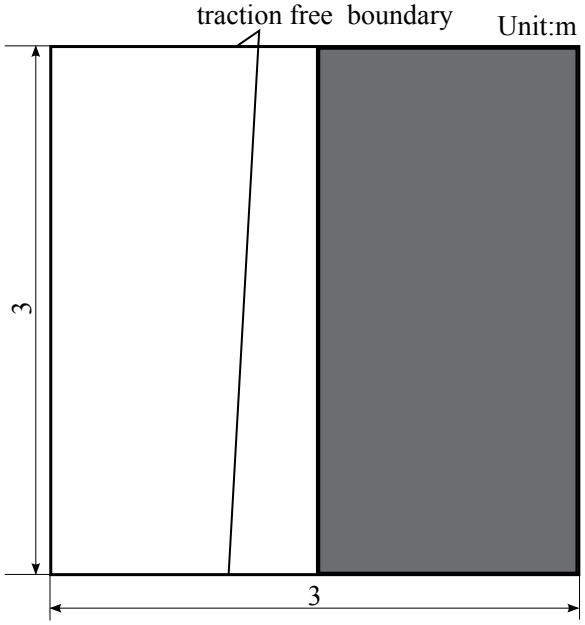

Figure 5.9: A unit cell composed of alternative material layers (the white denotes the material 1, the gray denotes the material 2).

from 0 to π/d, with $N = 128$, $K = 4$, $l = 30$ and selected range $[10, 130]$ [Hz]. From Fig. 5.11, it can be seen that the complex eigenfrequencies are filtered out by the fusiform integration path. In Fig. 5.12, similar as the previous example, at some points, more number of extra real eigenfrequencies near to the circular integration path are obtained than that of the extra real eigenfrequencies obtained by fusiform integration path.

5.3.3 Three-phase phononic structure

In this numerical example, we consider a square shape stiff inclusion coated with soft material imbedded in stiff material as shown in Fig. 5.13. The material for the square shape inclusion is considered to be the same as the host material. Here, we use a soft material for the coating material and the material constants shown in Fig. 5.2. The material constant ratios become as $\bar{\rho}_1/\bar{\rho}_2 = 1/8$, $E_1/E_2 = 1/160$. The high contrast between the materials of the coating layer and scatterer present a band gap as shown in Fig. 5.14. The parameters for the block SS method are $N = 200$, $K = 4$, $l = 30$, and selected range for real axis [10, 70] [Hz].

In Fig. 5.15, the total numbers of eigenfrequencies obtained by the circular and fusiform integration paths are shown as $\mathbf{k}$ varies from M to Γ. From Fig. 5.15, the only one mismatch between the results obtained by the fusiform integration path and the

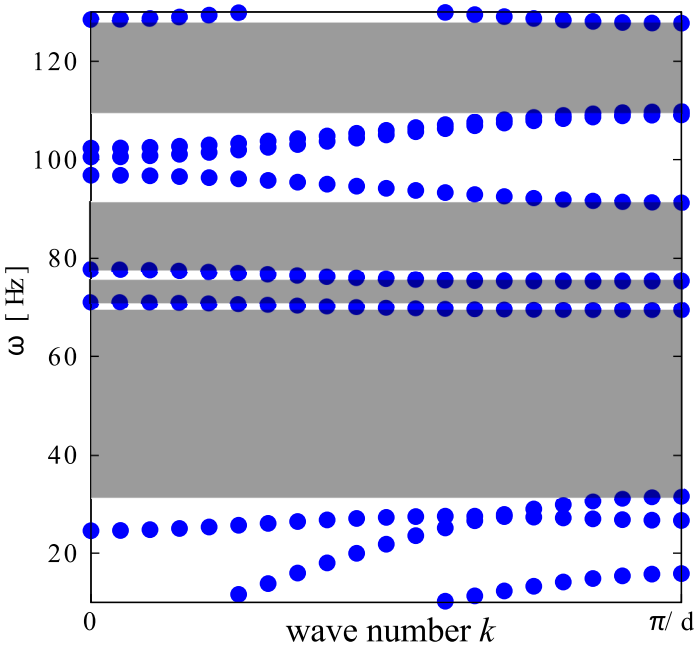

Figure 5.10: The band structure of the phononic crystal composed of alternative material layers shown in Fig. 5.10.

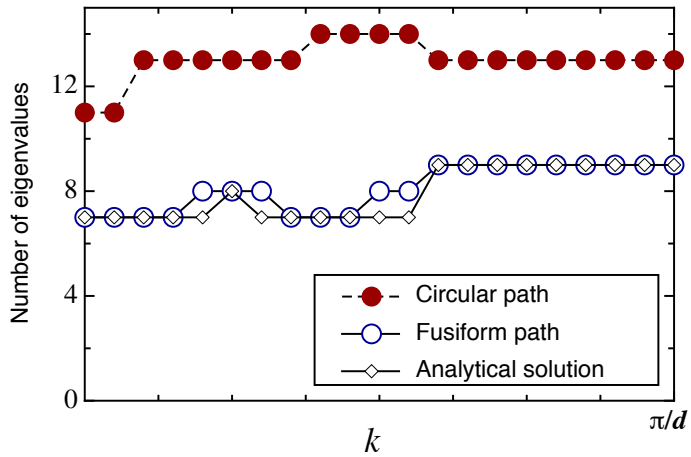

Figure 5.11: The number of eigenfrequencies obtained by the circular path and fusiform path.

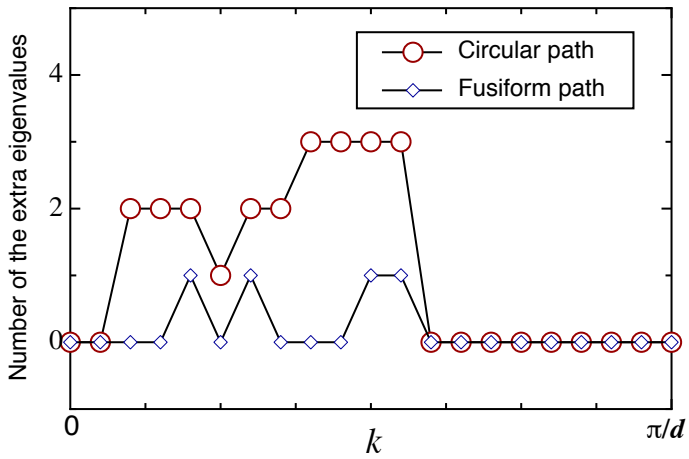

Figure 5.12: The number of extra eigenfrequencies outside the selected range obtained by the circular path and fusiform path .

Table 5.2: The material constants for the three-phase phononic structure

Material	Density [kg/m^3]	Young's modulus [Pa]	Poisson's ratio
1	$\bar{\rho}_1 = 2.0 \times 10^3$	$E_1 = 7.8 \times 10^5$	$\bar{\nu}_1 = 0.34$
2	$\bar{\rho}_2 = 1.6 \times 10^4$	$E_2 = 1.248 \times 10^8$	$\bar{\nu}_2 = 0.34$

analytical solution is found and it should be noted that the number of eigenfrequencies is one less than the analytical solution. The reason for the phenomenon is that the missing eigenvalue is located extremely close to the left corner points of the fusiform integration path. With the number of collocation points $N = 200$, the implicit filtered function evaluated numerically at the corner points does not extend outside the integration path but shrinks a little bit into the integration path.

5.4 Conclusion

The work is undertaken to apply the BEM to the analyses of elastic phononic structures. In the 2D elastodynamic problem, both longitudinal and transverse waves are considered in the calculations of band structures for the phononic crystals. The spurious eigenfrequencies , which are resulted by the BEM formulations applied to the multiple connected domains, in some cases, contain complex values. To avoid these complex eigenfrequencies, a fusiform integration path is propose and it excludes the complex eigenfrequencies with imaginary parts larger than a certain threshold from the enclosed domain. Three typical elastic phononic structures are given:

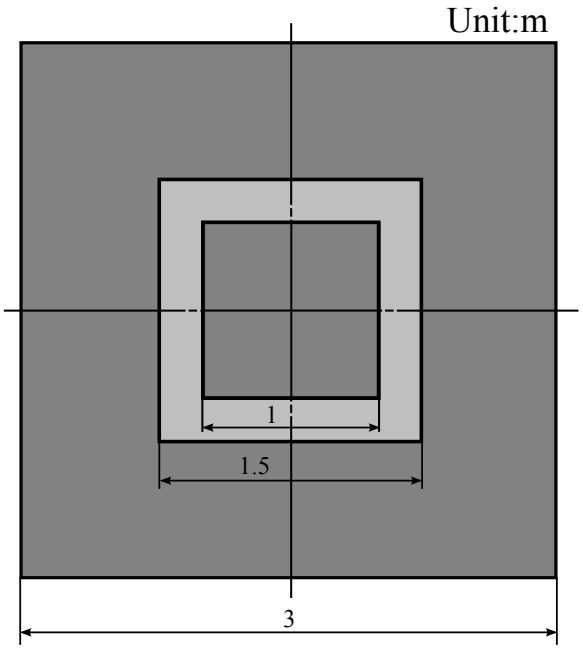

Figure 5.13: A unit cell with square shape inclusion coated with soft material (the bright gray denotes the material 1, the dark gray denotes the material 2).

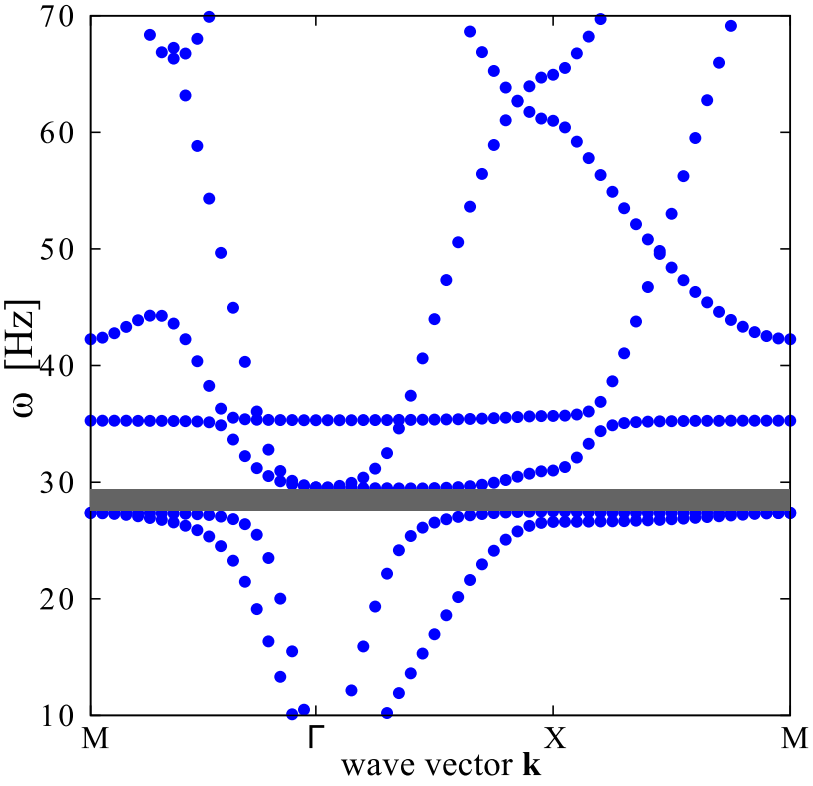

Figure 5.14: The band structure of the three-phase phononic structure.

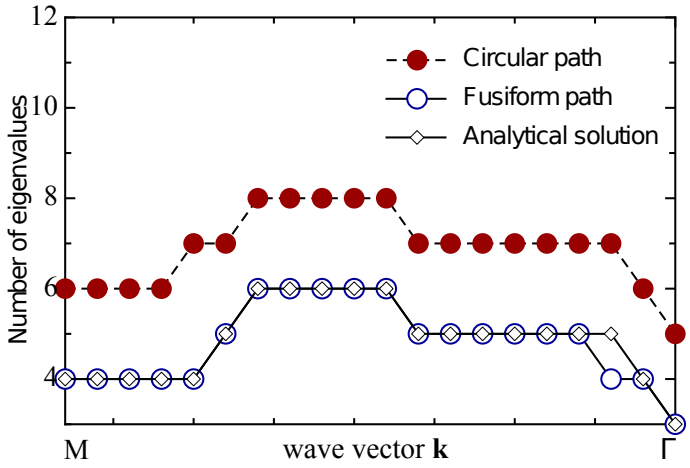

Figure 5.15: The number of eigenfrequencies obtained by the circular path and fusiform path.

- The two-phase phononic structure which has dense/stiff scatterers imbedded in light/soft host, presents a band gap based Bragg scattering.
- The unidirectional phononic periodic plate which has the unit cell with traction-free boundaries, presents flat bands.
- The phononic structure which has the imbedded dense/stiff scatterers coated with a light/soft material, presents a band gap.

The meaningful results demonstrate the effectiveness of the proposed methodology for the band calculation of the elastic phononic structures.

CHAPTER VI

Infinite/Finite Unidirectional Phononic Plates

6.1 Introduction

In practical problems, it is more appropriate to consider finite models than infinite ones of composite materials. Unlike the phononic crystals, the Bloch theorem is not applicable for the finite structures with periodic parts. Also they are different from the quasi-periodic situations whose solutions are converged. However, the finite structures with periodic parts present frequency-banded nature and exhibit a gap effect as well.

For an infinite 1D periodically layered media, the transfer matrix method is combined with Floquet's theorem to predict the dispersion curves across a specified frequency range [95, 96]. The investigation of the existence of band gaps in quasi-one-dimensional phononic plate with bounded unit cell is also reported [97]. A similar study is carried out by using the supercell plane wave method [98]. Research has also been conducted on periodic structures with finite layers [99, 100], in which the transfer matrix method is employed to predict the frequency-dependent transmission in a 1D finite periodic structure. Moreover, with the method of characteristics, propagation of waves in infinite and finite periodic structures are investigated [100]. The effects of the number of the layers for unit cells on the dynamics of a bounded structure are investigated by using FEM [101, 102]. A study of the finite elastic periodic materials and structures is presented with a perspective on both frequency and temporal domains in [103], in which the correlation between the dynamic response of the respective finite and infinite systems is discussed.

In previous chapters, the analyses of 2D acoustic/elastic phononic structures that related to the infinite problems are presented. In this chapter, the BEM is applied to the study of the transmission of waves in a finite structures with periodic parts which can be considered as phononic crystal plates. With the BEM, only the boundary is

discretized into line meshes in 2D problem. Furthermore, the matrices for the bounded unit cell is formulated and is used repeatedly according to the number of layers. With the proposed method, we derive a size-reduced system matrix in which quantities on the surfaces of phononic plate and the internal boundary of cells are removed. Moreover, we investigate the dispersion relation of the infinite structures by giving the periodic boundary condition to a unit cell. The nonlinear Bloch eigenvalue problem resulted by the BEM is solved by using the contour integral method. Both acoustic and elastic structures are investigated. For the acoustic phononic plate, the acoustic waves governed by the Helmholtz equations are considered and the cells have rigid boundaries. For elastic structures, longitudinal and transverse waves are considered, and a force free boundary condition is given on the surfaces of the phononic plates. Numerical simulations are performed and the correlation between the number of layers of the cells and the transmission is presented.

6.2 Formulations

The governing equations and boundary integral equations for acoustic and elastic problems have been introduced in the previous two chapters, therefore, we start from the derivation of the size reduced coefficient matrix for the finite unidirectional phononic structure.

6.2.1 Transfer matrix for the unit cell of a unidirectional phononic plate

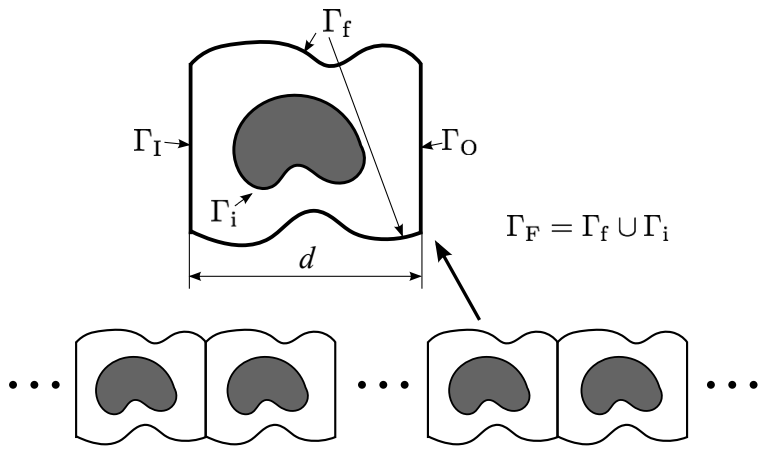

Figure 6.1: The boundary definition of the unit cell in a unidirectional phononic crystal plate.

Let us consider the unit cell of a unidirectional phononic structure shown in Fig. 6.1. The boundaries of the left and right interfaces of the unit cell is defined as Γ_{I} (input boundary) and Γ_{O} (output boundary), respectively. The rest of the boundaries of the unit cell including the internal boundary between different material domains, are defined as $\Gamma_{\mathrm{F}} = \Gamma_{\mathrm{f}} \cup \Gamma_{\mathrm{i}}$, where Γ_{f} is the traction-free boundary and Γ_{i} is the interface boundary between the matrix and inclusion.

By following the derivation of Eq. (5.12), a system of algebraic equations for the unit cell is obtained as follows:

$$\begin{pmatrix} \mathbf{H}_{\mathrm{II}} & \mathbf{H}_{\mathrm{IO}} & \mathbf{H}_{\mathrm{IF}} \\ \mathbf{H}_{\mathrm{OI}} & \mathbf{H}_{\mathrm{OO}} & \mathbf{H}_{\mathrm{OF}} \\ \mathbf{H}_{\mathrm{FI}} & \mathbf{H}_{\mathrm{FO}} & \mathbf{H}_{\mathrm{FF}} \end{pmatrix} \begin{pmatrix} \mathbf{U}_{\mathrm{I}} \\ \mathbf{U}_{\mathrm{O}} \\ \mathbf{U}_{\mathrm{F}} \end{pmatrix} = \begin{pmatrix} \mathbf{G}_{\mathrm{II}} & \mathbf{G}_{\mathrm{IO}} & \mathbf{G}_{\mathrm{IF}} \\ \mathbf{G}_{\mathrm{OI}} & \mathbf{G}_{\mathrm{OO}} & \mathbf{G}_{\mathrm{OF}} \\ \mathbf{G}_{\mathrm{FI}} & \mathbf{G}_{\mathrm{FO}} & \mathbf{G}_{\mathrm{FF}} \end{pmatrix} \begin{pmatrix} \mathbf{T}_{\mathrm{I}} \\ \mathbf{T}_{\mathrm{O}} \\ \mathbf{T}_{\mathrm{F}} \end{pmatrix}. \tag{6.1}$$

where $(\cdot)_{\mathrm{I}}$, $(\cdot)_{\mathrm{O}}$, and $(\cdot)_{\mathrm{F}}$ denote the quantities on the boundaries Γ_{I}, Γ_{O} and Γ_{F}, respectively.

Substituting the boundary conditions on Γ_{F} to Eq. (6.1) and moving the unknown quantities to the left hand side, we have

$$\begin{pmatrix} \mathbf{H}_{\mathrm{II}} & \mathbf{H}_{\mathrm{IO}} & \mathbf{A}_{\mathrm{IF}} \\ \mathbf{H}_{\mathrm{OI}} & \mathbf{H}_{\mathrm{OO}} & \mathbf{A}_{\mathrm{OF}} \\ \mathbf{H}_{\mathrm{FI}} & \mathbf{H}_{\mathrm{FO}} & \mathbf{A}_{\mathrm{FF}} \end{pmatrix} \begin{pmatrix} \mathbf{U}_{\mathrm{I}} \\ \mathbf{U}_{\mathrm{O}} \\ \mathbf{X}_{\mathrm{F}} \end{pmatrix} = \begin{pmatrix} \mathbf{G}_{\mathrm{II}} & \mathbf{G}_{\mathrm{IO}} & \mathbf{B}_{\mathrm{IF}} \\ \mathbf{G}_{\mathrm{OI}} & \mathbf{G}_{\mathrm{OO}} & \mathbf{B}_{\mathrm{OF}} \\ \mathbf{G}_{\mathrm{FI}} & \mathbf{G}_{\mathrm{FO}} & \mathbf{B}_{\mathrm{FF}} \end{pmatrix} \begin{pmatrix} \mathbf{T}_{\mathrm{I}} \\ \mathbf{T}_{\mathrm{O}} \\ \mathbf{Y}_{\mathrm{F}} \end{pmatrix}. \tag{6.2}$$

where $\mathbf{X}_{\mathrm{F}}$ and $\mathbf{Y}_{\mathrm{F}}$ contain the unknown quantities and known quantities on Γ_{F}, respectively.

Let $\mathbf{X}_{\mathrm{F}}$ be represented by the remaining quantities:

$$\begin{aligned} \mathbf{X}_{\mathrm{F}} = &-\mathbf{A}_{\mathrm{FF}}^{-1}\mathbf{H}_{\mathrm{FI}}\mathbf{U}_{\mathrm{I}} - \mathbf{A}_{\mathrm{FF}}^{-1}\mathbf{H}_{\mathrm{FO}}\mathbf{U}_{\mathrm{O}} \\ &+ \mathbf{A}_{\mathrm{FF}}^{-1}\mathbf{G}_{\mathrm{FI}}\mathbf{T}_{\mathrm{I}} + \mathbf{A}_{\mathrm{FF}}^{-1}\mathbf{G}_{\mathrm{FO}}\mathbf{T}_{\mathrm{O}} + \mathbf{A}_{\mathrm{FF}}^{-1}\mathbf{B}_{\mathrm{FF}}\mathbf{Y}_{\mathrm{F}}. \end{aligned}$$

Then, unknowns in Eq. (6.2) can now be represented by quantities only of Γ_{I} and

Γ_{O}:

$$\begin{aligned}
&\begin{pmatrix} \mathbf{H}_{\mathrm{IO}} - \mathbf{A}_{\mathrm{IF}}\mathbf{A}_{\mathrm{FF}}^{-1}\mathbf{H}_{\mathrm{FO}} & -\mathbf{G}_{\mathrm{IO}} + \mathbf{A}_{\mathrm{IF}}\mathbf{A}_{\mathrm{FF}}^{-1}\mathbf{G}_{\mathrm{FO}} \\ \mathbf{H}_{\mathrm{OO}} - \mathbf{A}_{\mathrm{OF}}\mathbf{A}_{\mathrm{FF}}^{-1}\mathbf{H}_{\mathrm{FO}} & -\mathbf{G}_{\mathrm{OO}} + \mathbf{A}_{\mathrm{OF}}\mathbf{A}_{\mathrm{FF}}^{-1}\mathbf{G}_{\mathrm{FO}} \end{pmatrix} \begin{pmatrix} \mathbf{U}_{\mathrm{O}} \\ \mathbf{T}_{\mathrm{O}} \end{pmatrix} \\
&= \begin{pmatrix} -\mathbf{H}_{\mathrm{II}} + \mathbf{A}_{\mathrm{IF}}\mathbf{A}_{\mathrm{FF}}^{-1}\mathbf{H}_{\mathrm{FI}} & \mathbf{G}_{\mathrm{II}} - \mathbf{A}_{\mathrm{IF}}\mathbf{A}_{\mathrm{FF}}^{-1}\mathbf{G}_{\mathrm{FI}} \\ -\mathbf{H}_{\mathrm{OI}} + \mathbf{A}_{\mathrm{OF}}\mathbf{A}_{\mathrm{FF}}^{-1}\mathbf{H}_{\mathrm{FI}} & \mathbf{G}_{\mathrm{OI}} - \mathbf{A}_{\mathrm{OF}}\mathbf{A}_{\mathrm{FF}}^{-1}\mathbf{G}_{\mathrm{FI}} \end{pmatrix} \begin{pmatrix} \mathbf{U}_{\mathrm{I}} \\ \mathbf{T}_{\mathrm{I}} \end{pmatrix} \\
&+ \begin{pmatrix} \mathbf{B}_{\mathrm{IF}} - \mathbf{A}_{\mathrm{IF}}\mathbf{A}_{\mathrm{FF}}^{-1}\mathbf{B}_{\mathrm{FF}} \\ \mathbf{B}_{\mathrm{OF}} - \mathbf{A}_{\mathrm{OF}}\mathbf{A}_{\mathrm{FF}}^{-1}\mathbf{B}_{\mathrm{FF}} \end{pmatrix} \begin{pmatrix} \mathbf{Y}_{\mathrm{F}} \end{pmatrix}.
\end{aligned} \tag{6.3}$$

For each periodic cell, Eq. (6.3) can be obtained, therefore, we can write Eq. (6.3) in a more general form:

$$\mathbf{M}\mathbf{X}^{l+1} = \mathbf{N}\mathbf{X}^{l} + \mathbf{L}\mathbf{Y}_{\mathrm{F}}, \tag{6.4}$$

where $\mathbf{X}^{l+1}$ and $\mathbf{X}^{l}$ are the vectors that contain the quantities on Γ_{O} and Γ_{I}, respectively.

6.2.2 Size-reduced system matrix

Let us consider a finite structure comprising the input domain Ω_{I}, the output domain Ω_{O}, and the finite layers of the periodic structures as shown in Fig. 6.2. The input domain's boundary that is shared with the periodic part is defined as Γ_{O}^{1}, and the remaining boundary of the input domain is defined as Γ_{L}. The output domain's boundary that is shared with the periodic part is defined as Γ_{I}^{n}, and the remaining boundary of the output domain is defined as Γ_{R}.

Also for domains Ω_{I} and Ω_{O}, the system of algebraic equations can be also formulated, as follows:

$$\mathbf{A}_{\mathrm{L}}\mathbf{X}^{\mathrm{L}} + \mathbf{A}_{\mathrm{L1}}\mathbf{X}^{1} = \mathbf{Y}^{\mathrm{L}}, \tag{6.5}$$

$$\mathbf{A}_{\mathrm{R}n}\mathbf{X}^{n} + \mathbf{A}_{\mathrm{R}}\mathbf{X}^{\mathrm{R}} = \mathbf{Y}^{\mathrm{R}}, \tag{6.6}$$

where $\mathbf{X}^{\mathrm{L}}$, $\mathbf{X}^{\mathrm{R}}$, $\mathbf{X}^{1}$, and $\mathbf{X}^{n}$ are the vectors that contain the known quantities on the boundary $\Gamma_{\mathbf{L}}$, $\Gamma_{\mathbf{R}}$, $\Gamma_{\mathbf{O}}^{1}$, $\Gamma_{\mathbf{I}}^{n}$, respectively.

Let the number of layers for the periodic part $N_{\mathrm{L}} = n-1$. By combining Eqs. (6.4), (6.5) and (6.6), we have the system of algebraic equations for the whole structure, as

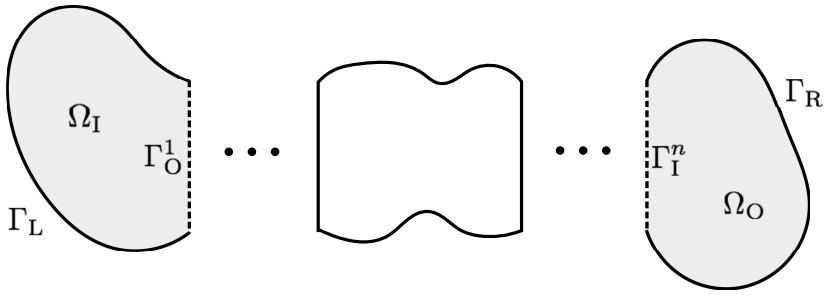

Figure 6.2: The definition of the boundaries of input and output domain of a finite structure.

follows:

$$\begin{pmatrix} \mathbf{A}_{\mathrm{L}} & \mathbf{A}_{\mathrm{L}1} & 0 & 0 & 0 & 0 & 0 \\ 0 & -\mathbf{N} & \mathbf{M} & 0 & 0 & 0 & 0 \\ 0 & 0 & -\mathbf{N} & \mathbf{M} & 0 & 0 & 0 \\ 0 & 0 & 0 & \ddots & \ddots & 0 & 0 \\ 0 & 0 & 0 & 0 & -\mathbf{N} & \mathbf{M} & 0 \\ 0 & 0 & 0 & 0 & 0 & \mathbf{A}_{\mathrm{R}n} & \mathbf{A}_{\mathrm{R}} \end{pmatrix} \begin{pmatrix} \mathbf{X}^{\mathrm{L}} \\ \mathbf{X}^{1} \\ \mathbf{X}^{2} \\ \vdots \\ \mathbf{X}^{n} \\ \mathbf{X}^{\mathrm{R}} \end{pmatrix} = \begin{pmatrix} \mathbf{Y}^{\mathrm{L}} \\ \mathbf{L}\mathbf{Y}_{\mathrm{F}} \\ \mathbf{L}\mathbf{Y}_{\mathrm{F}} \\ \vdots \\ \mathbf{L}\mathbf{Y}_{\mathrm{F}} \\ \mathbf{Y}^{\mathrm{R}} \end{pmatrix}. \tag{6.7}$$

Let n_{F} and n_{IO} be the numbers of elements for boundary Γ_{F} and Γ_{I} (or Γ_{O}) of a unit cell, respectively. There are two material collocation cases for the periodic part: one is that the materials are different at the connection interfaces between adjacent cells; the other one is that the same materials are used across the interfaces between adjacent cells. For the former case, the boundary at the interfaces between the adjacent cells are the real one, and it can be seen that the dimension of the system equation for the structure in Fig. 6.2 is reduced by $n_{\mathrm{F}}N_{\mathrm{L}}$ by employing Eq. (6.7). For the latter case, obviously, the interfaces between adjacent cells are virtual ones, so the reduction of the dimension of system marix becomes $N_{\mathrm{L}}(n_{\mathrm{F}} - n_{\mathrm{IO}}) + n_{\mathrm{IO}}$. Usually, for a complicated structured unit cell consisting of plural materials, we have $n_{\mathrm{F}} > n_{\mathrm{IO}}$.

6.2.3 Bloch eigenvalue problem for infinite phononic structures

Let us return to the unit cell depicted in Fig. 6.1. For infinite periodic structures, the Bloch theorem makes the following relation hold:

$$\mathbf{U}_{\mathrm{O}} = \mathbf{U}_{\mathrm{I}} \exp(\mathrm{i}kd), \tag{6.8}$$

$$\mathbf{T}_{\mathrm{O}} = \mathbf{T}_{\mathrm{I}}(-\exp(\mathrm{i}kd)), \tag{6.9}$$

where k is the wave number, d is the lattice vector, and for 1D phononic periodic structures, d becomes a scalar as the length of a unit cell. Since the outward normal directions at Γ_{I} and Γ_{O} are opposite to each other, a minus sign is needed in Eq. (6.9).

One can write Eq. (6.1) in another form as follows:

$$\begin{bmatrix} \mathbf{H}_{\mathrm{I}} & \mathbf{H}_{\mathrm{O}} & \mathbf{H}_{\mathrm{F}} \end{bmatrix} \begin{bmatrix} \mathbf{U}_{\mathrm{I}} \\ \mathbf{U}_{\mathrm{O}} \\ \mathbf{U}_{\mathrm{F}} \end{bmatrix} = \begin{bmatrix} \mathbf{G}_{\mathrm{I}} & \mathbf{G}_{\mathrm{O}} & \mathbf{G}_{\mathrm{F}} \end{bmatrix} \begin{bmatrix} \mathbf{T}_{\mathrm{I}} \\ \mathbf{T}_{\mathrm{O}} \\ \mathbf{T}_{\mathrm{F}} \end{bmatrix}. \tag{6.10}$$

Applying the periodic boundary condition in Eqs. (6.8) and (6.9), and homogeneous boundary condition to Eq. (6.10), a nonlinear eigenvalue problem is obtained as follows:

$$\begin{bmatrix} \mathbf{H}_{\mathrm{I}} + \mathbf{H}_{\mathrm{O}} \exp \mathrm{i}kd & -(\mathbf{G}_{\mathrm{I}} - \mathbf{G}_{\mathrm{O}} \exp \mathrm{i}kd) & \mathbf{A}_{\mathrm{F}} \end{bmatrix} \begin{bmatrix} \mathbf{U}_{\mathrm{I}} \\ \mathbf{T}_{\mathrm{I}} \\ \mathbf{X}_{\mathrm{F}} \end{bmatrix} = \mathbf{0}, \tag{6.11}$$

where the eigenvalue parameter ω is involved in each element of the coefficient matrix nonlinearly. Let Eq. (6.11) be represented in a compact form:

$$\mathbf{F}(\omega, k)\mathbf{X} = \mathbf{0}. \tag{6.12}$$

For unidirectional phononic structure, k is set to vary from 0 to π/d, and the dispersion curves can be obtained by solving eigenvalues ω determined by Eq. (6.12).

6.3 Numerical examples

6.3.1 Acoustic unidirectional phononic plate

A finite structure having periodic parts is depicted in Fig.6.3. Square input and output domains are connected by N_L layers of square cells with rigid cylinder scatters, and all sides of the square structures are assumed to be 1[m]. The parameters of the example are defined as: the sound velocity is 337 [m/s]; the density is 1.22 [kg/m^3]; the filling fraction is 0.503; the length of cell is 1 [m]. A nonsymmetrical excitation is given as the particle velocity $v = 1$[m/s] on 70% of the edge of the input domain, while in the output domain, 30 observation points are distributed. The points from number 1 to 10, 11 to 20 and 21 to 30 have the same y coordinates as $y = 0.5$,

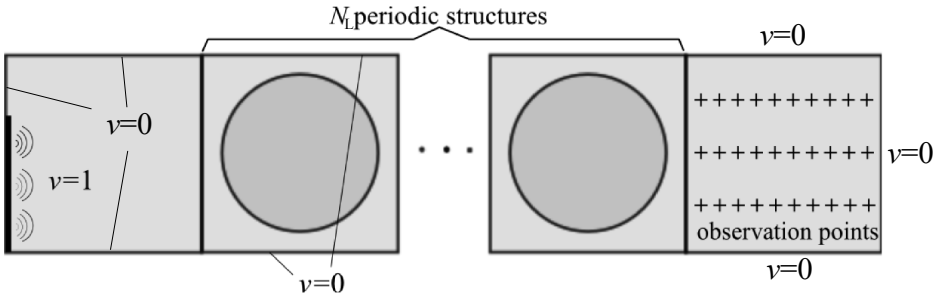

Figure 6.3: Input and output domains connected by square cells. The cross symbols denote the observation points.

$y = 0.25$, $y = 0.75$ respectively, while x coordinates for the each 10 points are 0.05, 0.15, $\cdots$, 0.95, and unit is [m]. Assuming that the unit cell is one layer of an infinite one directional periodic structure and solving the nonlinear eigenvalue problem given by Eq.(6.12) using the BEM based on Burton-Miller's method, the band structure is obtained. For the Block SS method, solved range is assumed as [500, 4500]. The numerical results for the dispersion curves obtained by the conventional BEM and that based on Burton-Miller's method are shown in Figs. 6.4 and 6.5, respectively. Since the spurious eigenvalues are constants when the wave number k varies from 0 to π, there are horizontal lines showing spurious eigenvalues in Fig. 6.4.

Next, let us consider the transmission problem and use different models by changing the layers of the connection parts. The transmissivities of the finite periodic structure with 12, 25, 50, 100 layers are shown in Figs.6.6 to 6.9, in which the sound pressures at 30 observation points are plotted, and in Figs.6.6(b) to 6.9(b) are shown their projections on ω-p plane. From the figures of transmissivity, it is found that the transmissivity becomes very low in the band gaps particularly when the number of the layers is larger than 25.

To obtain the band gaps of the finite structure, the block SS method is directly applied to compute the eigenfrequencies of the size-reduced system matrix Eq. (6.7) that is also of a nonlinear eigenvalue problem. The eigenfrequencies of models with 12, 25, 50, 100 layers are shown in Figs. 6.10 to 6.13, respectively, corresponding to the solved range [500,1500] in which 1 band gap is included. Eigenfrequencies out of this range are also obtained. From these numerical results, it is found that the distribution of the eigenvalues along the real-axis have the band gap shown in Fig. 6.5. However, as is found in Figs. 6.10 to 6.13, two eigenfrequencies 1252.513 and 1262.504 are always found in the range of band gap. These eigenfrequencies do not change even when the number of layers is increased, hence the two eigenfrequencies

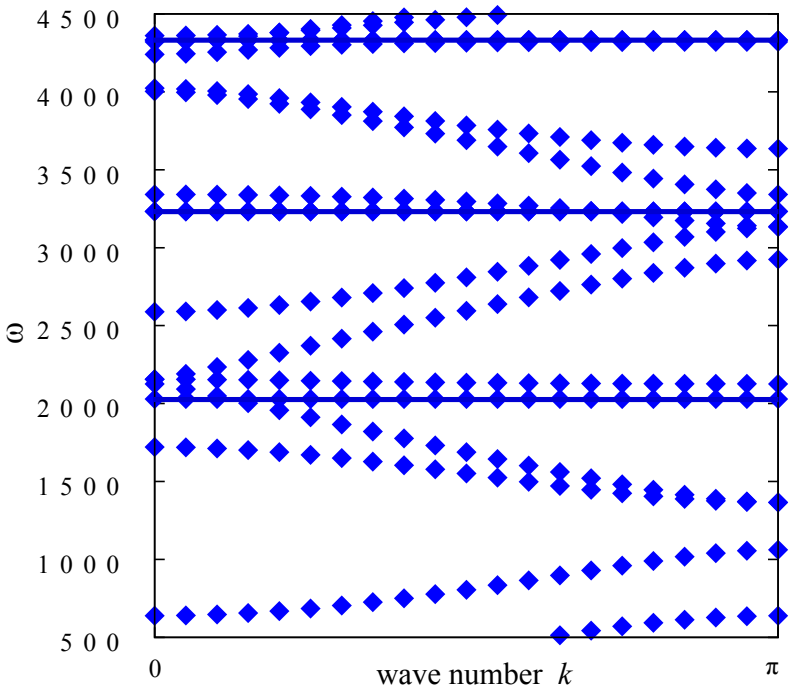

Figure 6.4: Dispersion curves (by conventional BEM) with spurious eigenvalues (horizontal lines).

can be considered as those corresponding to eigenmodes which have large amplitude in input and output domains while small amplitude in connection part.

6.3.2 Elastic unidirectional phononic plates

6.3.2.1 Example 1

A unit cell composed of alternating layers of two different materials is shown in Fig. 6.14, where the domain shown in black color corresponds to a stiff and dense material (denoted by subscript '2'), while the domain shown in white color corresponds to a compliant and light material (denoted by subscript '1'). The material constants are shown in Table 6.1.

Table 6.1: The material constants

Material	Density [kg/m^3]	Young's modulus [Pa]	Poisson's ratio
1	$\rho_1 = 2.0 \times 10^3$	$E_1 = 7.8 \times 10^6$	$\nu_1 = 0.34$
2	$\rho_2 = 1.6 \times 10^4$	$E_2 = 1.248 \times 10^8$	$\nu_2 = 0.34$

The unit cell proposed in this example has different materials at the two sides of

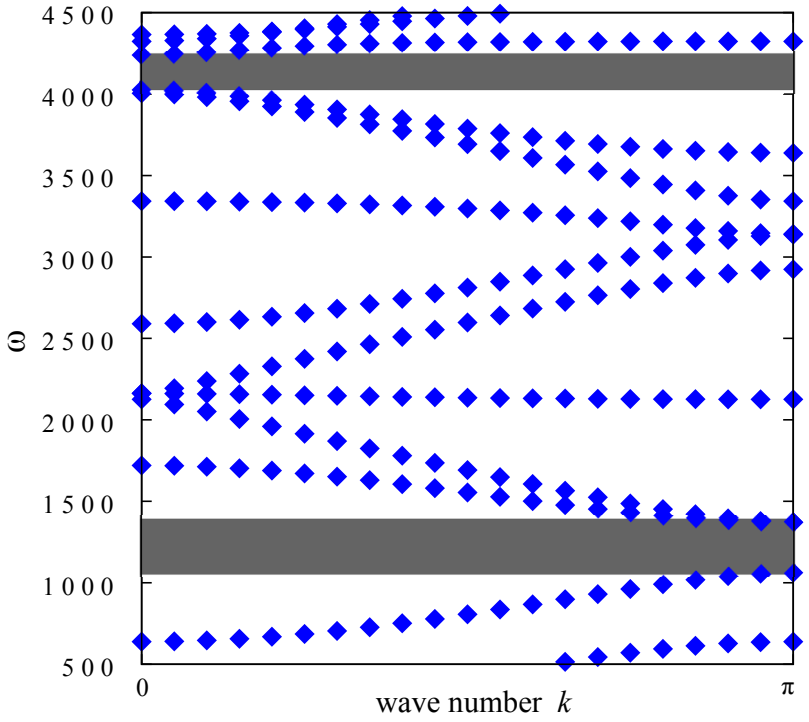

Figure 6.5: Dispersion curves (by the Burton-Miller method) and band gaps (shade).

the interfaces of the adjacent cells. This means that the reduced dimension of the system matrix is $n_{\mathrm{F}} N_{\mathrm{L}}$.

The finite structure composed of the input domain, the output domain and N_L layers of cells is depicted in Fig. 6.15, where an excitation $\bar{\mathbf{T}} = (1.0, 0.0)$ [N/m] is given on the left side boundary of the leftmost square domain in gray color which is considered as the input domain, and a roller support condition is specified on the right side boundary of the rightmost square in gray color which is considered as the output domain. The traction-free boundary condition is specified on the remaining part of the boundaries. The materials of the input and output domains are assumed as material 2. Moreover, 30 observation points (cross symbols) are chosen in the output domain. With the assumption that the left bottom corner point of the output domain is the origin of the coordinate system, the coordinates of the observation points numbered $1 \sim 10$ are $(0.1, 1)$, $(0.3, 1)$, ..., $(1.9, 1)$, points $11 \sim 20$ are $(0.1, 0.5)$, $(0.3, 0.5)$, ..., $(1.9, 0.5)$, and points $21 \sim 30$ are $(0.1, 1.5)$, $(0.3, 1.5)$, ..., $(1.9, 1.5)$.

Let us see first the band structure shown by the dispersion curves in Fig. 6.16, where the circular frequency range is chosen as $10 \sim 90$ [Hz]. It should be noted that the band structure is determined by a infinite system with the unit cell shown in Fig.

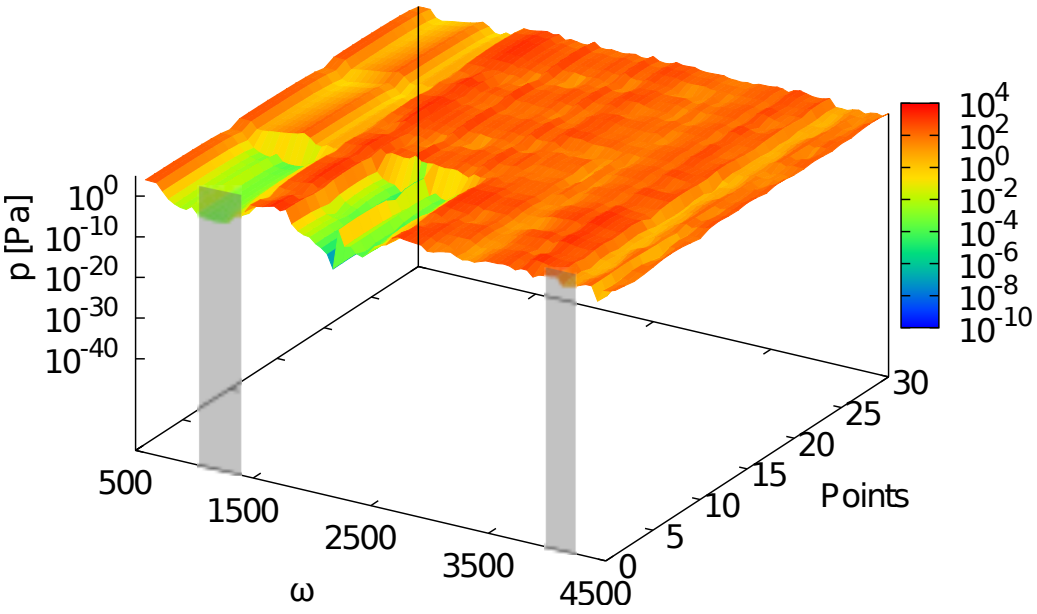

(a)

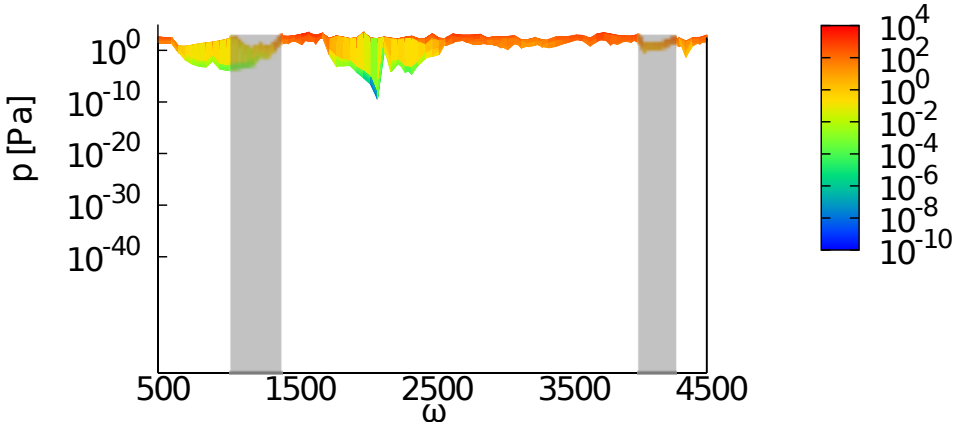

(b)

Figure 6.6: Transmissivity of finite periodic structure with 12 layers.

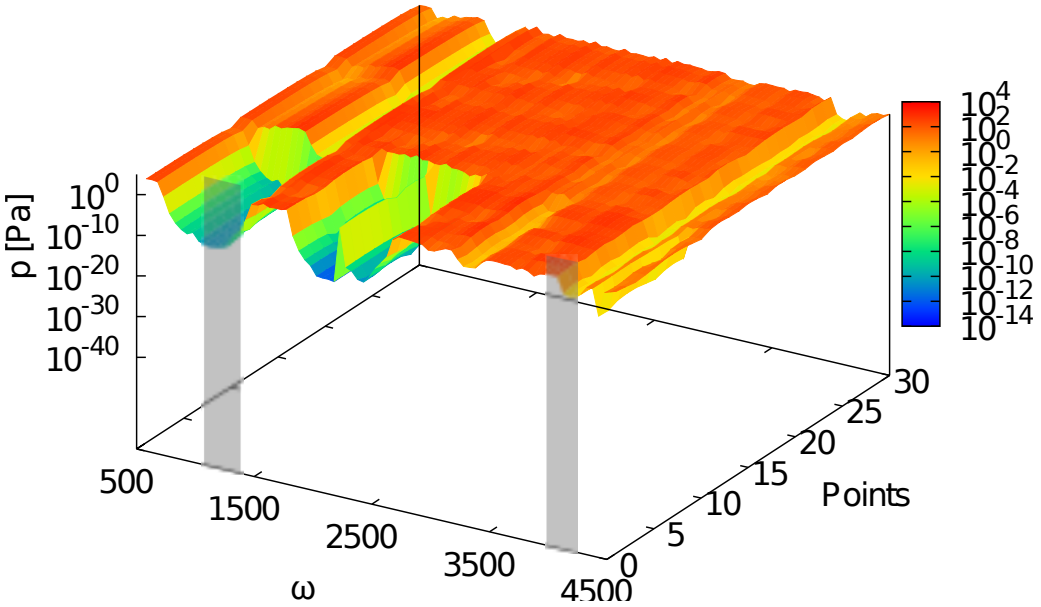

(a)

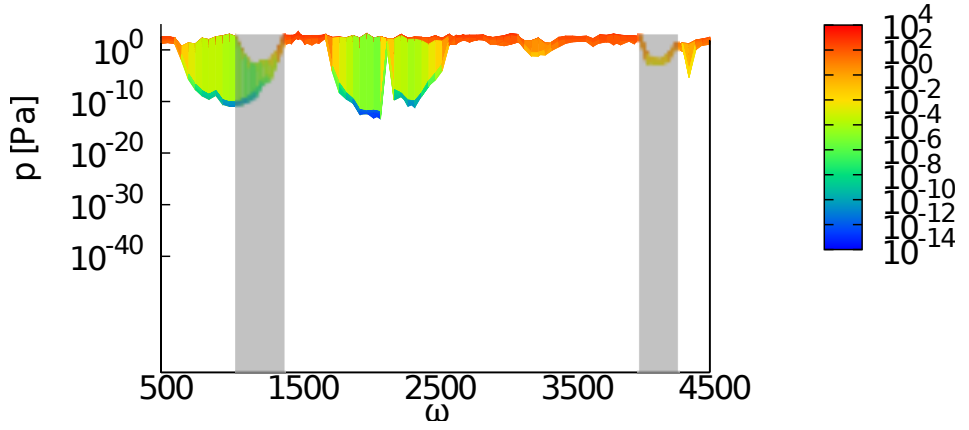

(b)

Figure 6.7: Transmissivity of finite periodic structure with 25 layers.

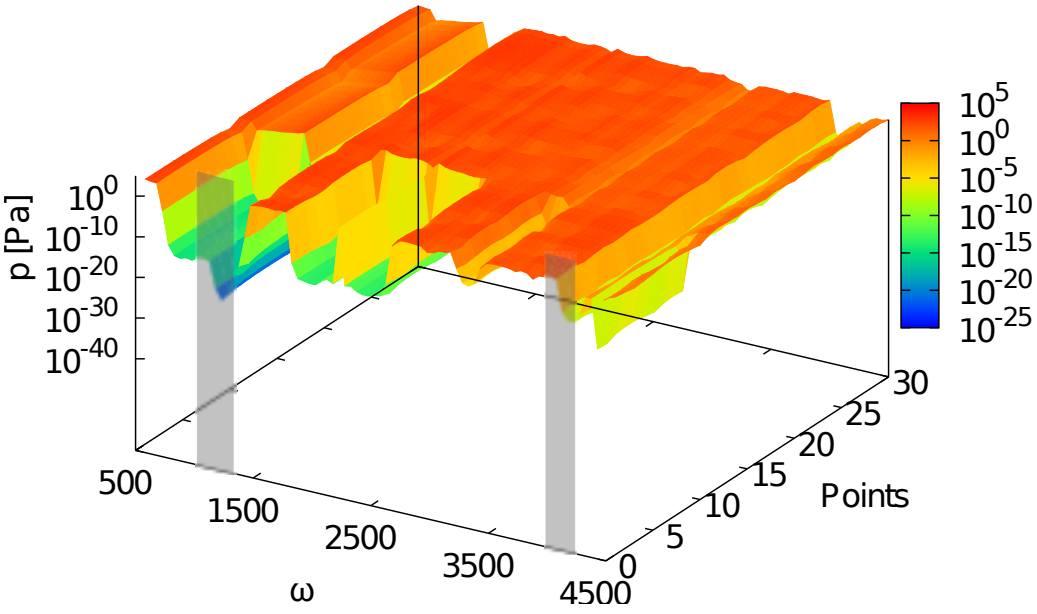

(a)

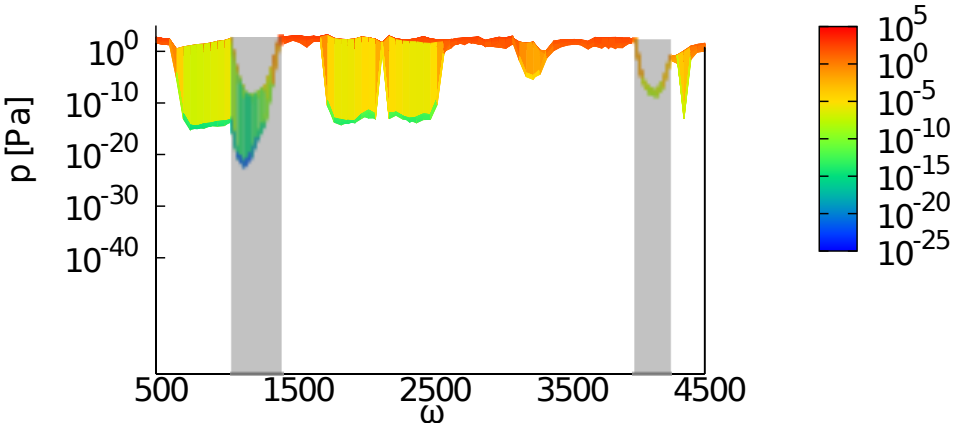

(b)

Figure 6.8: Transmissivity of finite periodic structure with 50 layers.

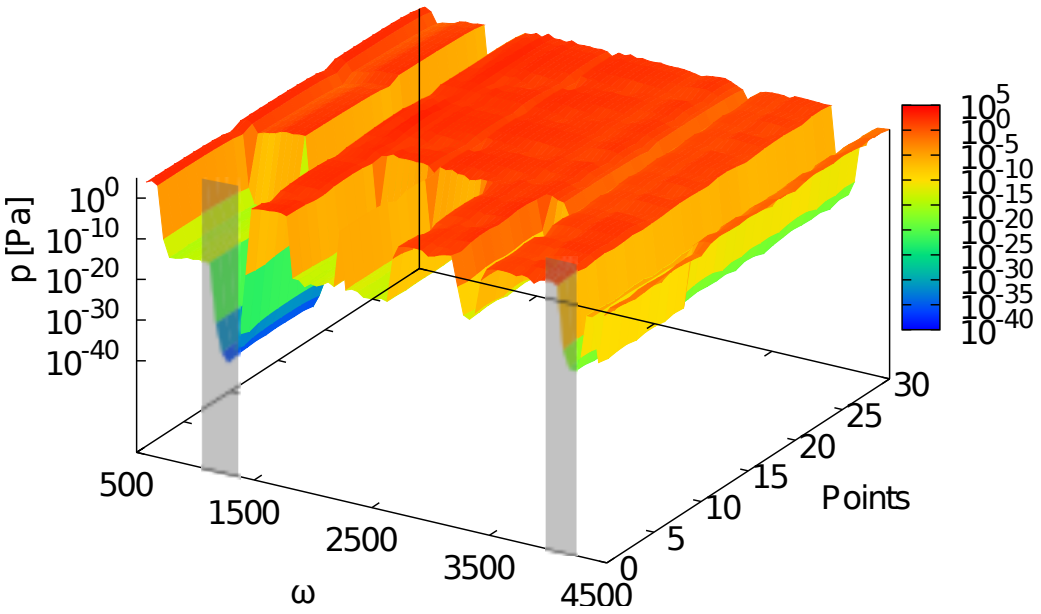

(a)

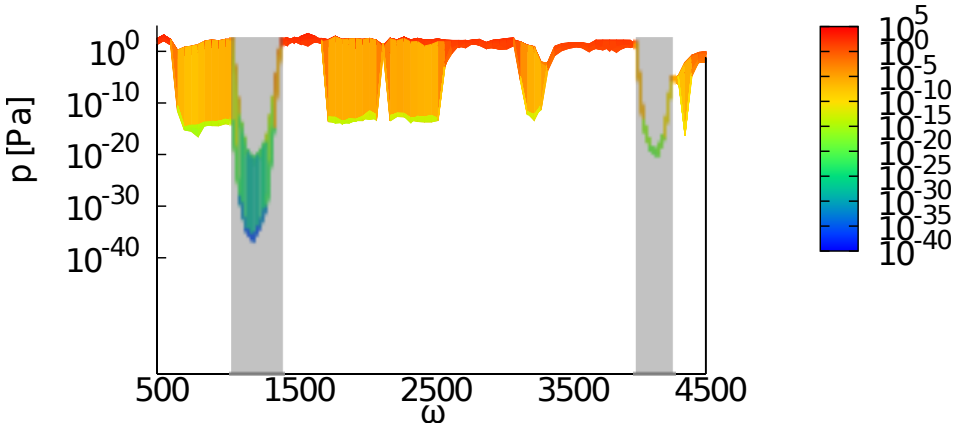

(b)

Figure 6.9: Transmissivity of finite periodic structure with 100 layers.

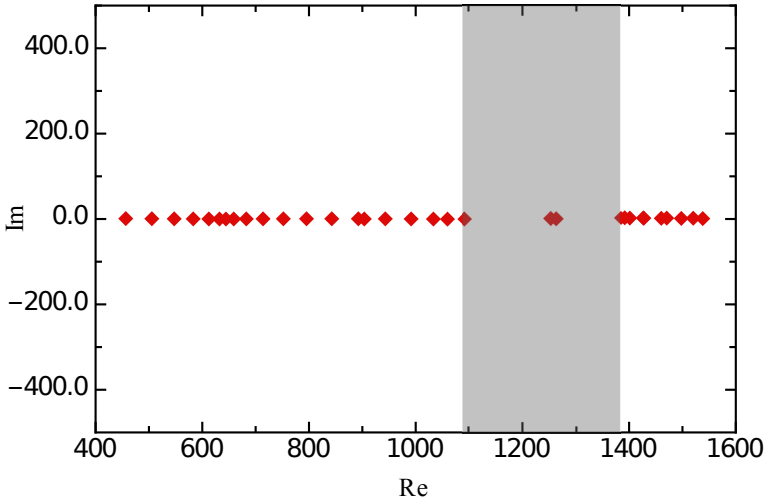

Figure 6.10: Eigenfrequencies of finite periodic structure with 12 layers.

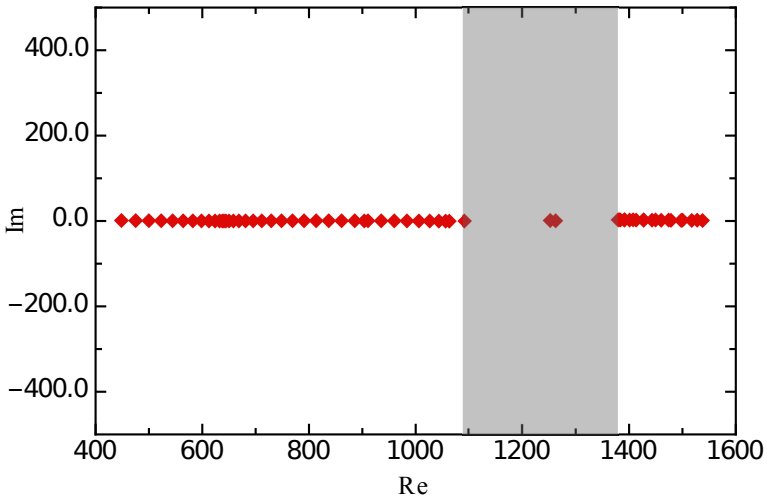

Figure 6.11: Eigenfrequencies of finite periodic structure with 25 layers.

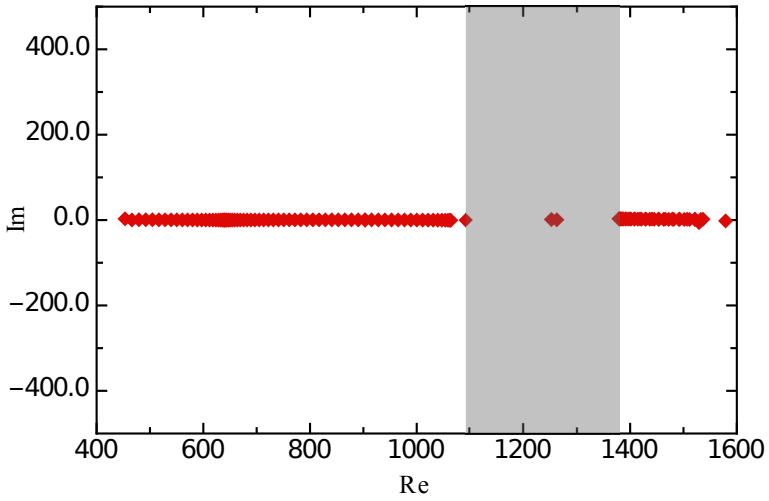

Figure 6.12: Eigenfrequencies of finite periodic structure with 50 layers.

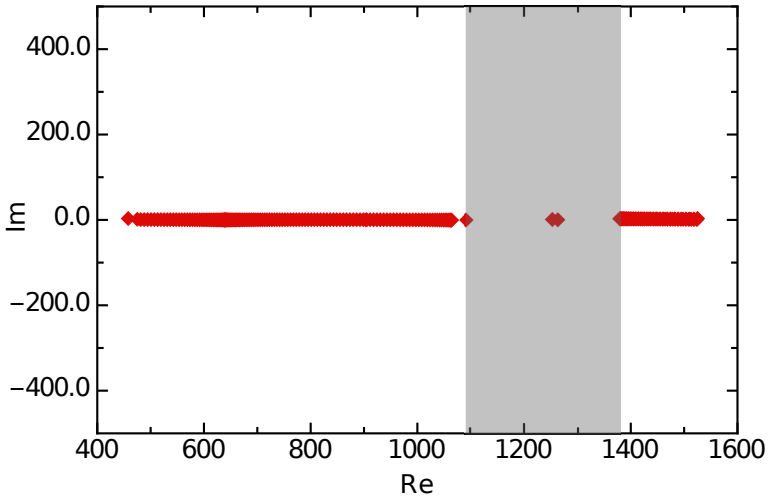

Figure 6.13: Eigenfrequencies of finite periodic structure with 100 layers.

6.14. Here, only two band gaps represented by the shaded ranges are considered.

For the finite structure, the displacement response $|\mathbf{U}| = \sqrt{U_x^2 + U_y^2}$ of the observation points of the output domain with different numbers of layers 10, 20, 30, 40 and their projections to ω-$|\mathbf{U}|$ plane are plotted in Fig. 6.17 to Fig. 6.20. It can be seen that the displacement transmitting to the output domain becomes smaller in accordance with the increase in the number of layers.

To obtain a more elaborate illustration of the correlation between transmission and number of layers, we choose 4 points in the frequency domain: 15, 30, 40, and 60 [Hz], in which 15 and 40 [Hz] are located in the pass band while 30, 60 [Hz] are located in the stop band. In Figs. 6.21 and 6.22, the transmissions of displacement $|\mathbf{U}|$ corresponding to the frequencies located in the pass band are presented, in which a small decrease in the transmission at frequency 40 [Hz] in the pass band can be observed. In Figs. 6.23 and 6.24, transmissions corresponding to the frequencies located in the stop bands are shown. The reduction of the displacement transmission is found not only in the former case, but also occurs in the pass band. Furthermore, the reduction of the transmission in stop bands is much faster than that in the pass bands.

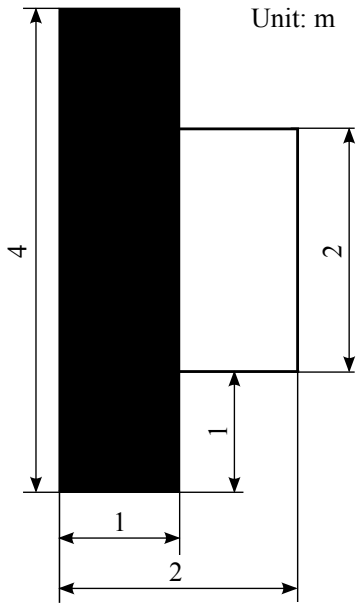

Figure 6.14: The unit cell (the stiff/dense material phase is shown in black and the compliant/light material phase is shown in white).

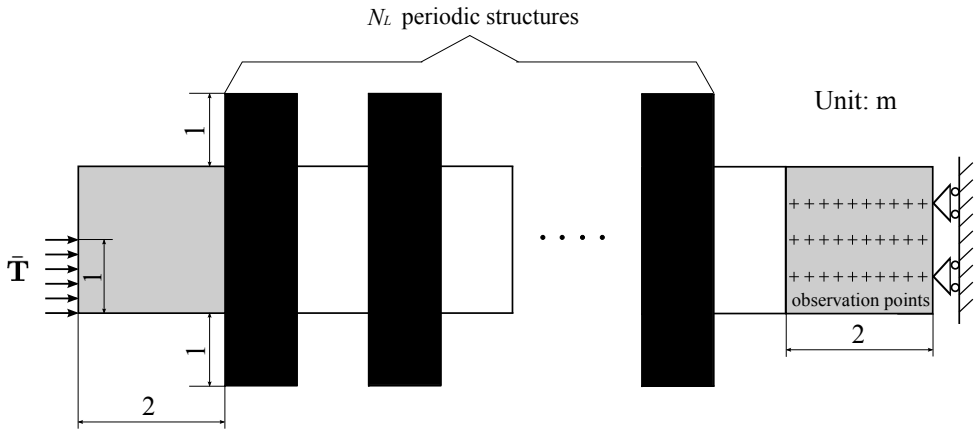

Figure 6.15: Two square domains connected (input domain is the left square domain in gray and output domain is the right square domain in gray) by N_L layers of cells in example 1 and the cross symbols denote the observation points.

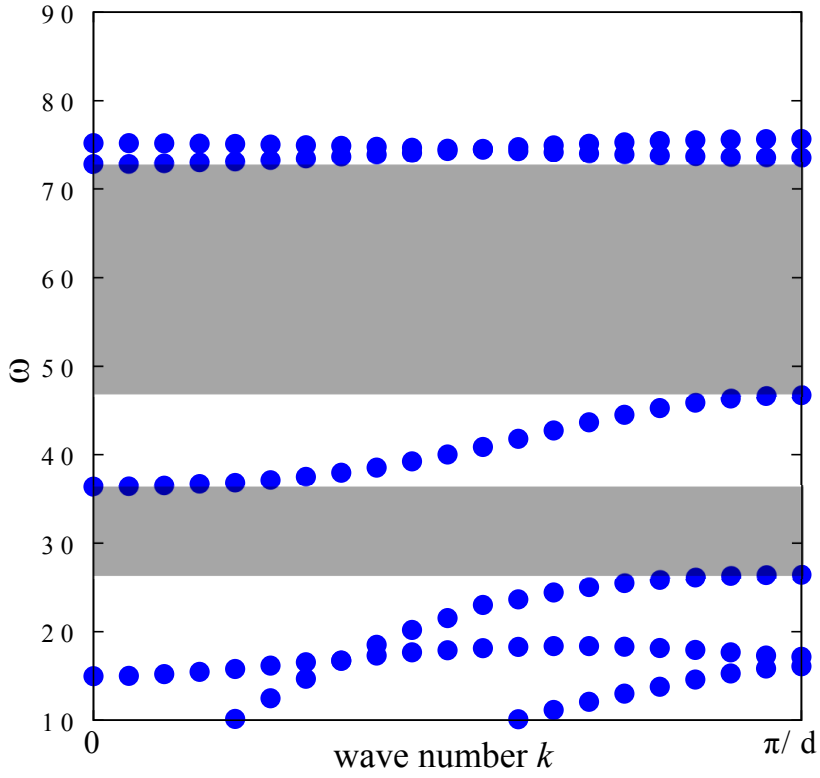

Figure 6.16: The band structure for the infinite structure (shade ranges denote the concerned band gaps).

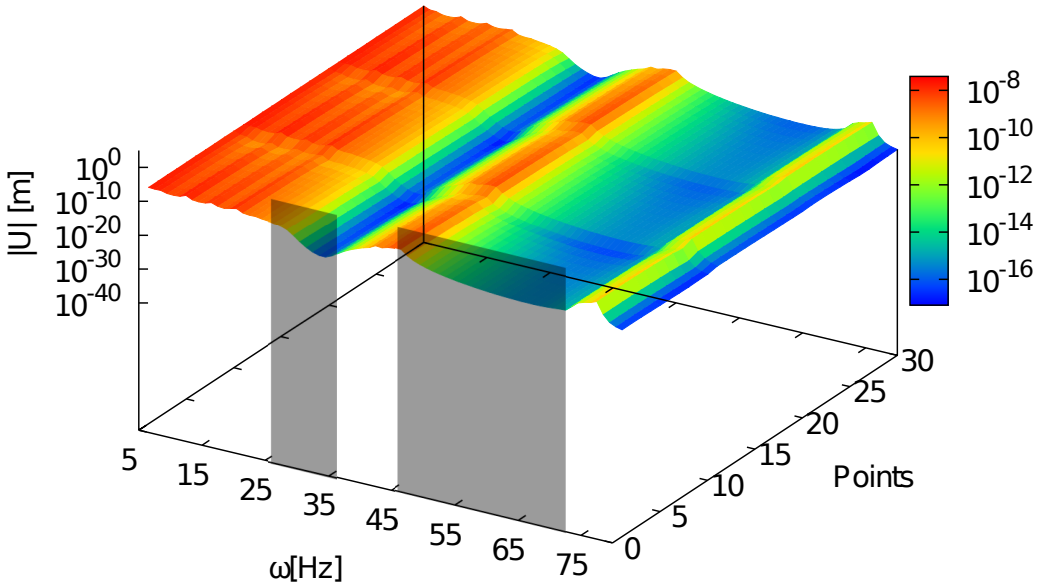

(a)

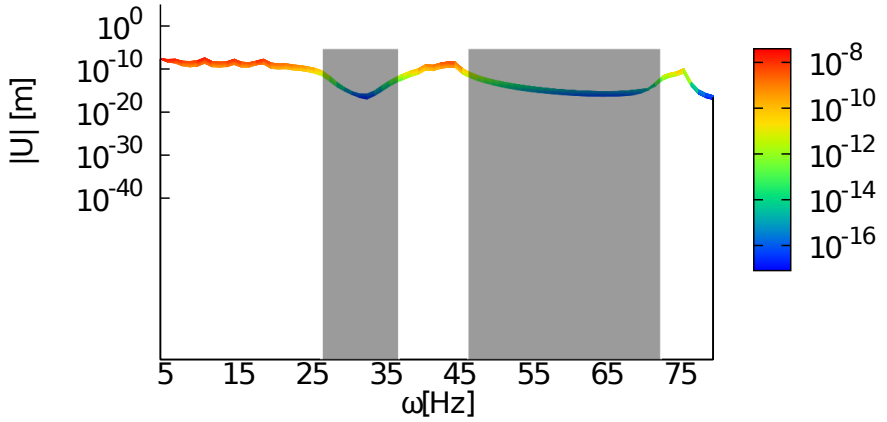

(b)

Figure 6.17: The transmission of $|\mathbf{U}|$ of 10-Layer sturcture ((a)) and the projection to ω-$|\mathbf{U}|$ plane ((b)).

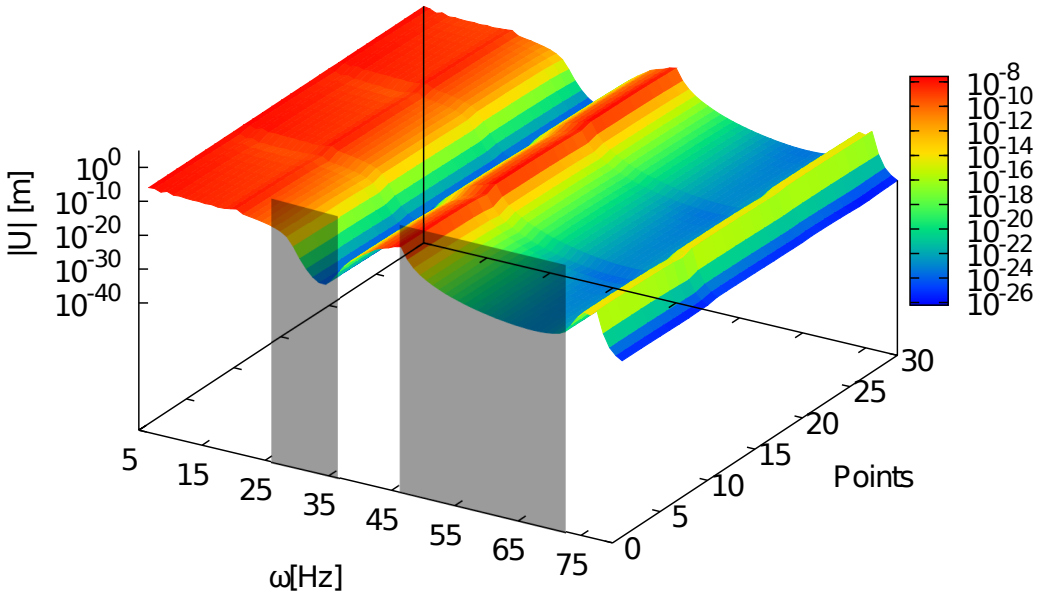

(a)

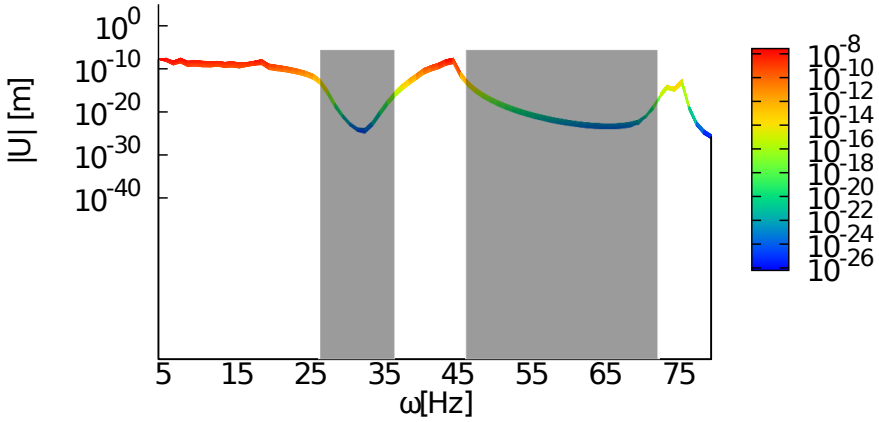

(b)

Figure 6.18: The transmission of $|\mathbf{U}|$ of 20-Layer sturcture ((a)) and the projection to ω-$|\mathbf{U}|$ plane ((b)).

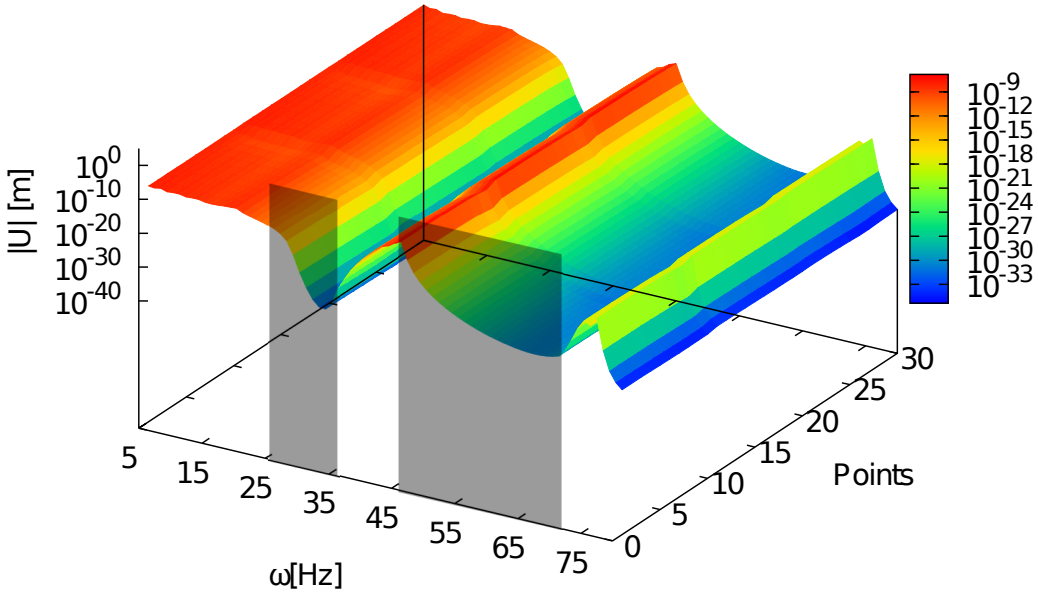

(a)

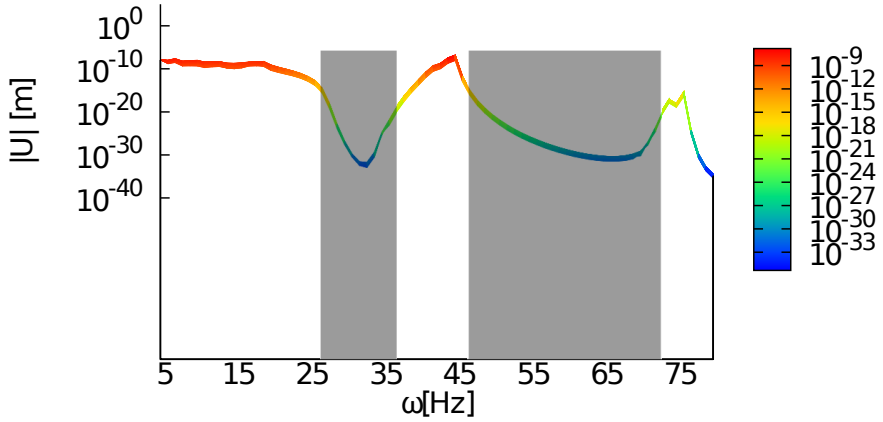

(b)

Figure 6.19: The transmission of $|\mathbf{U}|$ of 30-Layer sturcture ((a)) and the projection to ω-$|\mathbf{U}|$ plane ((b)).

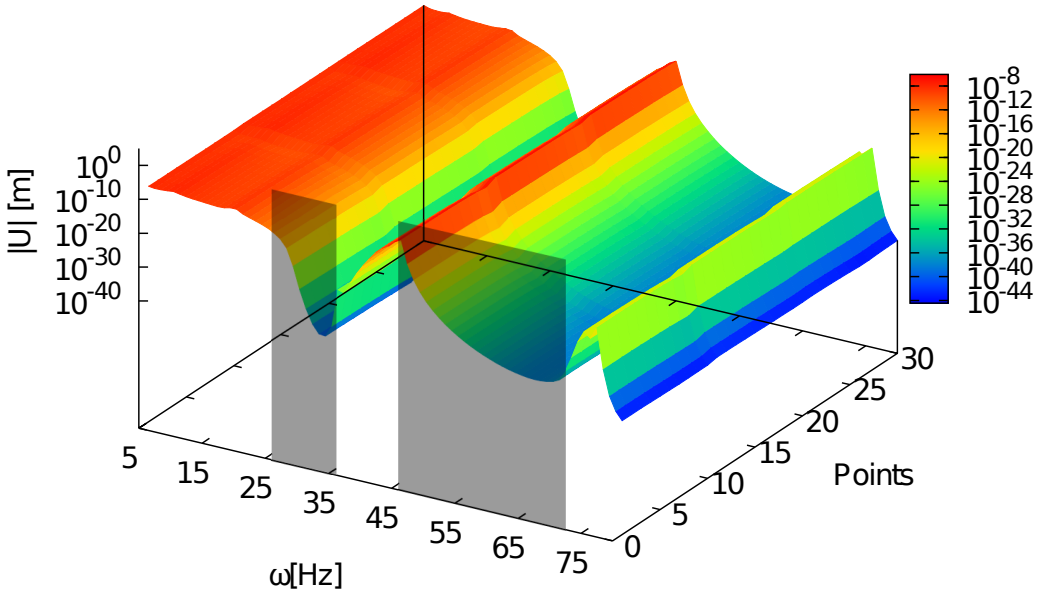

(a)

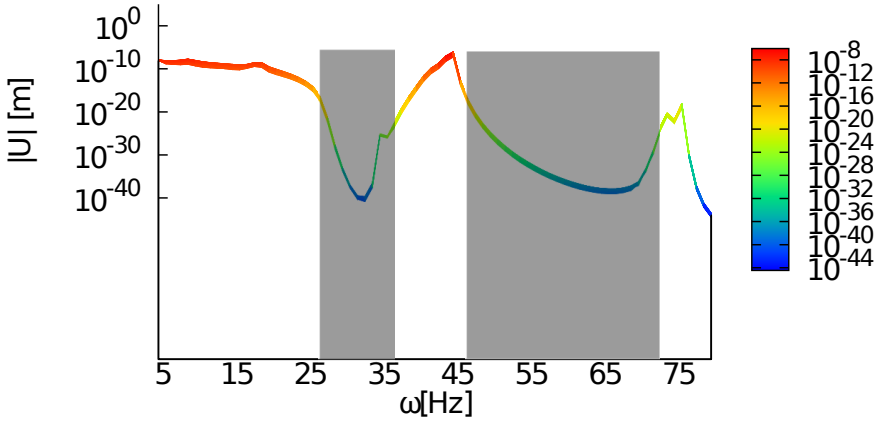

(b)

Figure 6.20: The transmission of $|\mathbf{U}|$ of 40-Layer sturcture ((a)) and the projection to ω-$|\mathbf{U}|$ plane ((b)).

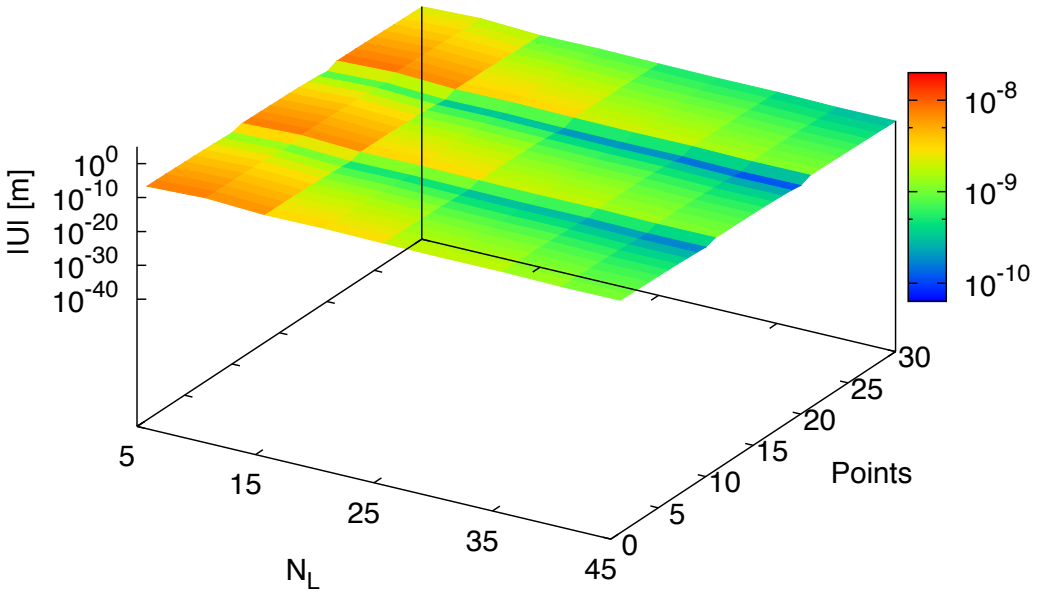

(a)

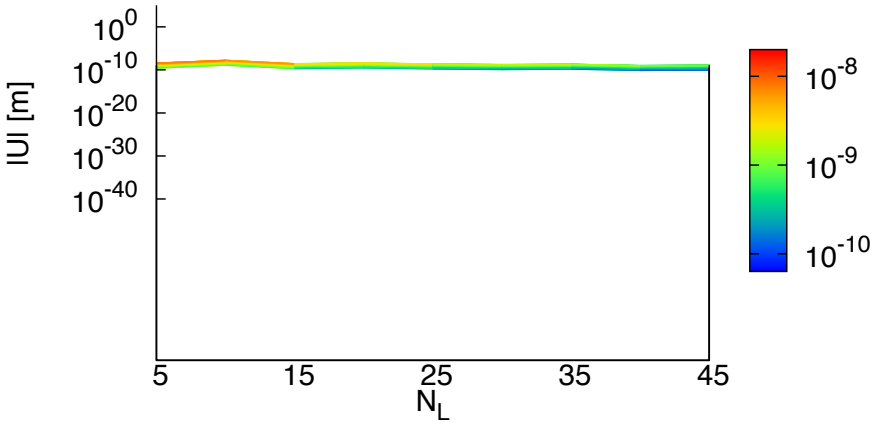

(b)

Figure 6.21: The transmission of $|\mathbf{U}|$ at 15Hz against different number of layers ((a)) and the projection to ω-$|\mathbf{U}|$ plane ((b)).

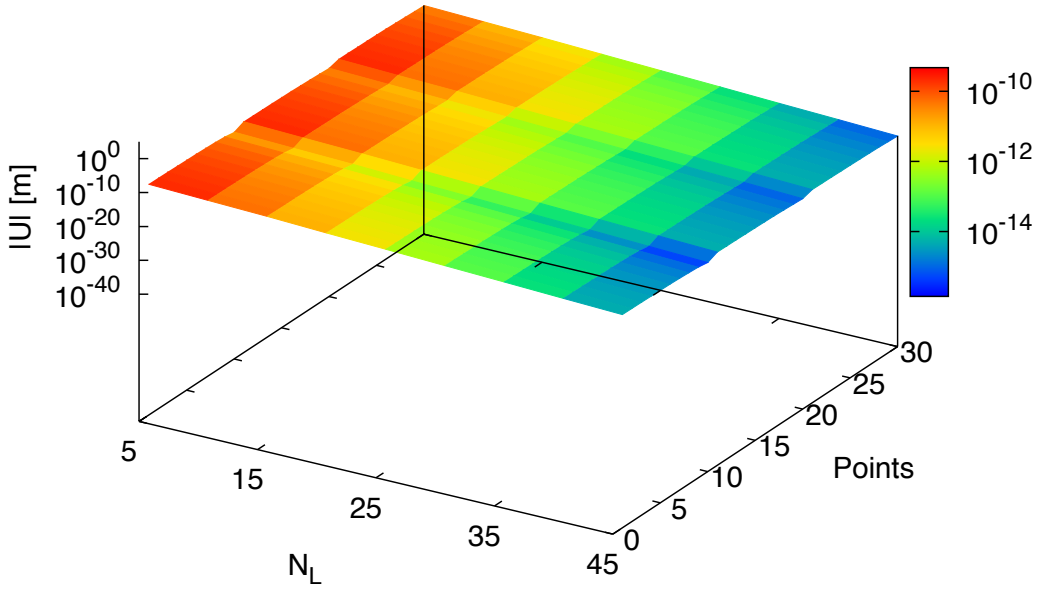

(a)

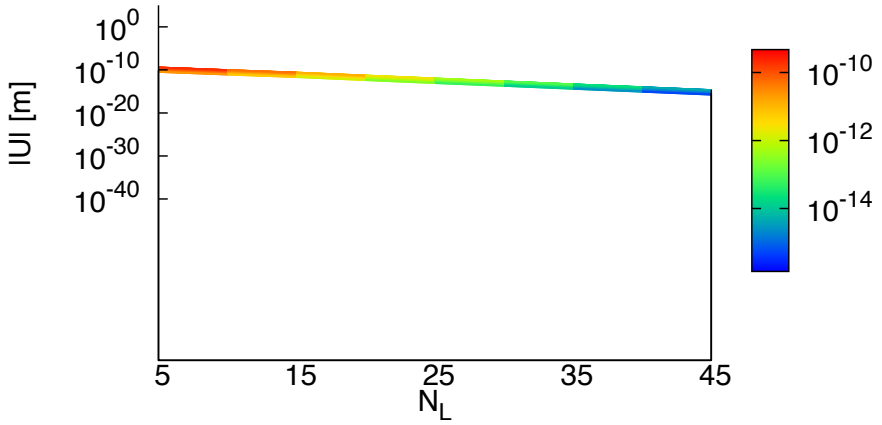

(b)

Figure 6.22: The transmission of $|\mathbf{U}|$ at 40Hz against different number of layers ((a)) and the projection to ω-$|\mathbf{U}|$ plane ((b)).

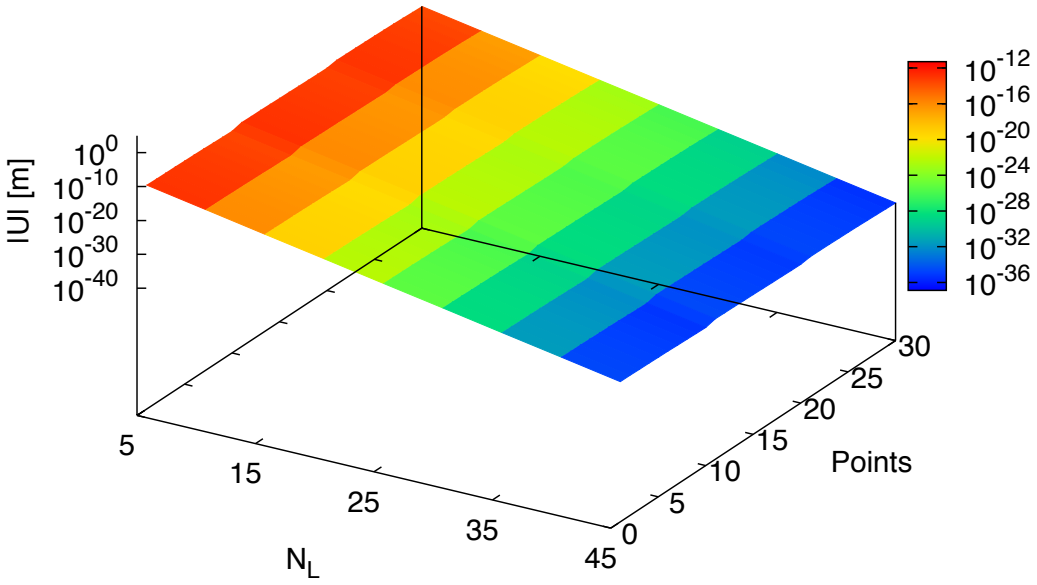

(a)

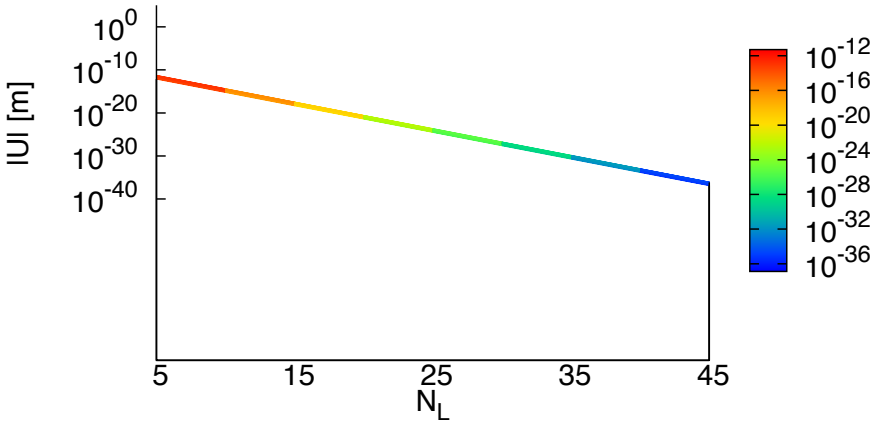

(b)

Figure 6.23: The transmission of $|\mathbf{U}|$ at 30Hz against different number of layers ((a)) and the projection to ω-$|\mathbf{U}|$ plane ((b)).

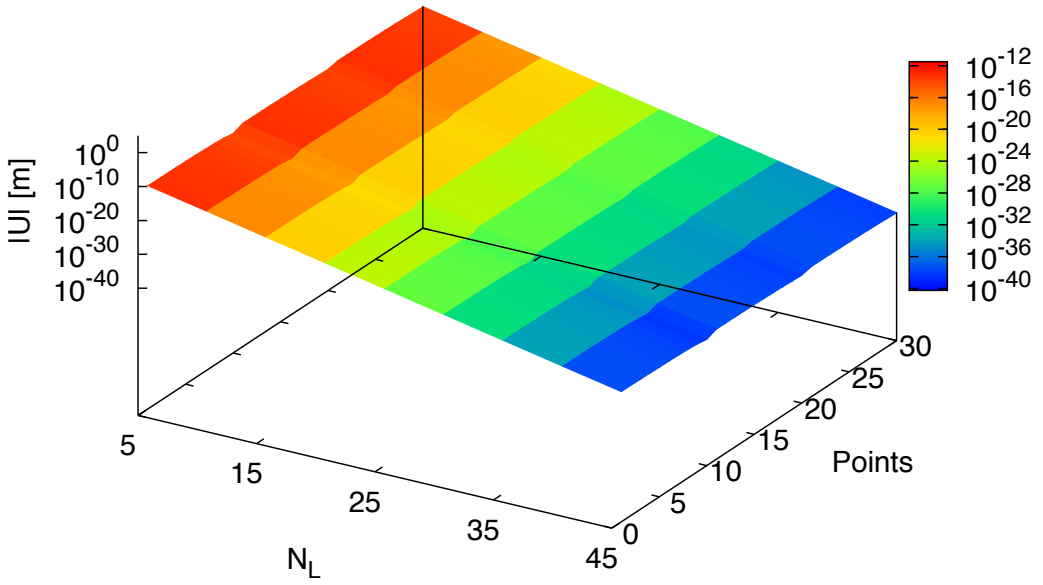

(a)

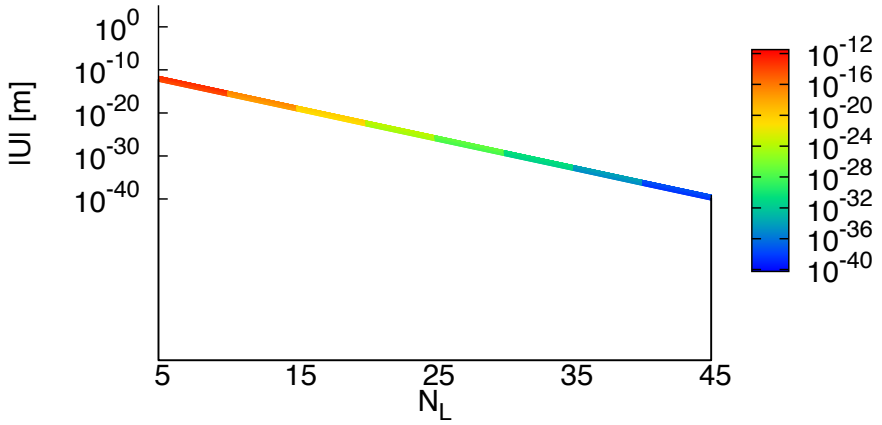

(b)

Figure 6.24: The transmission of $|\mathbf{U}|$ at 60Hz against different number of layers ((a)) and the projection to ω-$|\mathbf{U}|$ plane ((b)).

6.3.2.2 Example 2

This structure does not have real interfaces between adjacent cells. The virtual interfaces require additional boundary elements so the system matrix's dimension is reduced by $N_{\mathrm{L}}(n_{\mathrm{F}} - n_{\mathrm{IO}}) + n_{\mathrm{IO}}$. In particular, the eigenfrequencies of the structure, which has finite layers of cells, are extracted by using the BEM and the block SS method.

The structure of the unit cell is depicted in Fig. 6.25, where the same materials and their subscripts are used as those in the previous example. The square inclusion shown in gray color is assumed to be stiff and dense (material 2), while that shown in white color is compliant and light (material 1). A similar collocation of excitation and constraints is described in Fig. 6.26 and correspondingly, the coordinates of the observation points numbered as $1 \sim 10$ are (0.15, 1.5), (0.45, 1.5), ..., (2.85, 1.5), numbered as $11 \sim 20$ are (0.15, 2.25), (0.45, 2.25), ..., (2.85, 2.25), and those numbered as $21 \sim 30$ are (0.15, 0.75), (0.45, 0.75), ..., (2.85, 0.75), with the left bottom corner point of the right square output domain regarded as the origin of the coordinate axes.

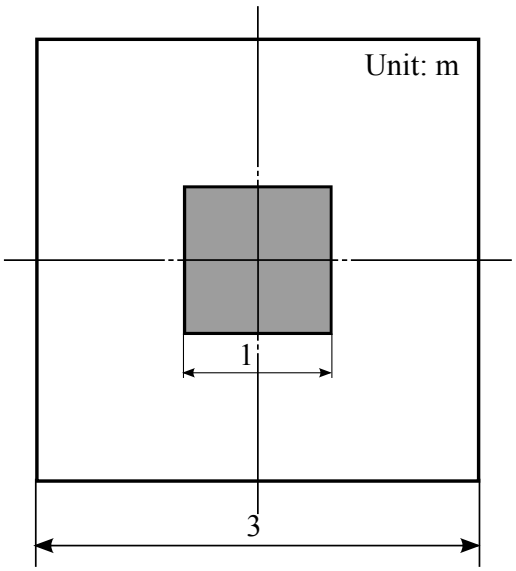

Figure 6.25: The unit cell (the stiff/dense material phase is shown in gray and the compliant/light material phase is shown in white).

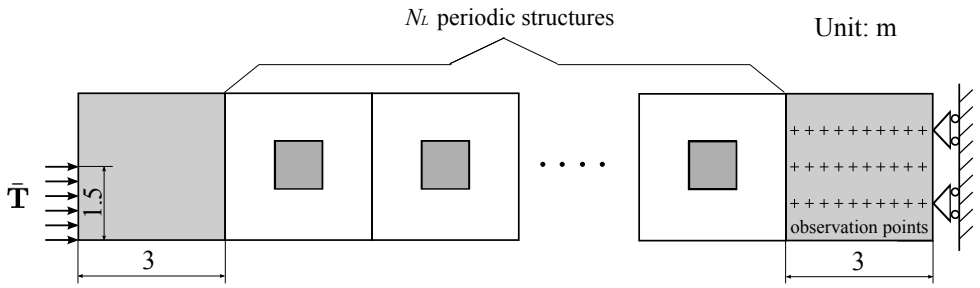

Figure 6.26: Two square domains connected (input domain is the left square domain in gray and output domain is the right square domain in gray) by N_L layers of cells in example 2 and the cross symbols denote the observation points..

Fig. 6.27 shows the dispersion relation which is based on an infinite periodic structure composed by the unit cell shown in Fig. 6.25. Two band gaps represented by the shaded ranges are found in the band structure of the selected range.

The displacement transmissions of the finite structure shown in Fig. 6.26 with different number of layers are plotted in Figs. 6.28 to Fig. 6.31. When $N_L = 40$, an apparent effect of the frequency bands can be observed because of the scattering and dispersion. The reduction of transmission is significant at the stop bands which is determined by infinite periodic structure. This means that the finite structure with a sufficient number of layers still keeps the frequency-banded nature.

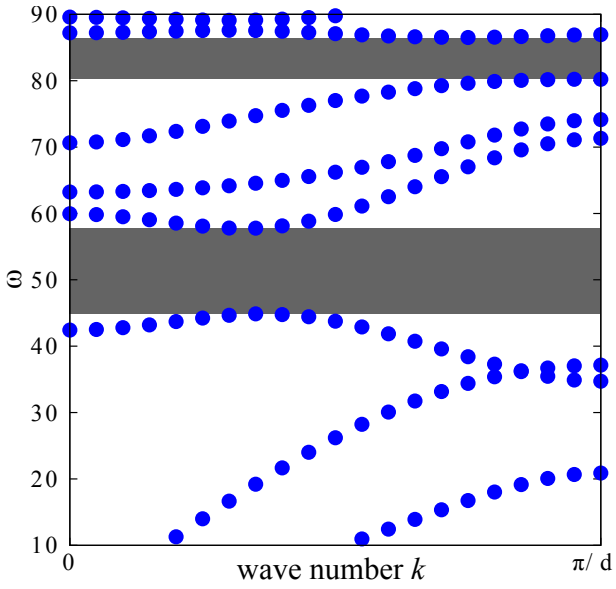

Figure 6.27: The band structure for the infinite structure (shade ranges denote the concerned band gaps).

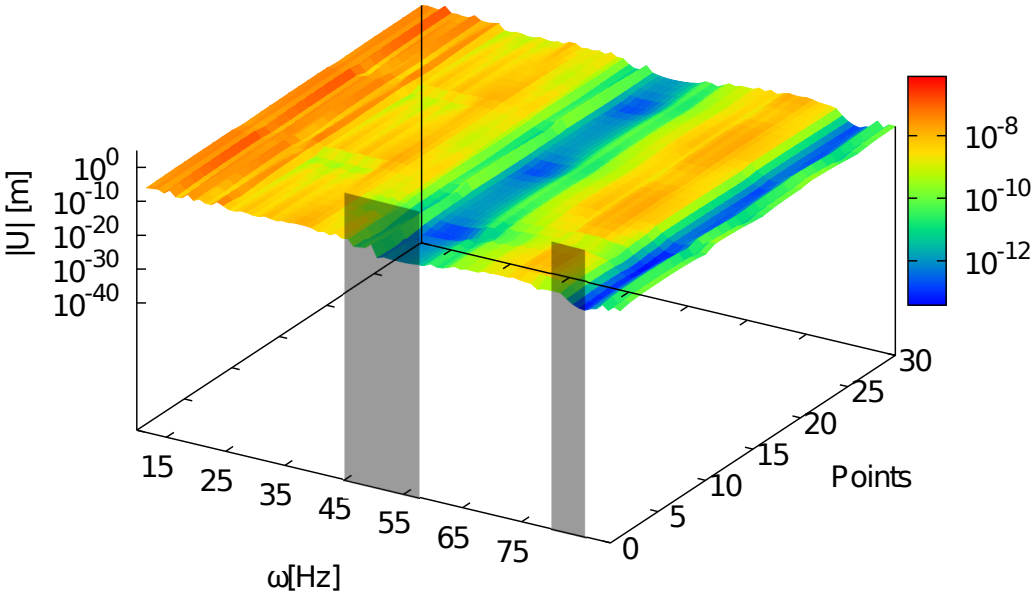

(a)

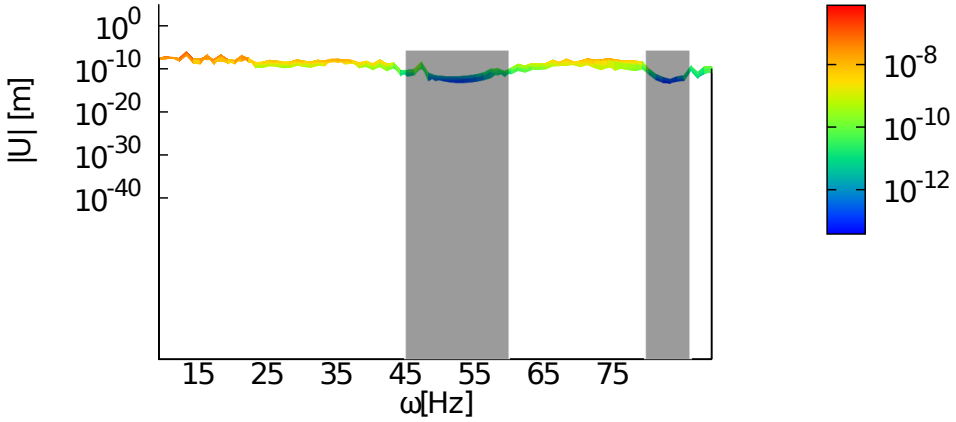

(b)

Figure 6.28: The transmission of $|\mathbf{U}|$ of 10-Layer sturcture ((a)) and the projection to ω-$|\mathbf{U}|$ plane ((b)).

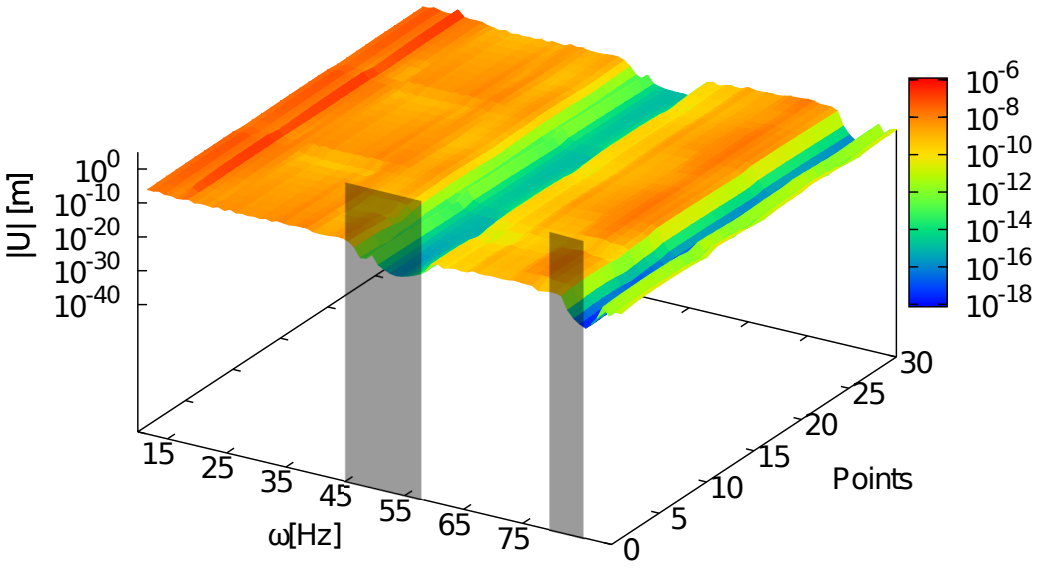

(a)

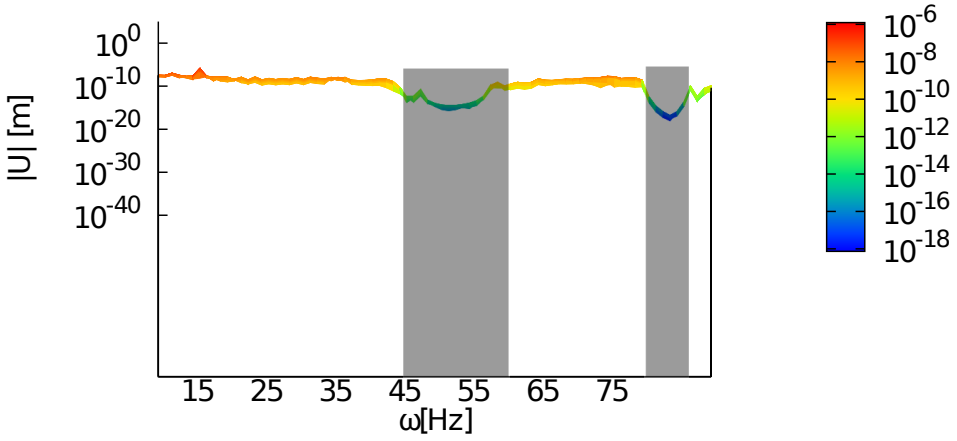

(b)

Figure 6.29: The transmission of $|\mathbf{U}|$ of 20-Layer sturcture ((a)) and the projection to ω-$|\mathbf{U}|$ plane ((b)).

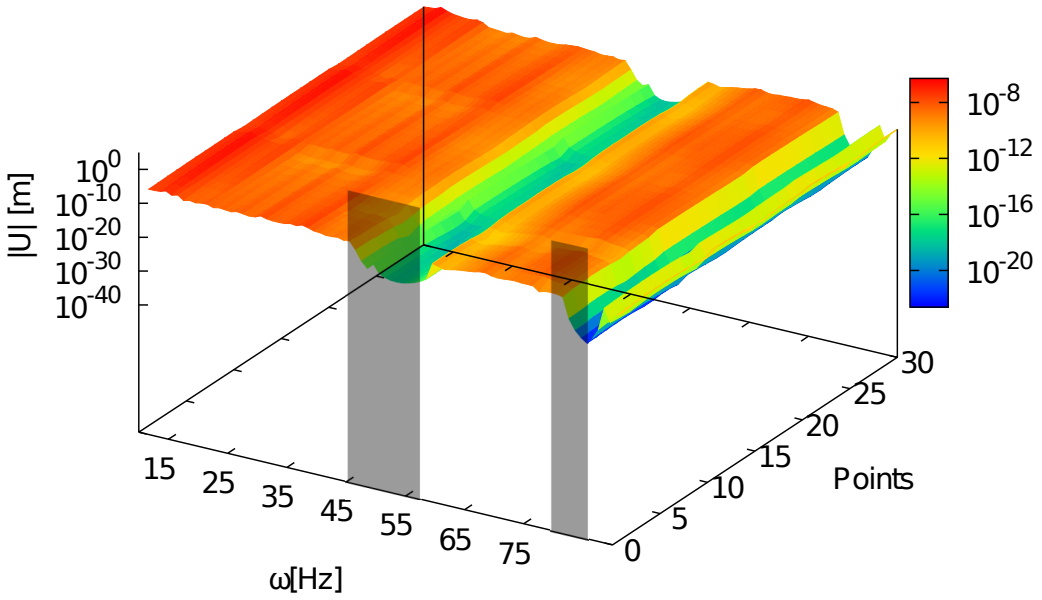

(a)

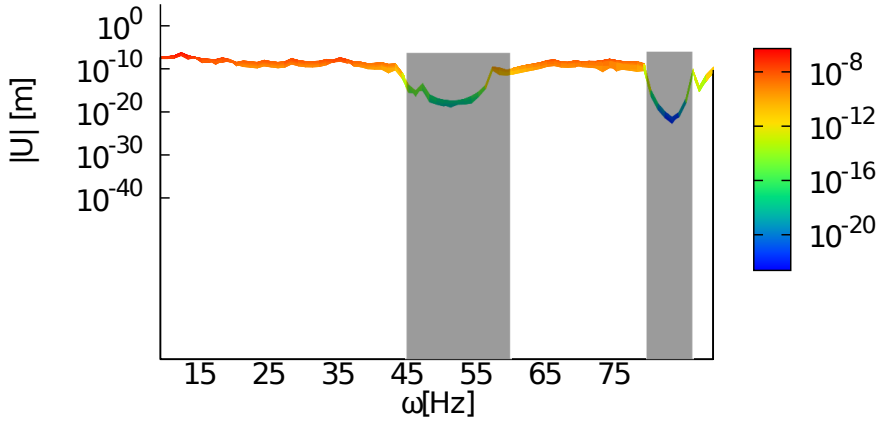

(b)

Figure 6.30: The transmission of $|\mathbf{U}|$ of 30-Layer sturcture ((a)) and the projection to ω-$|\mathbf{U}|$ plane ((b)).

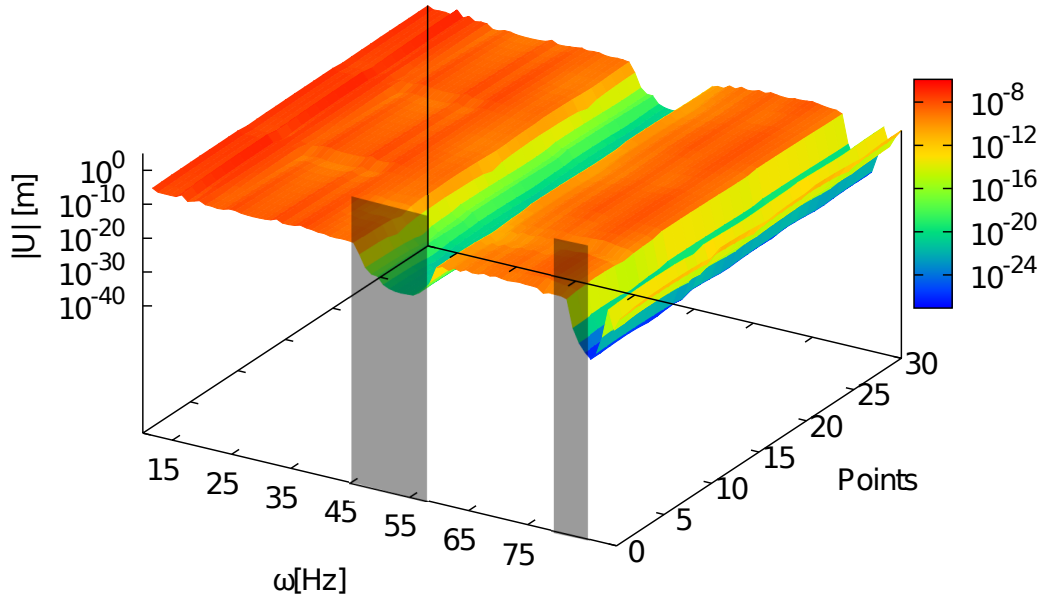

(a)

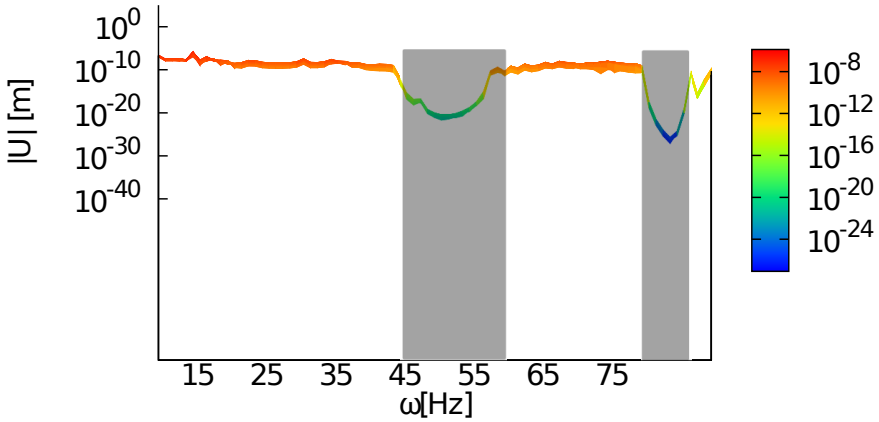

(b)

Figure 6.31: The transmission of $|\mathbf{U}|$ of 40-Layer sturcture ((a)) and the projection to ω-$|\mathbf{U}|$ plane ((b)).

The reductions of the transmissions in the finite structure at the frequencies in concerned pass band and stop band shown in Fig. 6.27 are plotted in Fig. 6.32 $\sim$ Fig. 6.35. The frequencies at 25, 65 Hz and 50, 85 Hz are chosen in the pass bands and stop bands, respectively. In this example, we do not find the reduction of transmissions at the frequencies in pass bands. The reductions centralize mainly in stop bands.

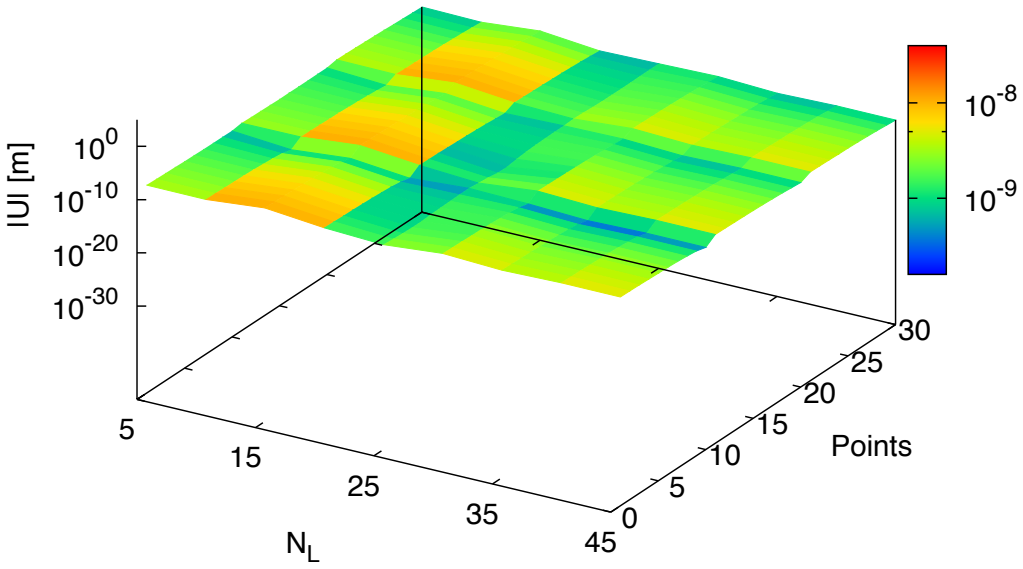

(a)

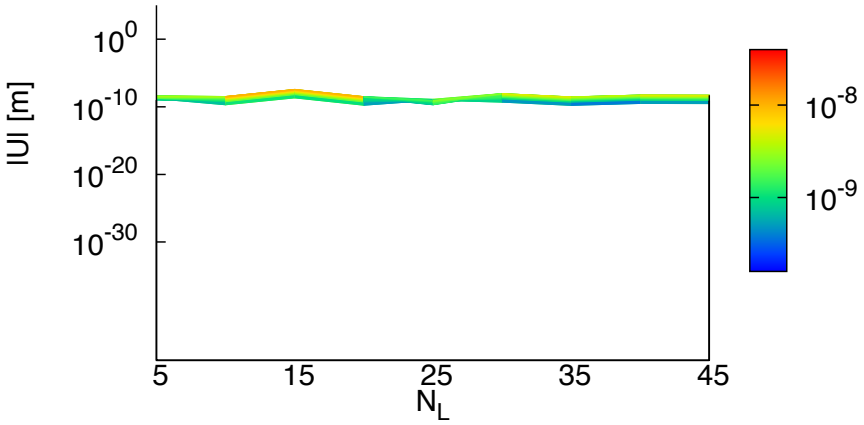

(b)

Figure 6.32: The transmission of $|\mathbf{U}|$ at 25Hz against different number of layers ((a)) and the projection to ω-$|\mathbf{U}|$ plane ((b)).

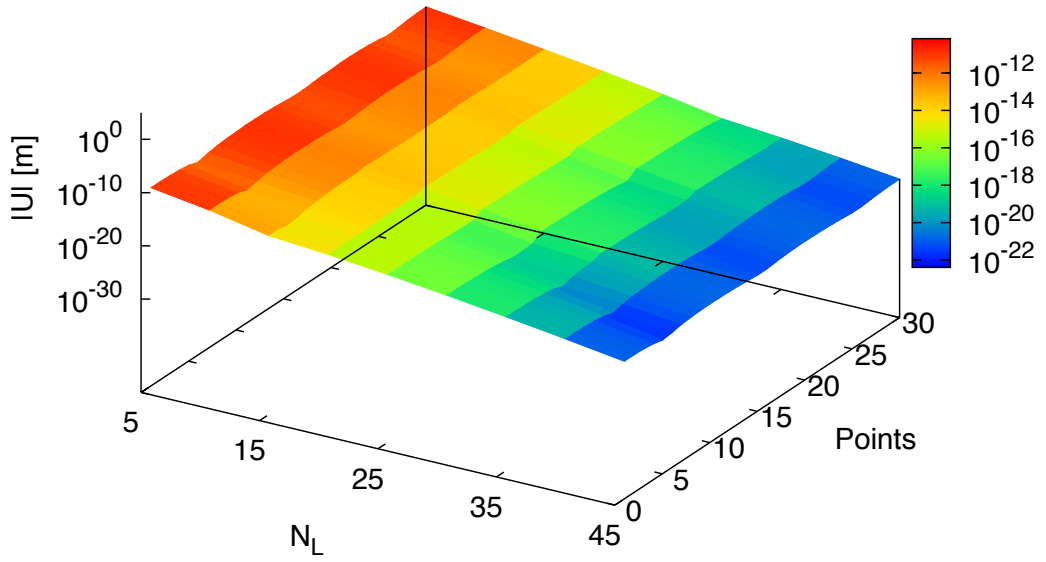

(a)

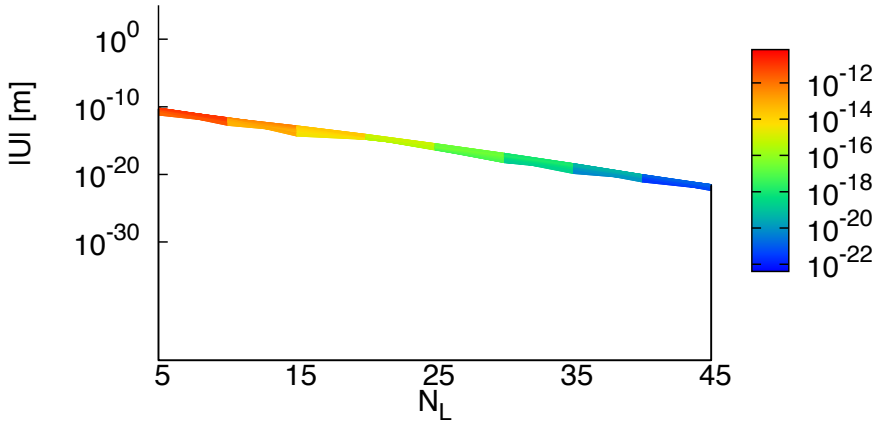

(b)

Figure 6.33: The transmission of $|\mathbf{U}|$ at 50Hz against different number of layers ((a)) and the projection to ω-$|\mathbf{U}|$ plane ((b)).

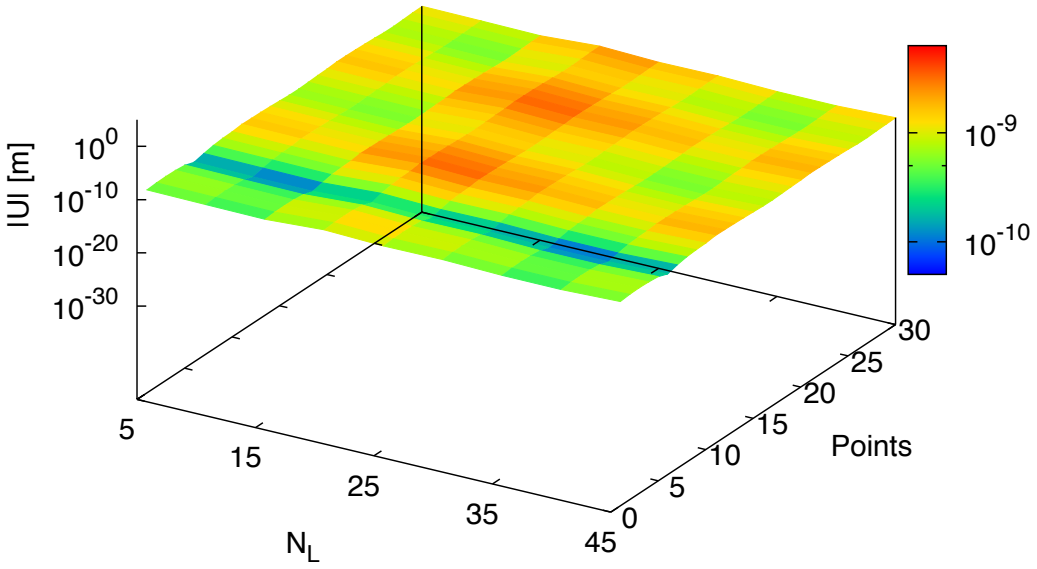

(a)

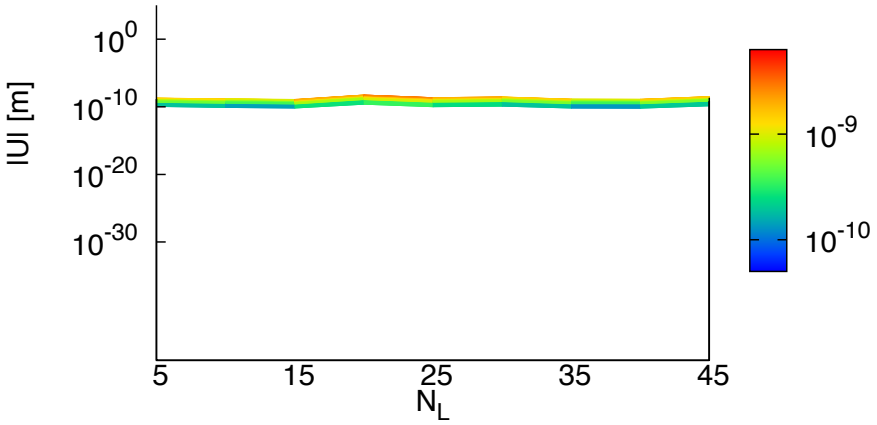

(b)

Figure 6.34: The transmission of $|\mathbf{U}|$ at 65Hz against different number of layers ((a)) and the projection to ω-$|\mathbf{U}|$ plane ((b)).

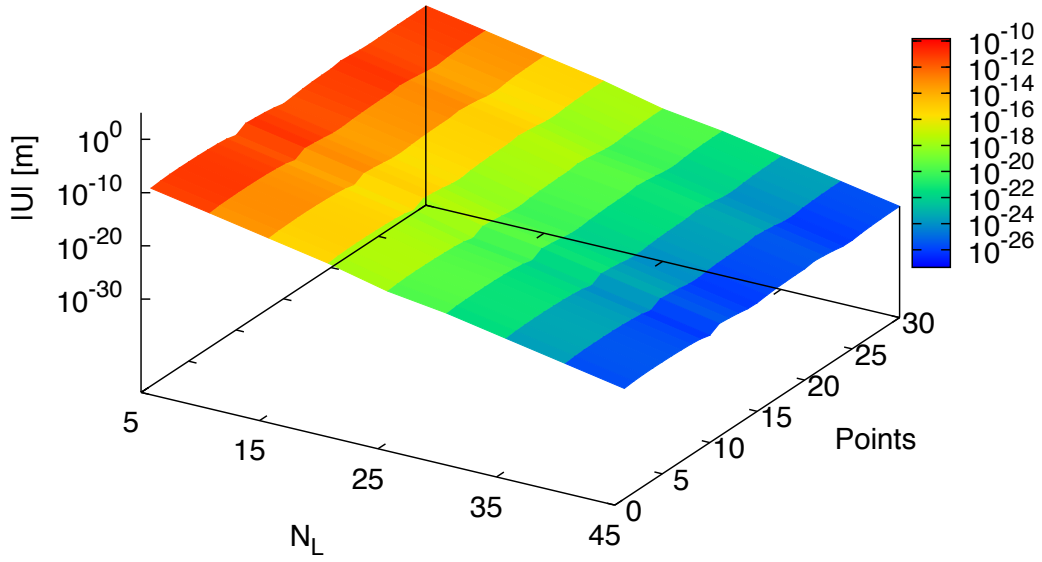

(a)

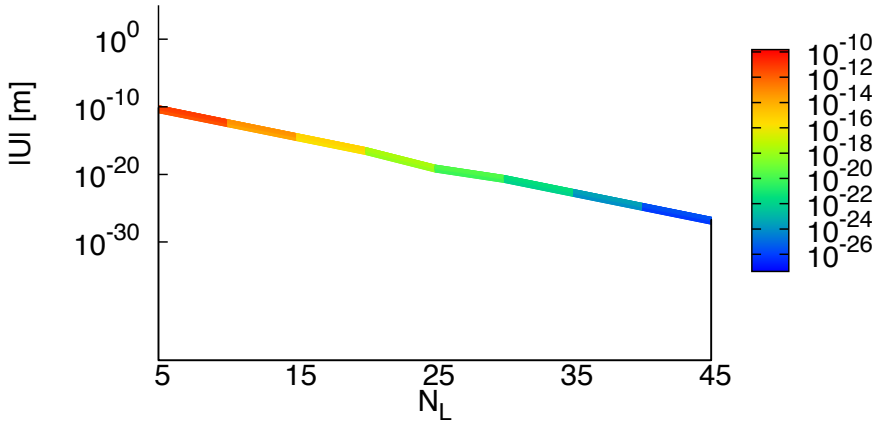

(b)

Figure 6.35: The transmission of $|\mathbf{U}|$ at 85Hz against different number of layers ((a)) and the projection to ω-$|\mathbf{U}|$ plane ((b)).

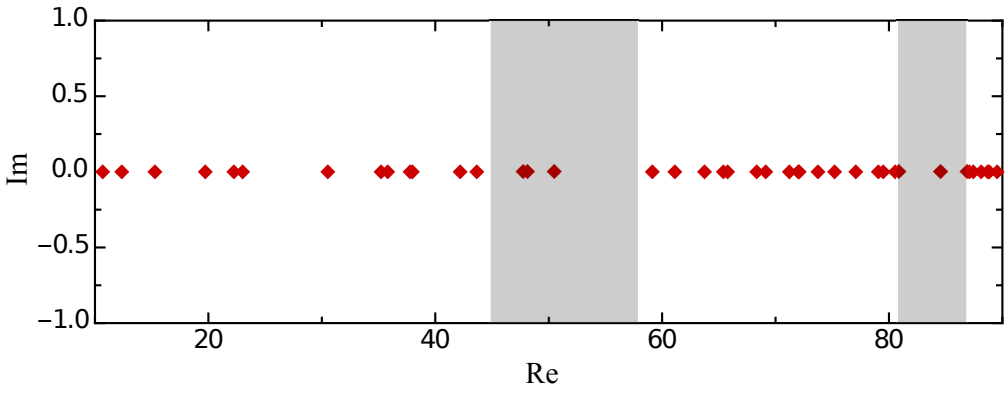

(a) 8 unit cells

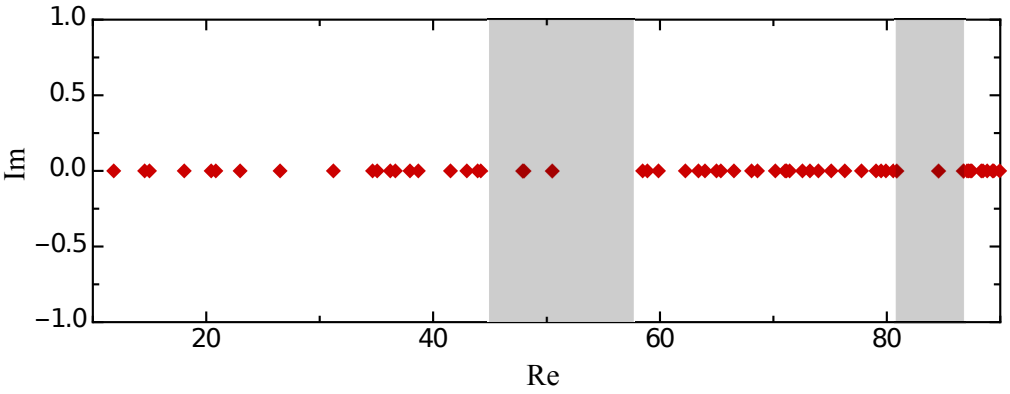

(b) 11 unit cells

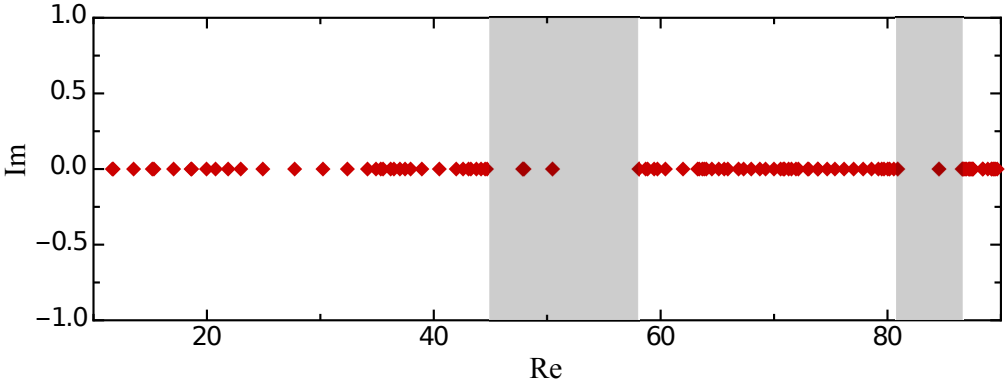

(c) 15 unit cells

Figure 6.36: The eigenfrequency distribution of the finite structure (shade ranges denote the stop bands).

The calculation of the eigenfrequencies for the finite structure in Fig. 6.26 is also carried out. The system matrix in Eq. (6.7) involves the circular frequency ω in the nonlinear form in each component of the matrix. We solve this nonlinear eigenvalue problem also by using the block SS method. The locations of the eigenfrequencies

display a banded distribution. In Fig. 6.36, three eigenfrequencies and one eigenfrequency are found in the first and second bands, respectively. These eigenfrequencies appearing in the stop bands are found to be constants, when the number of layers of unit cells is increased. They correspond to the local resonances of the input and output domains. More unit cells make a denser eigenfrequency distribution in the pass bands, but no more eigenfrequency appears in the stop bands. The banded distribution of eigenfrequencies also implies that the finite structure presents a frequency-banded nature.

6.4 Conclusion

In this chapter, infinite/finite unidirectional phononic structures in 2D have been investigated using the BEM. The analyses cover both acoustic and elastic problems.

The band structure of the unidirectional infinite phononic plates is computed by using the proposed methodology that has been employed in the previous two chapters. To investigate the wave transmission in a finite structure, a size-reduced system matrix is derived by utilizing the transfer matrix formulated by using the BEM repeatedly. The wave transmission is calculated against the frequency and the number of layers. With a sufficient number of layers of cells, the finite structure also exhibits a frequency-banded nature that coincides with the band structure of the infinite structure and can be enhanced through increase in number of the unit cells. This nature can also be confirmed by the natural frequency calculation of the finite structure. A reduction of transmission may also happen in the finite structure at the frequencies in the pass bands of the infinite structure with an increase in number of the cells comprising alternating layers of materials. However, this reduction is much slower than that at the frequency in the stop bands.

CHAPTER VII

Conclusions

In this thesis, a new BEM-based methodology for the band calculation of phononic structures is constructed. Unlike those methods which employ a quasi-periodic structures, our approach does not have the issue of convergence for the wave function. Also different from the domain methods, the proposed approach requires only boundary discretization which make the preprocessing easier. The block SS method is employed to overcome the difficulties that stem from the nonlinear property of the fundamental solutions adopted in the BEM. As very basis, the propose approach is applied to the resonance of acoustic cavities. Then various phononic structure are investigated by using the constructed methodology. The following results are obtained:

1. As a starting point for the application of the proposed BEM-based methodology to a periodic structure, the eigenfrequencies for resonance of acoustic cavities are extracted by using the BEM combined with the block SS method. Accurate numerical solutions are obtained and compared with the close form. By checking the behavior of the singular values of Hankel matrix, an appropriate threshold for the rank detection is chosen. The real spurious eigenfrequencies which are related to the internal boundary of a multiply connect domain are produced by CBIE. The real spurious eigenfrequencies are identified by using Burton-Miller's method, by which the shift of real spurious eigenfrequencies are observed.

2. Since the preparation works of the calculation of the eigenfrequencies for multiply connected domains have been done, the BEM is applied to the band calculation of the acoustic phononic structures. The effectiveness of the methodology are demonstrated by solving the band structures for two typical structures: homogeneous medium with rigid scatterers, composite mediums. The spurious eigenfrequencies in the Bloch eigenvalue problem appear as horizontal lines

in the band structures of both phononic structures. By using Burton-Miller's method, these horizontal lines are removed effectively and band gaps are observed in the band structures.

3. Applying the methodology to a more complicated propagation of both longitudinal and transverse waves in elastic solids, three typical elastic phononic structures are proposed: a two-phase 2D phononic structure base on Bragg scattering, a unidirectional 2D bounded phononic structure with traction-free boundaries and a three-phase phononic structure.

4. Besides the analyses of infinite phononic structures to which the Bloch theorem can be applied, finite unidirectional periodic structures are proposed for the importance of practical problem. Instead of formulating the whole system matrix, the transfer matrix based on the BEM serves repeatedly to form a size-reduced coefficient matrix for the transmission problem. The transmission of sound pressure/displacement from a input domain to a output domain that are connected by the unidirectional phononic cells is investigated with models containing different number of cells. The results show that reductions of transmission happen in the band gaps of the corresponding infinite structures. The reduction effect can be enhanced by increasing the number of cells between the input and output domains. Thus the finite structures also present a frequency-banded nature. A slight reduction is also observed at pass band as the number of cells is increasing, however, this reduction is negligible, compared with that in band gaps. Furthermore, the eigenfrequencies of the finite structures are extracted by the proposed approach. As a direct inspection for their frequency-banded nature, locations of eigenfrequencies for the finite structures are found to have a band distribution.

In summary, a new BEM-based methodology aimed at solving the band structure of phononic crystals is proposed. Numerical simulations cover various eigenvalue problems in homogeneous and phononic periodic structures. The numerical results demonstrate the effectiveness of our approach. Moreover, meaningful conclusions on infinite/finite phononic structures are obtained.

With the proposed methodology in the thesis, one can calculate the eigenfrequencies in a desired range by using the BEM without any domain discretization or interpolation. Also because of this, accurate solutions can be obtained. For the band calculation of phononic structures, the complexity of the designed unit cell does not affect the effectiveness of the method.

The further investigation will be conducted on the complicated 3D phononic structures with fast BEM algorithms whose codes are being developed. With the BEM, a simpler phononic BEM model that has only a scatterer, is enough for the band calculation if the quasi-periodic fundamental solution is employed. This means that size of the coefficient matrix can be reduced further. In particular, it may provide a easier algorithm as the basis of topological optimization of phononic structures, since the BEM model just has the boundary of the scatterer whose topological structure needs to be modified.

Bibliography

[1] J. Asakura, T. Sakurai, H. Tadano, T. Ikegami, and K. Kimura. A numerical method for nonlinear eigenvalue problems using contour integrals. *JSIAM. Lett*, 1:52–55, 2009.

[2] T. Gorishnyy, M. Maldovan, C. Ullal, and Thomas. E. Sound idears-physicsworld.com. *physicsworld.com*, 2005.

[3] E. Yablonovitch. Inhibited spontaneous emission in solid-state physics and eletronics. *Phys. Rev. Lett*, 58:2059–2062, 1987.

[4] J. D. Joannopoulos, R. D. Meade, and J. N. Winn. *Photonic crystals: modeling the flow of light*. Princeton Univ. Press, New Jersey, 1995.

[5] J. D. Joannopoulos, P. R. Villeneuve, and S. H. Fan. Putting a new twist on light. *Nature*, 386:143–149, 1997.

[6] Z. Y. Liu, X. X. Zhang, Y. W. Mao, Z. Y. Yang, C. T. Chan, and P. Sheng. Locally resonant sonic materials. *Science*, 289:1734–1736, 2000.

[7] H. Jia, M. Z. Ke, Y. T. Ye, F. M. Liu, and Z. Y. Liu. Subwavelength imaging by a simple planar acoustic superlens. *Appl. Phys. Lett.*, 97:173507, 2010.

[8] R. W. Haupt and D. Rolt. Standoff acoustic laser technique to locate buried land mines. *Lincoln Laboratory Journal*, 15:3–22, 2005.

[9] E. Dechaumphai and Renkun. Chen. Thermal transport in phononic crystals: The role of zone folding effect. *J. Appl. Phys.*, 111:073508, 2012.

[10] X. S. Guo, Z. Lin, J. Tu, B. Liang, J. C. Cheng, and D. Zhang. Modeling and optimization of an acoustic diode based on micro-bubble nonlinearity. *J. Acoust. Soc. Am.*, 133:1119–1125, 2013.

[11] M. Zubtsov, R. Lucklum, M. Ke, A. Oseev, R. Grundmann, B. Henning, and U. Hempel. 2D phononic crystal sensor with normal incidence of sound. *Sensor. Actuat. A-Phys.*, 186:118–124, 2012.

[12] X. D. Jing, P. Sheng, and M. Y. Zhou. Acoustic and electromagnetic quasimodes in dispersed random media. *Phys. Rev. A*, 46:6513, 1992.

[13] L. Ye, J. Liu, P. Sheng, and D. A. Weitz. Sound propagation in suspensions of solid spheres. *Phys. Rev. E*, 48:2805, 1993.

[14] C. E. Bradley. Time harmonic acoustic Bloch wave propagation in periodic waveguides. Part II.: Experiment. *J. Acoust. Soc. Am.*, 96:1854, 1994.

[15] R. Martinez-Sala, J. Sancho, J. V. Sanchez, Gomez. V., J. Llinares, and F. Meseguer. Sound attenuation by sculpture. *Nature*, 378:241, 1995.

[16] R. James, S. M. Woodley, C. M. Dyer, and V. F. Humphrey. Sonic bands, bandgaps, and defect states in layered structures-Theory and experiment. *J. Acoust. Soc. Am.*, 97:2041, 1995.

[17] J. H. Page, P. Sheng, H. P. Schriemer, X. D. Jing, and D. A. Weitz. Group velocity in strongly scattering media. *Science*, 271:634, 1996.

[18] J. H. Page, H. P. Schriemer, I. P. Jones, P. Sheng, and D. A. Weitz. Classical wave propagation in strongly scattering media. *Physica A*, 241:64, 1997.

[19] D. Garcia-Pablos, M. Sigalas, F. R. Montero de Espinoza, M. Torres, M. Kafesaki, and N Garcia. Theory and experiment on elastic band gaps. *Phys. Rev. Lett.*, 84:4349, 2000.

[20] J. V. Sanchez-Perez, C. Rubio, R. Matinez-Sala, R. Sanchez-Grandia, and V. Gomez. Acoustic barriers based on periodic arrays of scatterers. *Appl. Phys. Lett.*, 81:5240, 2002.

[21] D. Sutter and W. Steurer. Ultrasonic investigation of phononic Penrose crystals. *Phys. Stat. Sol. (c)*, 1:2716, 2004.

[22] D. Sutter-Widmer, P. Neves, P. Itten, R. Sainidou, and W. Steurer. Distinct band gaps and isotropy combined in icosahedral band gap material. *J. Acoust. Soc. Am.*, 97:2041, 1995.

[23] M. Sigalas and E. N. Economou. Band structure of elastic waves in two dimensional systems. *Solid State Commun*, 86:141–143, 1993.

[24] M. S. Kushwaha, P. Halevi, L. Dobrzynski, and B. Djafari-Rouhani. Acoustic band structure of periodic elastic composites. *Phy. Rev. Lett.*, 71:2022–2025, 1993.

[25] M. S. Kushwaha. Stop-bands for periodic metallic rods: Sculptures that can filter the noise. *Appl. Phys. Lett.*, 70:3218, 1997.

[26] M. S. Kushwaha, B. Djafar-Rouhani, L. Dobrzynski, and J. O. Vasseur. Sonic stop-bands for cubic arrays of rigid inclusions in air. *Eur. Phys. J. B*, 3:155, 1998.

[27] L. W. Cai and J. H. Williams Jr. Full-scale simulations of elastic wave scattering in fiber reinforced composites. *Ultrasonics*, 37:463, 1999.

[28] Z. Ye and H. Hsu. Phase transition and acoustic localization in arrays of air bubbles in water. *Appl. Phys. Lett.*, 79:1724, 2001.

[29] B. C. Gupta and Z. Ye. Theoretical analysis of the focusing of acoustic waves by two-dimensional sonic crystals. *Phys. Rev. E*, 67:036603, 2003.

[30] Y. J. Cao, Z. L. Hou, and Y. Y. Liu. Finite difference time domain method for band-structure calculations of two-dimensional phononic crystals. *Solid Stat Commun.*, 132:539–543, 2004.

[31] J. C. Hsu and T. T. Wu. Lamb waves in binary locally resonant phononic plates with two-dimensional lattices. *Appl. Phys. Lett.*, 90:201904, 2007.

[32] C. Goffaux and J. P. Vigneron. Theoretical study of a tunable phononic band gap system. *Phys. Rev. B*, 64:075118, 2001.

[33] M. Kafesaki and E. N. Economou. Multiple-scattering theory for three-dimensional periodic acoustic composites. *Phy. Rev. B*, 60:11993, 1999.

[34] I. E. Psarobas, N. Stefanou, and A. Modinos. Scattering of elastic waves by periodic array of spherical bodies. *Phy. Rev. B*, 62:278–291, 2000.

[35] Z. Y. Liu, C. T. Chan, and P. Sheng. Three-component elastic wave band-gap material. *Phy. Rev. B*, 65:165116, 2002.

[36] Y. Tanaka, Y. Tomoyasu, and S. Tamura. Band structure of acoustic waves in phononic lattice: two-dimensional composites with large acoustic mismatch. *Phy. Rev. B*, 62:7387, 2000.

[37] J. O. Vasseur, P. A. Deymier, A. Khelif, P. H. Lambin, B. Djafari-Rouhani, A. Akjouj, L. Dobrzynski, N. Fettouhi, and J. Zemmouri. Phononic crystal with low filling fraction and absolute acoustic band gap in the audible frequency range: A theoretical and experiment study. *Phy. Rev. E*, 65:056608, 2002.

[38] Z. Z. Yan and Y. S. Wang. Wavelet-based method for calculating elastic band gaps of two-dimensional phononic crystals. *J. Comput. Phys*, 74:224303, 2006.

[39] J. B. Li, Y. S. Wang, and C. Z. Zhang. Finite element method for analysis of band structures of phononic crystal slabs with archimedean-like tilings. *IEEE International Ultrasonics Symposium Proceedings*, pages 1548–1551, 2009.

[40] F. L. Li, Y. S. Wang, and C. Z. Zhang. Boundary element method for bandgap computation of photonic crystals. *Opt. Commun.*, 285:527–532, 2012.

[41] P. A. Knipp and T. L. Reinecke. Boundary-element calculations of electromagnetic band-structure of photonic crystals. *Physica. E*, 2:920–924, 1998.

[42] A. Barnett and L. Greengard. A new integral represntation for quasi-periodic fields and its application to two-dimensional band structure calculations. *J. Comput. Phys.*, 229:6898–6914, 2010.

[43] C. A. Brebbia, J. C. F. Telles, and L. C. Wrobel. *Boundary Element Techniques: Theory and Applications in Engineering*. Springer-Verlag, Berlin and NY, 1999.

[44] O. C. Zienkiewicz, R. L. Taylor, and J. Z. Zhu. *The Finite Element Method: Its Basis and Fundamentals*. Butterworth-Heinemann, Oxford, 6th edition, 2005.

[45] J. Vay. Asymmetric perfectly matched layer for the absorption of waves. *J. Comput. Phys.*, 183:367–399, 2002.

[46] T. Hohage and L. Nannen. Hardy space infinite elements for scattering and resonance problems. *SIAM J. Numer. Anal.*, 47:972–996, 2009.

[47] L. Greengard, J. F. Huang, V. Rokhlin, and S. Wandzura. Accelerating fast multipole methods for the Helmholtz equation at low frequencies. *IEEE Comput. Sci. Eng.*, 5:32–38, 1998.

[48] K. Amaya and S. Aoki. Effective boundary element methods in corrosion analysis. *Eng. Anal. Bound. Elem.*, 27:507–519, 2003.

[49] L. Shen and Y. J. Liu. An adaptive fast multipole boundary element method for three-dimensional acoustic wave problems based on the Burton-Miller formulation. *Comput. Mech.*, 40:461–472, 2007.

[50] M. Bebendorf and S. Rjasanow. Adaptive low-rank approximation of collocation matrices. *Computing*, 70:1–24, 2003.

[51] S. Kurz, O. Rain, and S. Rjasanow. Application of the adaptive cross approximation technique for the coupled BE-FE solution of symmetric electromagnetic problems. *Comput. Mech.*, 32:423–429, 2003.

[52] T. Sakurai and H. Sugiura. A projection method for generalized eigenvalue problems using numerical integration. *J. Comput. Appl. Math.*, 159:119–128, 2003.

[53] M. Yamaguchi, T. Matsumoto, and T. Takahashi. Application of SS method to eigenvalue analysis using boundary element method. *Proceedings of the 41st Graduation Thesis Presentation Meeting, JSME Tokai Branch*, pages 112–113, 2010.

[54] J. T. Chen, J. H. Lin, S. R. Kuo, and S. W. Chyuan. Boundary element analysis for the Helmholtz eigenvalue problems with multiply connected domain. *Proc. Roy. Soc. Lond. A.*, 457:2521–2546, 2001.

[55] A. J. Burton and G. F. Miller. The application of integral equation methods to the numerical solution of some exterior boundary-value problem. *Proc. Roy. Soc. Lond. A.*, 323:201–210, 1971.

[56] T. Ikegami and U. Sakurai, T. andNagashima. A filter diagonalization for generalized eigenvalue problems based on the Sakurai-Sugiura projection method. *J. Comput. Appl. Math.*, 233:1927–1936, 2010.

[57] W. J. Beyn. An integral method for solving nonlinear eigenvalue problems. *Linear Algebra Appl 2011*, 10:3839–3863, 2011.

[58] Y. Maeda, Y. Futamura, and T. Sakurai. Stochastic estimation method of eigenvalue density for nonlinear eigenvalue problem on the complex plane. *JSIAM letters*, 3:61–64, 2011.

[59] C. J. Zheng , T. Matsumoto, T. Takahashi, and H. B. Chen. A wideband fast multipole boundary element method for three dimensional acoustic shape sensitivity analysis based on direct differentiation method. *Eng. Anal. Bound. Elem.*, 36:361–371, 2012.

[60] G. R. C. Tai and R. P. Shaw. Helmholtz-Equation Eigenvalues and Eigenmodes for Arbitrary Domains. *J. Acoust. Soc. Am.*, 56:796–804, 1974.

[61] J. O. Adeyeye, M. J. M. Bernal, and K. E. Pitman. An improved boundary Integral-equation method for Helmholtz problems. *Int. J. Numer. Meth. Eng.*, 21:779–787, 1985.

[62] J. Zhou. Computations of eigenfunctions and eigenfrequencies of two dimensional vibrating structures by the boundary element method. *Proc. 28th IEEE Conference on Decision and Control*, 3:2045–2049, 1989.

[63] G. Bezine . A mixed boundary integral - finite element approach to plate vibration problems. *Mech. Res. Commun.*, 7:141–150, 1980.

[64] D. Nardini and C. A. Brebbia. A new approach to free-vibration analysis using boundary elements. *Appl. Math. Model.*, 7:157–162, 1983.

[65] D. Nardini and C. A. Brebbia. Dynamic analysis in solid mechanics by an alternative boundary element procedure. *Soil. Dyn. Earthq. Eng.*, 2:228–233, 1983.

[66] D. P. N. Kontoni, P. W. Partridge, and C. A. Brebbia. The dual reciprocity boundary element method for the eigenvalue analysis of Helmholtz problems. *Adv. Eng. Softw. Workst.*, 13:2–16, 1991.

[67] C. G. Provatidis. On DR/BEM for eigenvalue analysis of 2-D acoustics. *Comput. Mech.*, 35:41–53, 2004.

[68] K. Li, Q. B. Huang, and Y. Miao. Dual reciprocity hybrid boundary node method for acoustic eigenvalue problems. *Eng. Anal. Bound. Elem.*, 34:359–368, 2010.

[69] G. Davi and A. Milazzo. A regular variational boundary model for free vibrations of magneto-electro-elastic structures. *Eng. Anal. Bound. Elem.*, 35:303–312, 2011.

[70] A. J. Nowak and C. A. Brebbia. The multiple-reciprocity method. A new approach for transforming BEM domain integrals to the boundary. *Eng. Anal. Bound. Elem.*, 6:164–167, 1989.

[71] S. M. Kirkup and S. Amini. Solution of the Helmholtz eigenvalue problem via the boundary element method. *Int. J. Numer. Meth. Eng.*, 36:321–330, 1993.

[72] M. Denda, C. Y. Wang, and Y. K. Yong. 2-D time-harmonic BEM for solids of general anisotropy with application to eigenvalue problems. *J. Sound. Vib.*, 261:247–276, 2003.

[73] M. Denda, Y. Araki , and Y. K. Yong. Time-harmonic BEM for 2-D piezoelectricity applied to eigenvalue problems. *Int. J. Solids. Struct.*, 41:7241–7265, 2004.

[74] N. Kamiya, E. Andoh, and K. Nogae. Eigenvalue analysis by the boundary element method: new developments. *Eng. Anal. Bound. Elem.*, 12:151–162, 1993.

[75] A. Ali, C. Rajakumar, and S. M. Yunus. Advances in acoustic eigenvalue analysis using boundary element Method. *Comput. Struct.*, 56:837–847, 1995.

[76] M. J. Crocker. *Handbook of Acoustics*. John Wiley & sons INC., NewYork, 1998.

[77] J. T. Chen, M. H. Chang, K. H. Chen, and I. L. Chen. Boundary collocation method for acoustic eigenanalysis of three-dimensional cavities using radial basis function. *Comput Mech*, 29:392–408, 2002.

[78] J. T. Chen, T. W. Lin, K. H. Chen, and S. W. Chyuan. True and spurious eigensolutions for the problems with the mixed-type boundary conditions using BEMs. *Finite. Elem. Anal. Des.*, 40:1521–1549, 2004.

[79] J. T. Chen, I. L. Chen, and K. H. Chen. A unified formulation for the spurious and fictitious frequencies in acoustics using the singular value decomposition and Fredholm alternative theorem. *J. Comput. Acoust.*, 14:157–183, 2006.

[80] S. Parmley, T. Zobrist, T. Clough, A. Perez-Miller, M. Makela, and R. Yu. Phononic band structure in a mass chain. *Appl. Phys. Lett.*, 67:777, 1995.

[81] R. Martínez-Sala, J. Sancho, J. V. Sánchez, V. Gómez, J. Llinares, and F. Meseguer. Sound attenuation by sculpture. *Nature*, 378:241, 1995.

[82] M. M. Sigalas. Defect states of acoustic waves in a two-dimensional lattice of solid cylinders. *J. Appl. Phys.*, 84:3026, 1998.

[83] A. Khelif, B. Djafari-Rouhani, J. O. Vasseur, and P. A. Deymier. Transmission and dispersion relations of perfect and defect-containing waveguide structures in phononic band gap materials. *Phy. Rev. B*, 68:024302, 2003.

[84] A. Khelif, A. Choujaa, B. Djafari-Rouhani, M. Wilm, S. Ballandras, and V. Laude. Traping and guiding of acoustic waves by defect modes in a full-band-gap ultrasonic crystal. *Phy. Rev. B*, 68:214301, 2003.

[85] G. Wang, J. H. Wen, X. Y. Han, and H. G. Zhao. Finite difference time domain method for the study of band gap in two-dimensional phononic crystals. *Acta Phy. Sin. -Ch. ed.*, 52:1943–1947, 2003.

[86] A. J. Burton and G. F. Miller. The application of integral equation methods to the numerical solution of some exterior boundary-value problems. *Proc. Roy. Soc. Lond. A.*, 323:201–210, 1971.

[87] A. Sommerfeld. *Partial differential equation in physics*. Academic Press, New York, 1949.

[88] C. J. Zheng , H. B. Chen, T. Matsumoto, and T. Takahashi. Three dimensional acoustic shape sensitivity analysis by means of adjoint variable method and fast multipole boundary element approach. *CMES: Computer Modeling in Engineering & Sciences*, 79:1–30, 2011.

[89] Z. Y. Qian, Z. D. Han, P. Ufimtsev, and S. N. Atluri. Non-Hyper-Singular Boundary Integral Equations for Acoustic Problems, Implemented by the Collocation-Based Boundary Element Method. *CMES: Computer Modeling in Engineering & Sciences*, 6:133–144, 2004.

[90] C. Kittel. *Introduction to solid state physics*. John Wiley & Sons, Inc, The United States of America, 8th edition edition, 2005.

[91] D. Colton and R. Kress. *Integral Equation Methods in Scattering Theory*. John Wiley, 1983.

[92] Z. Y. Liu, C. T. Chan, and P. Sheng. Analytic model of phononic crystals with local resonances. *Phys. Rev. B*, 71:014103, 2005.

[93] T. A. Cruse. A direct formulation and numerical solution of the general transient elastodynamic problem. *J. Math. Anal. Appl.*, 22:244–259, 1968.

[94] M. I. Hussein. Reduce Bloch mode expansion for periodic media band structure calculations. *Proc. R. Soc. A*, 465:2825–2848, 2009.

[95] R. Esquivel-Sirvent and G. H. Cocoletzi. Band structure for the propagation of elastic-waves in superlattices. *J. Acoust. Soc. Am.*, 95:86–90, 1994.

[96] M. R. Shen and W. W. Cao. Acoustic bandgap formation in a periodic structure with multilayer unit cells. *J. Phys. D. Appl. Phys.*, 33:1150, 2000.

[97] X. F. Wang, M. S. Kushwaha, and P. Vasilopoulos. Tunability of acoustic spectral gaps and transmission in periodically stubbed waveguides. *Phys. Rev. B*, 65, 2001.

[98] Y. W. Yao, Z. L. Hou, F. G. Wu, and X. Zhang. Low-frequency band gaps in one-dimensional thin phononic crystal plate with periodic stubbed surface. *Physica. B*, 406:2249–2253, 2011.

[99] W. W. Cao and W. K. Qi. Plane wave propagation in finite 2-2-composites. *J. Appl. Phys.*, 1995.

[100] A. Bedford. *Drumheller DS. Introduction to Elastic Wave Propagation.* Wiley, Chichester, 1994.

[101] J. S. Jensen. Phononic band gaps and vibrations in one- and two-dimensional mass-spring structures. *J. Sound. Vib.*, 266:1053–1078, 2003.

[102] M. I. Hussein, G. M. Hulbert, and R. A. Scott. Band-gap engineering of elastic wave guides using periodic materials. *Pro of the 2003 ASME International Mechanical Engineering Congress and R&D Expo, Washington, DC, ASME Publication*, New York:799–807, 2003.

[103] M. I. Hussein, G. M. Hulbert, and R. A. Scott. Dispersive elastodynamics of 1D banded materials and structures: analysis. *J. Sound. Vib.*, 289:779–806, 2006.